Life and Death of Mixed Metal Halide Perovskites

Mechanism and Consequences of Light Induced Halide Segregation in MAPb(I,Br)3

Suchan, Klara

2023

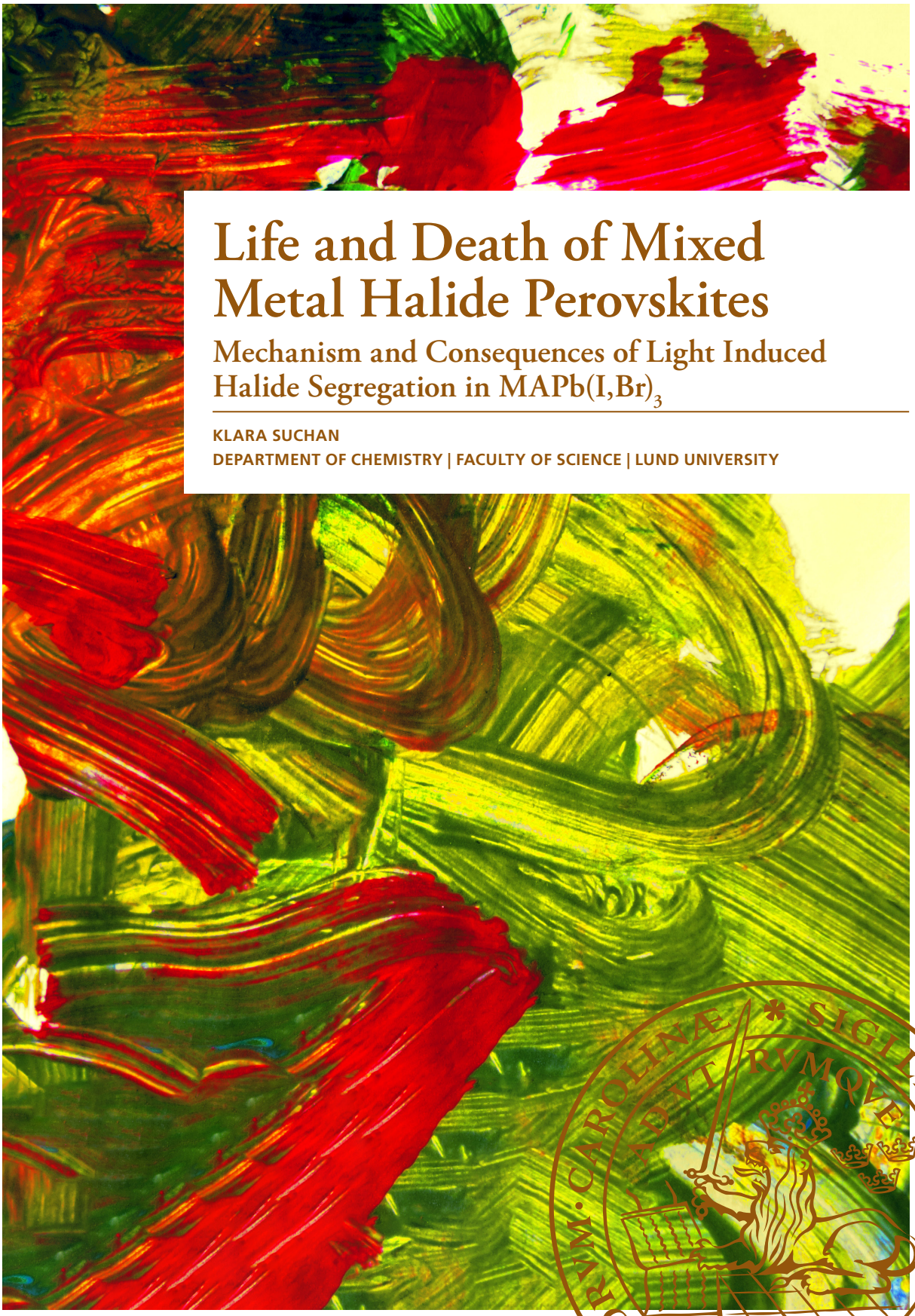

Life and Death of Mixed Metal Halide Perovskites

Mechanism and Consequences of Light Induced Halide Segregation in $MAPb(I,Br)_3$

KLARA SUCHAN
DEPARTMENT OF CHEMISTRY | FACULTY OF SCIENCE | LUND UNIVERSITY

Printed by Media-Tryck, Lund 2023 NORDIC SWAN ECOLABEL 3041 0903

Faculty of Science
Department of Chemistry
Division Chemical Physics

ISBN 978-91-7422-948-6

Life and Death of Mixed Metal Halide Perovskites

Life and Death of Mixed Metal Halide Perovskites

Mechanism and Consequences of Light Induced Halide Segregation in $MAPb(I,Br)_3$

by Klara Suchan

LUND
UNIVERSITY

Thesis for the degree of Doctor of Philosophy
Thesis advisors: Prof. Eva Unger, Prof. Ivan Scheblykin
Faculty opponent: Prof. Michael Toney

To be presented, with the permission of the Faculty of Science of Lund University, for public criticism in KC:A lecture hall at the Department of Chemistry - Division Chemical Physics on 12 of May 2023 at 9:00.

Organization **LUND UNIVERSITY** Department of Chemistry - Division Chemical Physics Box 124 SE–221 00 LUND Sweden	Document name **DOCTORAL DISSERTATION**
	Date of disputation 2023-05-12
	Sponsoring organization
Author: Klara Suchan	

Title and subtitle

Life and Death of Mixed Metal Halide Perovskites: Mechanism and Consequences of Light Induced Halide Segregation in $MAPb(I,Br)_3$

Abstract

Metal halide perovskites have attracted immense scientific interest due to their outstanding optoelectronic properties over a wide bandgap range. Applications cover a wide range of optoelectronic devices from solar cells, LEDs and lasers to X-ray detectors.[1, 2] Particularly in combination with existing silicon technology, perovskite-silicon tandem solar cells, which achieve power conversion efficiencies of over 32 %, have the potential to reduce the effective cost of solar cell devices, making them economically viable over carbon-based energy generation.[1] Despite tremendous efforts, the reliable and stable operation of metal halide perovskites is still hindered by dynamic phenomena such as current-voltage hysteresis,[3, 4] dynamic defect formation,[5, 6] degradation and light-induced phase segregation.[7] The high ion mobility of metal halide perovskites has been proposed to be at the core of these critical instabilities that prevent commercial application. Ion mobility is known to be enhanced under illumination. However, in single halide systems it is not trivial to detect ion migration. Mixed halide systems therefore provide a unique model system for monitoring ion migration due to the formation of distinctly different phases under illumination. This provides a unique opportunity to gain further insight into the relationship between optical excitation and ion migration.
This thesis investigates the phase segregation that occurs upon optical illumination of metal halide perovskites with mixed halides (bromide and iodide).

In a meta-data study, we analyze over 45 000 solar cell device metrics to explore the contribution of phase segregation to device performance.

Furthermore, we analyze the mechanism of phase segregation. In this work, we present insights from photoluminescence microscopy as well as multimodal photoluminescence and X-ray diffraction measurements of the temperature and composition dependence of phase segregation. We revealed the complexity of the phase segregation process and proposed an alternative kinetic model to rationalize the entire process.

In addition, we described the X-ray sensitivity of mixed metal halide perovskites and the challenges encountered when using X-ray-based characterization techniques. In particular, we discovered that X-ray induced defects can alter the photo-stability of metal halide perovskites, making meaningful characterization of the phase segregation process very complex.

Our results highlight the complex interplay between ion mobility, photostability, and photon-induced defects. We are confident that these insights will contribute to a detailed understanding of light-induced phase segregation and ion migration in general. We hope that this understanding will point the way to stable and reliable operation of metal halide perovskite solar cells.

Key words

Mixed Metal-Halide Perovskites, Light induced phenomena, X-ray Diffraction, Photoluminescence, Phase Segregation

Classification system and/or index terms (if any)

Supplementary bibliographical information		Language English
ISSN and key title		ISBN 978-91-7422-948-6 (print) 978-91-7422-949-3 (pdf)
Recipient's notes	Number of pages 212	Price
	Security classification	

Life and Death of Mixed Metal Halide Perovskites

Mechanism and Consequences of Light Induced Halide Segregation in $MAPb(I,Br)_3$

by Klara Suchan

LUND
UNIVERSITY

Cover illustration front: Painting by Leona Suchan.

Faculty of Science, Department of Chemistry - Division Chemical Physics

isbn: 978-91-7422-948-6 (print)
isbn: 978-91-7422-949-3 (pdf)

Printed in Sweden by Media-Tryck, Lund University, Lund 2023

Printed matter
3041 0903

Media-Tryck is a Nordic Swan Ecolabel
certified provider of printed material.
Read more about our environmental
work at www.mediatryck.lu.se

MADE IN SWEDEN

Dedicated to my daughters
Karlotta Suchan – Leona Suchan

Contents

List of publications

This thesis is based on the following publications, referred to by their Roman numerals:

I **Rationalizing Performance Losses of Wide-Bandgap Perovskite Solar Cells Evident in Data from the Perovskite Database**

K.Suchan, J.Jacobsson, C. Rehermann, M. Simmonds, E. Unger, T. Kirchartz, C. Wolff

Manusscript in preparation

II **Complex evolution of photoluminescence during phase segregation of $MAPb(I_{1-x}Br_x)_3$ mixed halide perovskites**

K.Suchan, A.Merdasa, C. Rehermann, E. L. Unger, I. G. Scheblykin

Journal of Luminescence, **2020**, 221, 117073

III **Multi-Stage Phase-Segregation of Mixed Halide Perovskites under Illumination: A Quantitative Comparison of Experimental Observations and Thermodynamic Models**

K.Suchan, J. Just, P. Becker, C. Rehermann, A. Merdasa, R. Mainz, I. G. Scheblykin, E. Unger

Advanced Functional Materials, **2023**, 33,2206047

IV **Light-Induced Halide Vacancies as Key Players in the Temperature-Dependent Phase Segregation of Mixed Metal Halide Perovskites**

K.Suchan, J. Just, P. Becker, C. Rehermann, A. Merdasa, R. Mainz, I. G. Scheblykin, E. Unger

Manusscript in preparation

Publications not included in this thesis:

Optical in situ monitoring during the synthesis of halide perovskite solar cells reveals formation kinetics and evolution of optoelectronic properties

K.Suchan,J. Just, P. Becker, E. L. Unger, T. Unold

Journal of Materials Chemistry A

Vertically Aligned $CsPbBr_3$ Nanowire Arrays with Template-Induced Crystal Phase Transition and Stability

Z.Zhang, **K.Suchan**, H. Li, C. Hetherington, A. Kiligaridis, E. Unger, I. G. Scheblykin, J. Wallentin

The Journal of Physical Chemistry C

Origin of Ionic Inhomogeneity in $MAPb(I_xBr_{1-x})_3$ Perovskite Thin Films Revealed by In-Situ Spectroscopy during Spin Coating and Annealing

C. Rehermann, A. Merdasa, **K.Suchan**, V. Schröder, F. Mathies, E. L. Unger

ACS Applied Materials & Interfaces

Roadmap and roadblocks for the band gap tunability of metal halide perovskites

E.Unger, L. Kegelmann, **K.Suchan**, D. Sörell, L. Korte, S. Albrecht

Journal of Materials Chemistry A

Acknowledgements

This thesis would not have been possible without the support and insights of many smart and great people. I am deeply grateful to all those who have contributed to my research in one way or another. Their expertise, encouragement, and support have been invaluable to me, and I could not have completed this journey without them.

In particular, I would like to thank Eva Unger. Your unique supervision approach and trust in my scientific capabilities have given me the freedom to develop and follow my own ideas. Your dedication and passion for research have been a constant source of inspiration and motivation. I would also like to express my sincere thanks to Ivan Scheblykin, formally my co-supervisor, but your mentorship went much beyond that. I felt honest support from you, through the good and the bad. It made all the difference to know, that you were there to fight and celebrate with me.

I would also like to thank the members of Eva Unger's group in Berlin. My sincere thanks go to Carolin and Oleksandra, who provided me with samples throughout my PhD. Hampus and Maxim for their conversations, feedback, and advice.

I am especially grateful to the group members of Ivan's Single-Molecular-Spectroscopy-group, who provided me with their friendship, support, and encouragement throughout my PhD. Aboma, you were he for me when I had just started my PhD. You taught me so much on PL-microscopy and Science in general. Marina, I really enjoyed the time we had as office-mates. Thank you for all the fun conversations and all the help with Matlab. Special thanks also to Chen and Shraddha, for their enormous empathy during the last phase of my PhD. They patiently listened to yet a new catastrophe every day. You are the best! I will surely miss you!

My research journey has been greatly enriched by the knowledge, experience, and support of the entire division of chemical physics. Because of all of you I enjoyed coming to work everyday. I remember so many special moments, laughter and joy. Friday Fika quickly became my favorite part of the work-week. Special thanks also to my 'post-doc-mentor-group' buddies, Christina, Eglė and Linnea for all their input, advise and discussions around our futures. I hope you each find your own perfect path for your future. I thank the in-FORM project team at MAX IV for the provision of samples and degradation data. Further, I would like to thank the entire DanMAX and Balder teams at MAX IV, the P06 team at Petra III, as well as the MetalJet source team at HZB for beamtime and their extremely valuable support.

Beyond the research world I want to thank my friends, especially the parents of our 'tjej-gang' for going with us through sickness and health. You made me feel at home in Lund and Sweden in general.

Last but not least, I would like to express my love and gratitude to my family, for their unwavering support, child-care and patience throughout my PhD journey. Without my parents who raised me to believe that I could achieve anything this would not have been possible.

Thanks to my kids, Lotta and Leona: you are the life in my work-life balance. Playing with you in the afternoons makes me realise every day that there is more to life than just science.

Justus, I agree with Hampus, who said that you are the best! Your patience, understanding, and love has been the foundation of my success. Your willingness to listen, to offer advice, and to share the challenges and triumphs of my research has been invaluable to me. May this thesis not be the end, but only the beginning of our collaboration as scientists.

Popular summary in English

Today, the need for clean energy sources to meet society's growing demand for electricity in a sustainable way is becoming increasingly apparent. Not only is global demand for energy increasing, but the drive for carbon neutrality requires electricity to replace other, more carbon-intensive forms of energy. Developing the capacity to generate and store electricity is therefore a key milestone in meeting the challenges ahead. This dissertation is my contribution to the quest to develop new technologies and improve existing ones for a greener future.

In 2012, metal halide perovskites were introduced as a new solar cell material. Since then, it has attracted a lot of attention due to its particularly high efficiency in converting solar energy into usable electricity. Combined with existing silicon technology, perovskite-silicon tandem solar cells, which achieve over 32 % power conversion efficiency, have the potential to reduce the effective cost of solar cell devices, making them economically viable over carbon-based energy generation. However, a major drawback to date has been their poor long-term stability. With current stabilities on the order of weeks to a few months, there is still a long way to go for successful commercialisation.

In this thesis I have studied a particular type of metal halide perovskite in which iodide and bromide ions are mixed. This is done to adjust the material properties for optimal combination in silicon-based tandem solar cells. However, when exposed to sunlight, the iodide and bromide ions segregate, resulting in the parallel formation of iodide-rich and bromide-rich domains. We analysed how this phenomenon affects the efficiency of solar cell devices by comparing 45 000 data sets of previously reported perovskite solar cell devices. In the main experimental part of this thesis, I discuss the mechanism of the segregation process in great detail. We were able to reveal another level of complexity than previously thought and proposed a refined model to describe the mechanism. Finally, we take a step back and consider how our X-ray measurements may affect the phenomenon under study.

Our results are a contribution to the collective effort to understand the diverse phenomena underlying the current instabilities in metal halide perovskites. Hopefully they will guide design strategies towards highly efficient and stable perovskites.

Populärvetenskaplig sammanfattning på svenska

I dag blir det allt tydligare att det finns ett behov av miljövänliga energikällor för att på ett hållbart sätt möta samhällets växande efterfrågan på elektricitet. Utöver att den globala efterfrågan på energi öker, kräver också strävan efter koldioxidneutralitet att elektricitet ersätter andra, mer koldioxidintensiva energiformer. Att utveckla kapaciteten att generera och lagra el är därför en viktig steg för att möta de kommande utmaningarna. Denna avhandling är mitt bidrag till ansträngningarna att utveckla ny teknik och förbättra befintlig teknik för en grönare framtid.

År 2012 introducerades metallhalogenidperovskiter som ett nytt solcellsmaterial. Sedan dess har det väckt stor uppmärksamhet på grund av sin särskilt höga effektivitet när det gäller att omvandla solenergi till användbar elektricitet. I samband med befintlig kiselteknik har tandemsolceller av perovskit och kisel, som uppnår en energiomvandlingseffektivitet på över 32 %, potential att minska den effektiva kostnaden för solenergi, vilket gör dem ekonomiskt lönsamma jämfört med kolbaserad energiproduktion. En stor nackdel har dock hittills varit deras dåliga långsiktiga stabilitet. Med nuvarande stabiliteter i storleksordningen veckor till några månader är det fortfarande en lång väg kvar till en framgångsrik kommersialisering.

I denna avhandling har jag studerat en särskild typ av metallhalogenidperovskit där jodid- och bromidjoner blandas. Detta görs för att anpassa materialets egenskaper till kisels egenskaper. När de utsätts för solljus separeras dock jodid- och bromidjonerna, vilket resulterar i att det parallellt bildas jodidrika och bromidrika domäner. Jag analyserade hur detta fenomen påverkar solcellernas effektivitet genom att jämföra 45 000 dataset av tidigare rapporterade perovskitsolceller. I den centrala experimentella delen av denna avhandling tog jag en närmare titt på mekanismen för segregationsprocessen. Vi kunde avslöja en annan nivå av komplexitet än vad man tidigare trott och föreslog en förfinad modell för att beskriva mekanismen. Slutligen tar vi ett steg bakåt och överväger hur våra röntgenmätningar egentligen påverkar det studerade fenomenet.

Våra resultat är ett bidrag till den kollektiva ansträngningen att förstå de olika fenomen som ligger till grund för de nuvarande instabiliteterna i metallhalogenidperovskiter. Förhoppningsvis kommer de att vägleda konstruktionsstrategier mot högeffektiva och stabila perovskiter.

Abbreviations and Symbols

CO_2	carbon dioxide
IEA	International Energy Agency
PV	Photovoltaics
NREL	National Renewable Energy Laboratory
3D	3-dimensional
MHP	Metal halide perovskite
PhD	Philosophical Doctor
XRD	X-ray diffraction
PL	Photoluminescence
LED	Light-emitting diode
SQ-limit	Schockley-Queisser-limit
c-Si	Crystalline silicon
MA	Methyl-ammonium
FA	Formamidinium
AM 1.5	Atmospheric Mass 1.5 Standard Spectrum
DFT	Density functional theory
CW	Continuous wave
CCD	Charge-coupled device
NA	Numeric aperture
XRF	X-ray fluorescence
XEOL	X-ray excited optical luminescence
XAS	X-ray absorption spectroscopy
SDD	Silicon drift diode
PLQY	Photoluminescence quantum yield
1D	1-dimensional
IRF	Instrumental response function
2D	2-dimensional
V_{oc}	Open circuit voltage
J_{sc}	Short circuit current density
PCBM	[6,6]-phenyl-C61-butyric acid methyl ester
PEDOT:PSS	poly(3,4-ethylenedioxythiophene) polystyrene sulfonate
SCAPS	Solar Cell Capacitance Simulator
FF	Fill factor
FWHM	Full width half maximum
HZB	Helmholtz-Zentrum Berlin
TRPL	Time resolved photoluminescence
XBIC	X-ray beam induced current
EDX	Energy dispersive X-ray analysis

Introduction

In today's world, it is becoming increasingly clear that there is a tremendous need for clean electricity sources to meet society's growing demand in a sustainable, less monopolized manner. Not only is global demand for energy growing, but the drive for carbon neutrality requires electricity to replace other, more carbon-intensive forms of energy. As a result of this electrification, demand for electricity is expected to triple by 2050. Access to energy is a key issue for improving health, education, and development. At the same time, the energy sector in its current form is the source of three-quarters of greenhouse gas emissions. In 2021, 13 gigatonnes of carbon dioxide (CO_2) were emitted by electricity generation alone.[8] As such, transforming the electricity industry plays a most central role in trying to avert the worst effects of climate change. In addition to greenhouse gas emissions, the power sector is largely responsible for current air pollution, acid precipitation, radioactive waste, hydrocarbon pollution, and trace metal pollution of soil and groundwater. Progress in clean power generation is therefore a necessity. The International Energy Agency (IEA) has published a roadmap for the global energy sector, outlining the key actions that need to be taken to achieve carbon neutrality by 2050. This is seen as the only chance to meet the 1.5-degree target of the legally binding Paris Agreement, which was adopted by 196 countries in 2015.[9]

However, the roadmap points out that tremendous work is still needed to achieve the goal of carbon neutrality by 2050. It states that "This will require nothing less than a complete transformation of the way we generate, transport and consume energy."[9] Moreover, it estimates that $\approx$40 % of the necessary CO_2 savings by 2050 need to come from technologies which are not yet developed. This emphasizes the great responsibility scientists have in meeting these expectations. Already today, solar energy is abundantly available and can be converted into electricity with the help of photovoltaics (PV). Even with current PV technologies, the world's electricity needs could be generated by PV modules with an efficiency of 25 %, covering only 0.3 % of the earth's surface.

Since the advent of PV, silicon solar cells have held the largest market share, which is expected to remain above 90 % by 2030.[11] In the last 10 years, the module efficiency of

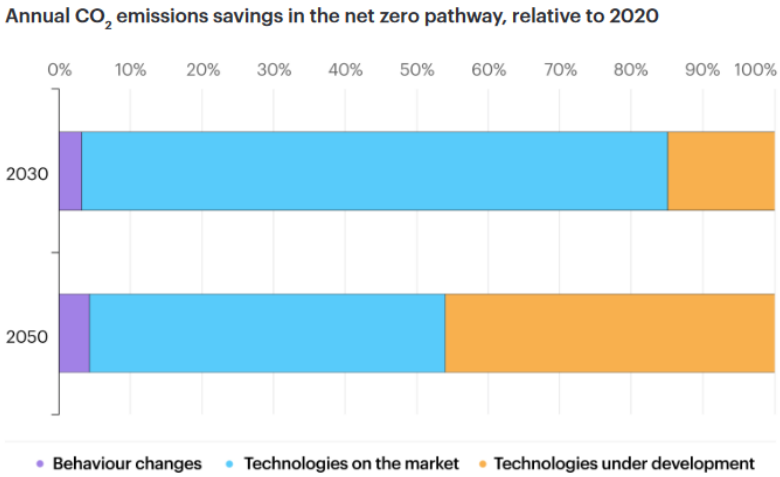

Figure 1: The annual CO_2 emissions savings in the net zero pathway, relative to 2020 highlight the importance of research in the quest to reduce the CO2 emission to net 0 by 2050, obtained with permission from IAE [9]

silicon modules has increased from 15 % to 20 %. Together with the decreased cost of modules due to significantly reduced material usage from 16 g/Wp to 2.5 g/Wp, this has led to significantly reduced energy payback times for silicon PV systems. In Northern Europe, silicon PV plants require about 0.9 to 1.1 years, depending on latitude, as shown in Figure 2 c.[11] From an energy perspective, installing silicon PV systems is thus already worthwhile even in Northern Europe. However, in the current capitalist system, only further improved cost efficiency will inevitably ensure the continued adoption of PV systems, independent of the political will. Meanwhile, newly installed PV power plants have overtaken newly installed coal-fired power plants, as they can produce electricity at lower cost. In addition, PV projects coming on line in 2022 have a projected average price of 0.04 $/kWh, about 27 % less than the cheapest fossil competitor, existing coal plants.[12] This is the first time that it has been economically favourable to decommission existing coal-fired power plants and replace them with PV plants. However, by the end of 2021, only 945 GW have been installed, resulting in PV power accounting for less than 4 % of the electricity generated worldwide.

While the price for silicon continuously decreases, the cost of PV is starting to flatten out because a large fraction of the cost of PV today are ternary costs associated with the installation and maintenance of the power plants, shown in Figure 2 a and b. This shows, that further reduction of the pure material price, will not contribute much to decreasing the price of solar energy generation. Ternary costs generally scale with the size and weight of the modules rather than the amount of energy generated. Therefore, increasing efficiency while maintaining the same module size and weight will effectively reduce the price per kWh. Thus, further improvement of existing silicon technology will inevitably make PV

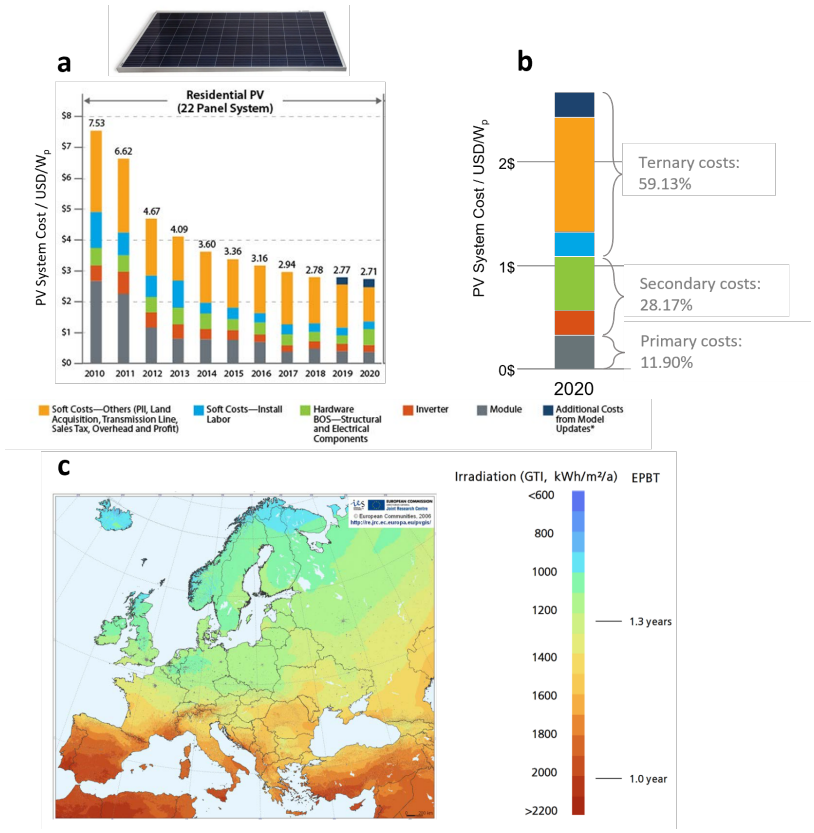

Figure 2: a) The levelized cost of photovoltaic electricity production has been decreasing in the past 10 years but is starting to level off at $\approx$ 2.7 \$/W_p in recent years. Reproduced with permission from NREL [10] b) The reason for this is that the ternary costs of photovoltaic, mainly installing and maintaining the module, makes up almost 60 % of the entire costs of electricity production today. The wafer itself is responsible for only about 12 % of the costs of solar energy conversion. Adapted from [10] c) shows the energy payback time in Europe dependent on the local irradiation. Even though the local irradiation in Sweden is only about half of that in Spain, the energy payback time is still as low as 1.3 years. Assuming a lifetime of 20 years, this means that a PV system installed in Sweden can produce 15 times the amount of energy that was needed for its production, reproduced with permission from Frauenhofer Institute ISE [11]

technology energetically and monetarily favourable over fossil alternatives, shorten the energy payback period, and thus reduce the CO_2/kWh caused by module production. While there are several approaches to increasing the efficiency of solar modules, tandem solar cells, which utilize a larger portion of the solar spectrum through the use of two absorber layers, have shown promise, as discussed in section 1.1.

Scope of This Work

In this work, I focus on bandgap tunable metal halide perovskites (MHPs) with mixed-halides. While MHPs show great promise in terms of their opto-electronic properties and solar cell device efficiency, their large drawback is their to date unstable operation. Mixing halides such as bromide and iodide tunes their bandgap and thus ensures compatibility with existing silicon technology. Silicon-perovskite tandem solar cells have recently achieved over 32 % efficiency. However, a reoccurring challenge is their insufficient stability. When exposed to light, the halides in mixed-halide MHPs tend to segregate, creating iodide- and bromide-rich domains.[13]

In a meta-data study (Paper I) we analyse solar cell device metrics reported in the *Perovskite Database* with respect to their bandgap, aiming to highlight pathways towards the development of efficient and stable operation of perovskite based PV across the entire bandgap range.[14] Through analysis of the reported device data available in the *Perovskite Database*, we evaluate the relevance of different of loss mechanisms, including the band-alignment in the device layer-stack, intrinsic defects and transient effects such as the light induced phase segregation. We conclude that the light induced phase segregation is responsible for a significant portion of the under-performance of MHP devices with a large bromide to iodide ratio, leading to a sharp decrease in output power after a few minutes.

In the main experimental work of this thesis, (Papers II, III and IV) we shine light on the mechanism of this light induced phase segregation. Understanding its mechanism is crucial towards mitigating segregation, making MHPs relevant for industrial implementation with the existing silicon PV technology. By comparing the evolution of structural and optoelectronic properties as well as microscopic and macroscopic insights, we are able to contribute to the current understanding of why and how the halides segregate under light.

In the attempt to perform spatially resolved X-ray based measurements (nano-X-ray fluorescence and 3D X-ray diffraction), the small spot sizes and thus high local X-ray fluxes revealed X-ray sensitivity to be a recurring, yet under-explored issue. Section 3.3 therefore contains preliminary results concerning the X-ray stability of mixed iodide-bromide perovskites. To consider X-ray stability is of foremost importance when employing X-ray based characterization techniques, especially in realtime *in-situ* measurements. Ensuring that the characterization is not interfering in the evolution of the properties of the probed system is the base for a meaningful analysis of the data. Beyond this, X-ray stability is a prerequisite for alternative usages of MHPs, for example as X-ray scintillator and for photovoltaic applications in space. With detailed X-ray diffraction measurements during degradation we are able to elucidate the degradation pathway and furthermore draw a first map of the dependence of X-ray sensitivity on the halide and cation system.

Outline

This thesis consists of two parts. Part one introduces the material system, key methods and methodology together with a summary of the major findings of the PhD work. The second part consists of a collection of papers and manuscripts (Paper I to IV).

Part 1:

Chapter 1: Serves as an introduction to the material properties and state of the art of Mixed Halide Perovskites (MHPs). A special focus is payed to material properties relevant to the tunability and the photo-stability of MHPs. An introduction to the phase-segregation phenomenon is given.

Chapter 2: The used experimental setups for X-ray diffraction (XRD) and photoluminescence (PL) are introduced. Beyond this the methodologies and analysis schemes used in this thesis and their challenges are discussed.

Chapter 3: The fourth and final chapter summarizes the main findings of this thesis related to the photo-induced phase segregation of metal halide perovskites. Beyond this, preliminary results on their X-ray sensitivity are included as the last section.

Part 2:

Paper I Here, we compare the perovskite solar cell device metrics, collected in the perovskite database, for wide bandgap solar cells. We evaluate the contribution of different loss mechanisms. We come to the conclusion that the light induced phase segregation plays a significant role in the under-performance of wide bandgap mixed-halide perovskite solar cells, employing high bromide fractions.

Paper II In this Paper we study the light induced phase segregation by photoluminescence microscopy. Studying the evolution of PL, we reveal a complex segregation pathway of mixed metal halide perovskites.

Paper III Here we employ multimodal XRD and PL to further analyze the multi-stage phase segregation process. We perform a quantitative analysis of the compositional phase distribution established upon illumination for $MAPb(I_{1-x}Br_x)_3$ samples with varying bromide fraction x. Based on these results, we quantitatively evaluate the proposed theoretical models and conclude that in addition to a pure thermodynamic model, a kinetic model is required to rationalize the entirety of the observed phase segregation.

Paper IV In the same experimental setup developed for Paper III, we study the phase segregation process for $MAPb(I_{0.4}Br_{0.6})_3$ samples at different temperatures between -20 °C and 60 °C. We compare our experimental results qualitatively with a simple 2D numerical model based on the results of Paper III.

Chapter 1

Mixed Metal Halide Perovskites

1.1 Bandgap Tunability

1.1.1 Importance of Bandgap Tunability for Opto-Electronic Applications

The bandgap is one of the most important physical properties that characterizes any semiconductor. Different technological applications require different bandgaps. Thus, the bandgap tunability of a material system is a desirable property because it allows the material to be optimized for any device application that requires a specific bandgap. The color of a light emitting diode (LED) is determined by the bandgap of the emitter. Bandgap tunability therefore makes it possible to produce an LED that emits a specific color of light. Modern telecommunications are based on silicon technology with a bandgap of 1.1 eV, so all materials used in telecommunications must be tuned to this energy. For example, waveguiding materials that need to be transparent at 1.1 eV require a lower bandgap energy.

In solar cells, the bandgap of the absorber material must be matched to the solar irradiance spectrum. The possible power conversion efficiency η of a solar cell device is therefore closely related to the bandgap of the material. The maximum achievable power conversion efficiency is given by the Schockley-Queisser limit, which is shown in Figure 1.1 d (solid black line) as a function of the absorber bandgap. The bandgaps of both GaAs and silicon, 1.4 eV and 1.1 eV respectively, are in the ideal range for a single junction solar cell, where the maximum achievable power conversion efficiency is about 33.7 %.[18] In Figure 1.1 a and d it is clear that even in this ideal range, and assuming ideal solar cells, still over 66 % of the solar energy is fundamentally lost. This is because photons with energy below the bandgap cannot be absorbed and are therefore transmitted. Photons above the bandgap are absorbed, but any energy above the bandgap is lost to thermalization. However, the

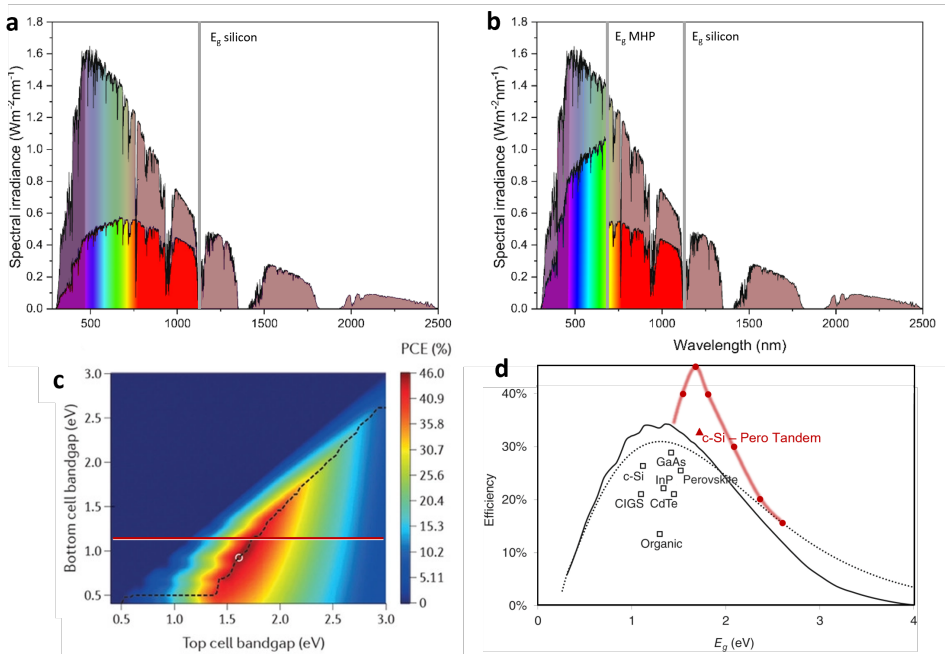

Figure 1.1: The solar energy spectrum can be used more efficiently when two absorber materials with matched bandgaps are stacked. a) shows the solar spectrum at AM 1.5 in dimmed rainbow colors. The practically usable part for a bandgap of 1.1 eV (silicon) is highlighted in stronger rainbow colors. b) shows the usable part of the solar energy spectrum for a tandem solar cell with a narrow bandgap absorber of 1.1 eV (silicon) and 1.75 eV (MHP). The inset shows a sketch of the principle of how the spectrum is split in a monolithic tandem device. c) Shows the theoretical efficiency limit of a monolithic tandem solar cell as a function of the bandgaps of the lower and upper cell materials. We have added the red line to indicate the bandgap of silicon as the bottom cell. Adapted from [15] ©2019 The Authors. Published by WILEY-VCH Verlag GmbH & Co. KGaA, Weinheim d) Shows the single-junction efficiency limit based on the AM1.5 standard solar spectrum (full line, black) and the limit for tandem solar cells based on silicon as the narrow-gap bottom cell (red). For comparison, the highest measured efficiencies for devices using different solar cell absorber materials and the record silicon tandem efficiency are shown. Adapted from [16], ©2022 The Author. WIREs Energy and Environment published by Wiley Periodicals LLC. With efficiency data from [17] and the theoretical limit of c-Si-Pero tandems digitized from [15]

achievable power conversion efficiency can be increased by using more than one absorber material in a solar cell device, as shown in Figure 1.1 b. In tandem solar cells, two absorbers are used. A large bandgap absorber is placed in front, ideally absorbing only the high energy photons. Photons with energy below the bandgap are transmitted and absorbed by the second absorber material with a smaller bandgap. This allows a larger fraction, up to 45 %, of the solar energy to be used.[19] For a tandem solar cell with silicon as the bottom cell, indicated by the red line in Figure 1.1 c, a bandgap closer to 1.7 eV is predicted to be most efficient. The predicted efficiency limit, compared to the Schockley-Queisser limit for a tandem with silicon, is shown in Figure 1.1 d in red. For integration into a tandem solar cell with GaAs (E_g = 1.4 eV), a bandgap as high as 1.9 to 2.0 eV is required, as shown in Figure 1.1 c.

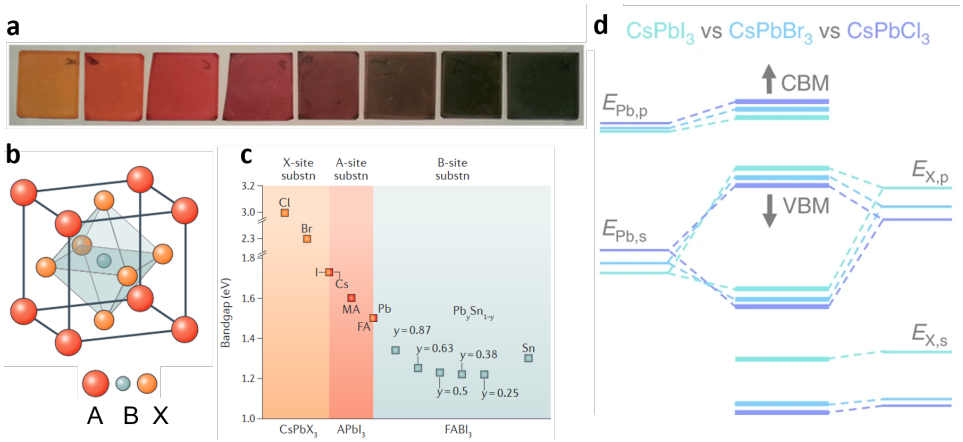

Figure 1.2: a) photograph of $FAPb(I_{1-x}Br_x)_3$ samples with varying x. b) shows the perovskite ABX_3 structure. The bandgap can be tuned by substitution of either the halide, X, shown in yellow, the cation A or the metal B. Figures reproduced from [20, 21] Reproduced with permission from Springer Nature. Substitution of the halide, has a large effect on the bandgap due differences in electronegativity of I, Br and Cl. These differences lead to a shift of their p-orbital, effecting the valence band of in the perovskite lattice. Reproduced from [22], ©2019, The Author(s). Nature Communications published by Springer.

1.1.2 What Changes the Bandgap of Metal Halide Perovskites?

Their bandgap tunability in conjunctions with good opto-electronic properties makes metal halide perovskites a promising material class to be used in a variety of opto-electronic applications. Perovskite-type crystals have the general chemical formula of ABX_3, in which the A ion is a relatively large cation at the center of the unit cell, the B ion is a smaller cation at the corners, and the three X anions at the centers of the edges of the unit cell (Figure 1.2). While some oxide and chalcogenide perovskites are being explored, the perovskites that are used in PSCs are mainly metal halide perovskites, where A = methylammonium (MA^+), formamidinium (FA^+), cesium (Cs^+) or rubidium (Rb^+); B = lead (Pb^{2+}) or tin (Sn^{2+}); X = iodide (I^-), bromide (Br^-) or chloride (Cl^-). While most research has been conducted on $MAPbI_3$ and $FAPbI_3$, which exhibit optical bandgaps of $\approx$ 1.55 and $\approx$ 1.48 eV, respectively, the bandgap of metal halide perovskites can be tuned between 1.2 eV and 3 eV, as shown in fig 1.2.

Generally, a substitution with a smaller ion can either contract the lattice, or tilt the BX_6 octahedra. In the case of the most common Pb perovskites, the substitution of A-site cations and X-site ions with a smaller ion (e.g. FA by MA or I by Br), leads to contraction of the lattice. This results in the peakshift in XRD to higher diffraction angles, presented in section 2.4.2 The formation of the bandgap follows a slightly more complicated rationale. The bandgap of Pb based metal halide perovskites is formed by the anti-bonding states between the s-orbital of Pb and the p-orbital of the X-site halide. The conduction band is mostly dominated by the p-orbital of Pb with only a minor influence of the s-orbitals of the

halides. The substitution of the X-site ions, leads to two competing effects on the bandgap. The increasing electronegativity of chlorine, compared to bromine and even more so for iodine, leads to stabilisation and thus decrease in the original energy of the X-site p-orbital, $E_{X,p}$ going to smaller ions. This decrease of $E_{X,p}$ leads to a strong decrease of the valence band energy. In the ABX_3 structure, the contraction of the lattice for smaller ions leads to a stronger overlap of the orbitals and thus stronger splitting. While this is the dominating effect in most alloyed semiconductors, it only results in a minor modulation of the valence band energy in the case of Pb based MHPs.[22] Partially exchanging the relatively large iodine with in MAPbI3 with a smaller bromine with stronger electronegativity thus leads to a significant increase in the bandgap to up to 2.2 eV.[23]The resulting bandgap follows approximately the linear Vegard's law.[24]

While the pure iodide perovskites have been extensively researched, with over 30000 reported devices, mixed bromide-iodide devices are relatively scarcely reported, as we discuss in Paper I.

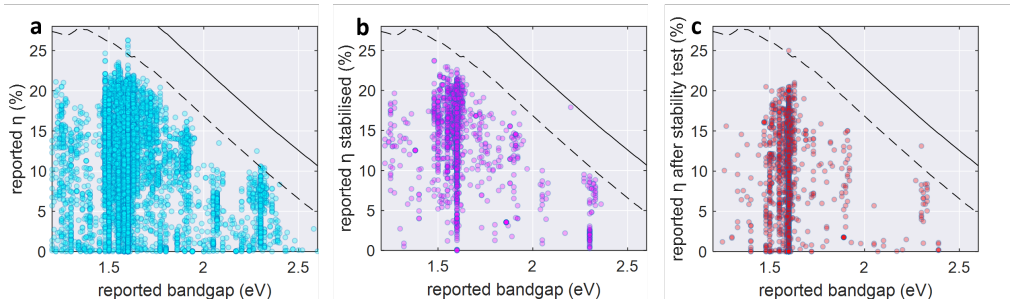

Figure 1.3: (a) The device efficiency as a function of perovskite bandgap for all cells in the Perovskite Database together with the SQ limit (solid) and the SQ limit minus 5 % (broken). While around 1.6 eV and 2.3 eV, the device efficiency is approaching the SQ limit, the efficiency is less optimal at bandgaps below 1.5 eV and shows a gap between 1.7 and 2.2 eV. The reoccurring stability issues become apparent when looking at the stabilised efficiency (b) and the efficiency after stability tests. The pronounced decrease in data-density, signifies a lack in reporting stabilised efficiency and stability tests. The gap between 1.7 and 2.2 eV becomes especially pronounced when considering the efficiency after stability tests, which is likely due to photo-instability of mixed halide perovskites.

1.1.3 State of the Art of Bandgap Tunability

Next to the mere ability to synthesize materials with various bandgaps, two things are of key importance:

- Maintaining high material quality → good device efficiency
- chemical stability → stable device efficiency

Jacobsson et al. recently developed an online platform that allows browsing, uploading and downloading experimental solar cell data. The perovskite device database including over 45 000 devices with their metadata, was created by 80 contributors, collecting information from initially over 17 000 papers.[14]. The power conversion efficiency η is plotted with respect to the device bandgap in Figure 1.3 a. When looking at the 45 000 devices reported in the perovskite database, it becomes obvious, that while the device efficiency is coming close to the Schockley-Queisser limit for perovskite absorbers with a bandgap around 1.6 eV, this extraordinary performance is not maintained across the entire bandgap range. Deviations from the theoretical limit can be seen in the narrow-bandgap regime around 1.4 eV, which is the ideal range for single junction solar sells. Furthermore, in the region between 1.7 eV and 2.0 eV, which is relevant for tandem and multi-junction solar cells, a clear dip in device performance can be seen. The sub-optimal performance of the devices in this band gap range may have several reasons which are discussed in detail in Paper I. A prominent reason is the reported photo-instability of mixed bromide-iodide perovskites, which is the research topic in papers II, III and IV.

When looking at the performance after stability tests have been conducted, it becomes

evident, that to date no stable perovskite solar cells with a bandgap around 1.9 eV have been reported, (see Figure 1.3b). This clearly indicates inferior stability in this range. This bandgap region coincides with the instability region due to the photo-induced phase segregation. It becomes thus clear, that while mixed bromide-iodide films and even devices can be prepared over the entire bandgap range, high power conversion efficiencies are not maintained over the entire bandgap range. Moreover, despite the massive amount of reported device date (>45 000 devices) no long-term stable and efficient devices have been reported in the bandgap region between 1.8 and 2.2 eV.

1.2 Elastomechanical properties of perovskites

Despite tremendous efforts, the reliable and efficient operation of metal halide perovskites today is still hindered by dynamic phenomena such as current-voltage hysteresis,[3, 4] dynamic defect formation[5, 6] degradation and light induced phase segregation[7]. Ion migration has been proposed to lie at the heart of these critical instabilities preventing commercial application. On the other hand, more recent literature stresses the self-healing potential which comes alongside high ion mobility. As a result of both the challenges and potentials connected to ion mobility, lately greater attention is being paid to the remarkable 'softness' of metal halide perovskites.

1.2.1 A-priori Elastomechanical Properties

A remarkable property of metal halide perovskites is their often reported softness. The elastomechanical properties of metal halide perovskites resemble those of soft metals and polymers rather than more traditional semi-conductor materials. Macroscopically, the stiffness of metal halide perovskites is 10 times lower than that of conventional semiconductors such as GaAs and Si.[25] Studies on single crystals suggest that the Pb–X framework dominates the elastic modulus. The softness is caused by the high deformability and weakness of heterovalent Pb-X bonds. The lower elastic modulus of $MAPbI_3$ compared to $MAPbBr_3$ has been rationalized with weaker Pb–I bond strengths, compared to Pb-Br bond strength.[26] The soft lattice leads to high dynamic disorder in the lattice, which is so high, that a 'liquid-crystal dualism' has been proposed.[25, 27] Microscopically, this 'lattice-softness' yields high halide vacancy densities. At room temperature, equilibrium vacancy densities have been reported to be has high as 0.01 to 0.4 %.[4,10–13] Ion diffusion is proportional the vacancy density c_v by:

$$\boldsymbol{\mathcal{D}}(T) \;=\; f \cdot 1/6 \cdot c_v(T) \cdot \alpha^2 \cdot k(T) \tag{1.1}$$

where f is a correlation factor depending on the lattice symmetry, α is the jump lengths of a single jump and $k(T)$ is the jump frequency. Hence, these halide vacancies have been shown to be responsible for the major part of the observed ion migration.[28]

1.2.2 Light and Electrical Bias Induced Defect Formation

Under real operating conditions, the percentage of mobile ion vacancies is expected to be even higher due to additional light and electrical-bias induced halide vacancies.[29–31] Specifically, illumination above the bandgap with 100 mW· cm^{-2} has been shown to increase the ion conductivity by two orders of magnitude.[31] Reports of an ionic portion of the total conductivity of up to 60 % lead to metal halide perovskites to be described as mixed ionic electronic conductors.[28, 31] While in the dark, migration via pre-existing Schottky defects has been the most discussed pathway in metal halide perovskites, under light other mechanisms may start to play a role. The formation of light induced Frenkel defects where a vacancy-interstitial pair is formed, has been discussed.[32–34]

While light induced halide-vacancy formation has been proposed repeatedly, the exact mechanism is still under debate. Phung et al. recently discussed three possible pathways of photo-induced halide vacancy formation which all depend on the excess absorbed energy above the band-gap.[32]

1) the thermal pathway considers that the excess energy from photons with energies above the band-gap dissipates into the lattice during thermalization. The resulting heat-up of the lattice is weakening the Pb-halide bonds causing a dissociation reaction. 2) the photodissociative pathway occurs at photon energies high enough to directly break chemical bonds and thus directly induces the dissociation reaction without any intermediate step. This mechanism has frequently been proposed for the observed decomposition of PbI_2 into Pb^0 and volatile I_2. As the Pb-I octahedra in PbI_2 resemble those in $MAPbI_3$ a similar reaction may occur also in $MAPbI_3$. 3) As a third pathway, a synergy of pathways 1) and 2) is discussed, in which photons bring the system into a still bound but excited state which already weakens the Pb-halide bonds, such that they can be broken with less thermal energy.

By analysing the excitation energy dependence of the observed PL-shift related to the formation of halide defects, Merdasa et al. concluded that at low photon energies, below 2.3 eV, the thermal pathway dominates. At photon energies beyond 2.3 eV, the synergetic and finally the direct photodissociative pathways dominates, as the excess photon energy starts to be sufficiently high to directly dissociate the Pb-halide bonds. In inhomogeneous mixed Br-I perovskites, it further needs to be taken into account, that the excess photon energy, which is the energy above the band-gap is higher in iodide-rich domains compared to bromide-rich domains. Which can lead to an inhomogeneous defect density.

Beyond vacancy formation via the excess photon energy, even a direct charge carrier induced or assisted pathway has been discussed.[33] However, to date the mechanism behind this is far from agreed upon. If charge carriers are to play a direct role in the creation of halide vacancies this would have severe implication for inhomogeneously mixed Br-I perovskites, where nearly all charge carriers concentrate in small I-rich domains. The resulting vacancy density upon excitation will hence be strongly inhomogeneous.

1.3 Light Induced Halide Segregation

Ion migration lies at the heart of most of the critical instabilities which still prevent the commercial application of metal halide perovskites in application such as tandem solar cells or LEDs. Despite tremendous efforts, the reliable and efficient operation of metal halide perovskites today is still hindered by dynamic phenomena like hysteresis, dynamic defect formation, degradation and light induced phase segregation, largely induced by remarkably mobile ions in metal halide perovskites.[3, 29, 35–38] Ion mobility as the underlying cause is often illusive. When mixed metal halide perovskite samples are exposed to light, the halides in the sample segregate and distinct iodide rich and bromide rich phases appear. Ion mobility, as the prerequisite for the halide segregation, determines the phase-segregation process. Hence, light induced phase segregation of mixed metal halide perovskites provides a unique opportunity to watch the ions move due to the establishment of distinctly different phases under illumination. It is thus a unique chance to get further insights into the relation between optical excitation and ion migration.

The most apparent signifier of photo-segregation is the red-shift of the PL energy as a result from the charge carrier funneling into newly established iodide-rich narrow-bandgap domains. It is thus apparent that charge carriers loose a portion of their energy due to photo-segregation, which is obviously detrimental for high power conversion efficiencies. Recently several studies analysed the effect of the photo-segregation into iodide rich and bromide rich domains on solar cell efficiencies.[39–43] The experimental evidence clearly shows that phase-segregation is detrimental for the solar cell performance. Furthermore, it highlights, that while the V_{oc} is less affected than previously assumed, the J_{sc} is largely affected due to the isolated nature of the iodide rich domains, acting as efficient traps which we discuss in detail in Paper I. Consequently, understanding halide movement in perovskite absorbing layers is key to making perovskite solar cells viable for commercialization.

1.3.1 Experimental Observations

In the quest for long-term durable perovskites with a bandgap attuned to that of silicon, numerous studies have been conducted to grasps the details of the photo-induced phase segregation. As the phase segregation has been reported to be dependent on the atmosphere, the temperature, the synthesis conditions as well as the excitation intensity and energy, many seemingly contradicting observations have been reported. It is therefore important to differentiate between generally valid observations which have been consistently reported for a wide range of independent samples and individual reports which may be sample specific and not generally hold true.

Fundamental Observations, Agreed Upon in the Community There are a few fundamental aspects of the phase segregation process, which have repeatedly been proven to be valid rather generally by several different labs and studies. The red shift of the initial PL to a PL energy resembling that of samples with a bromide fraction of x = 0.2 as been observed by numerous research-groups.[7, 13, 29, 44–50] Especially striking is the consistency of the final PL energy across all bromide contents above x = 0.2. This has not only been reported for the MA material system, but even for other cation systems, the establishment of a low energy PL signal resembling the PL of an iodide rich sample (close to x = 0.2) has been observed (x ≈0.26 (MA^+), ≈0.21 (FA^+), ≈0.02 (Cs^+), ≈0.35 (FA^+/Cs^+), and ≈ 0.20 ($MA^+/FA^+/Cs^+$)) as shown in Figure 1.4 [44, 51–56]

This apparent universality of the approximate PL position, has sparked discussion of a thermodynamically stable 'terminal x-value'.[13, 56–60] A major focus of several theoretical models has been the explanation of such a 'terminal x-value', which has been rationalized by either critical x-values in the thermodynamic free energy of mixing[57, 61] or a cubic to tetragonal phase transition[62]. However, the cubic to tetragonal phase transition is not universal for different cation systems and has therefore been ruled out to be the only cause of the emergence of similar PL bands. Moreover, as we discuss in Paper III, the 'terminal x-values' have predominantly been observed by PL alone, which is by itself not the method of choice to gain reliable compositional information.

Studying the vast amount of PL spectra reported after phase-segregation, it becomes also apparent, that the low energy PL peak is continuously growing during phase segregation and that the PL spectra are immediately dominated by this growing low-energy PL peak. Eventually an equilibrium state is reached at which the PL does not change anymore. In this final equilibrium state, the original high-energy PL peak is often not detectable or reported to be at least 4 orders of magnitude lower in intensity. Charge carrier funnelling from the larger bandgap domains to iodide-rich narrow-bandgap domains has been proposed to be the cause.

The phase segregation process has been shown to be fluence dependent[7] and a threshold fluence necessary to induce phase segregation has been shown. Further the phase segregation process has been shown to be reversible if it is kept under dark conditions.[13] However, the reverse process is orders of magnitudes slower, such that often not the full reverse process is reported.

Structural measurements such as X-ray diffraction and absorption spectroscopy have confirmed the appearance of iodide rich and bromide rich phases. However, the reports on the structural changes during phase segregation are very diverse.[13, 42, 45–48, 51, 53, 64–66]

Conflicting Observations While it has been established that I-rich and Br-rich phases form when mixed halide perovskites are exposed to optical light, not much more details of

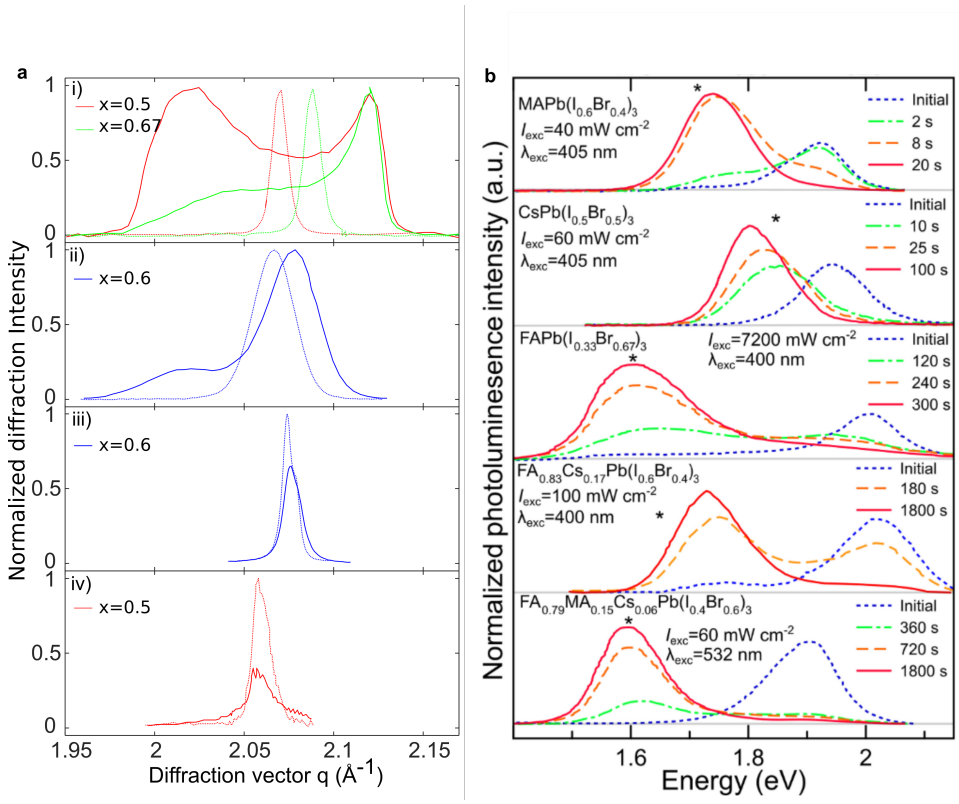

Figure 1.4: a) Time-evolved XRD patterns for MAPb(I$_{1-x}$Br$_x$)$_3$ reported by i)[63] ii)[13], iii)[47] and iv)[52], show the diversity of structural changes observed during segregation. The segregated patterns are shown in full lines and the initial pattern prior to illumination broken lines of the same color. All data was digitized using WebPlotDigitizer. b) Photoluminescence (PL) spectra for MAPb(I$_{1-x}$Br$_x$)$_3$[46], CsPb(I$_{1-x}$Br$_x$)$_3$[52], FAPb(I$_{1-x}$Br$_x$)$_3$ [54] , FA$_{0.83}$Cs$_{0.17}$Pb(I$_{1-x}$Br$_x$)$_3$ [44], and FA$_{0.79}$MA$_{0.15}$Cs$_{0.06}$Pb(I$_{1-x}$Br$_x$)$_3$[55] thinfilms. Asterisks represent PL emission energies associated with $x \approx 0.2$ for each cation composition. Figure reproduced from [56]

how the final stage actually looks like has been agreed upon. Some XRD measurements show a clear split into two distinct peaks, which seemingly agrees with the notion of the establishment of a thermodynamically favoured I-rich and a Br-rich peak.[13, 64, 66] Others have reported merely peak broadening with the majority phase keeping its compositions, while even other reports show a shift of the entire peak[47, 67]. The qualitative disagreement, shown in 1.4 makes a quantitative description of the final phase distribution very difficult. Especially the volume fraction of the iodide rich phase is subject to controversy. Values between 1 % and 24 % have been reported. While in an XRD pattern with two clear peaks, it might be possible to define an 'iodide-rich' and a 'bromine rich' phase,in other cases it is not straight forward. Generally different measurement techniques, probing slightly different material properties have given contradicting results. Already in the first report on phase segregation, a discrepancy was noted between XRD measurements

and absorption measurements.[13] Further, cathodoluminescence measurements observed iodide rich domains on the order of 8-10 nm, which would be too small to be even visible in XRD measurements. Alongside this the cathodoluminescence measurements suggested that the mixed phase keeps it's original composition, in clear contradiction to the XRD measurements.[61]

1.3.2 Theoretical Models Explaining Phase Segregation

It is generally agreed upon, that the phase segregation is a charge carrier induced effect as it can be light-[13, 45, 46, 48, 49, 68] bias-[53, 66] or electron-beam induced[69, 70]. Beyond this the process is fully reversible in the absence of charge carriers ruling out that charge-carriers merely deliver the energy needed to overcome an activation energy barrier. To date roughly three types of models have been developed, which each succeed to rationalize certain but not all aspects of the phase segregation process.

Polaron Model A widely discussed type of model is the polaron-model, in which it is postulated that the lattice-strain induced by the polaron is relaxed by the rearrangement of ions. Specifically the polarons get trapped in the narrow-bandgap iodide rich domains, where they attract further iodide, templating the growth of iodide rich domains.[57, 59, 61, 71, 72] Theoretical calculations based on the polaron model predict two minima in the potential energy for the compositions x = 0.2 and x = 0.8, which has been used to rationalize the universal PL energy position and the observations of two peaks in the XRD patterns.[61] However, this type of models falls short in rationalizing the excitation density threshold of the photo-segregation, which is accounted for in models relying on the difference between the band-gap of the original mixed phase and the light induced i-rich domains.[68, 73]

Band-gap Models In the so called band-gap models, the energy of the charge carriers can be reduced if the sample segregates, as the charge carriers can relax into the i-rich domains which exhibit a lower bandgap.[50, 60, 68, 74] While no clear minima in the potential energy exist, an interplay of entropy gain by mixing and band-gap reduction in certain areas by segregation leads to stable phases around x = 0.2.[74] Further the competition of entropy driven mixing and light induced segregation can explain the excitation threshold.

Drift-Diffusion Models A third type of models often called drift-diffusion models, relies on the combination of different diffusion rates of iodide and bromide and a field due to spatially diverging electron and hole distributions. Different reports suggest inhomogeneous excitation throughout the thickness of the perovskite film, or spatial difference in hole-and electron trapping to be the cause of an electric field. However, while the models most often

assume iodide to diffuse faster, DFT calculations predict bromide to diffuse significantly faster than iodide in mixed samples.[47, 52] Recently in our work, the role of the defect chemistry has been highlighted to play a major role. Especially the role of halide vacancies determining ionic transport has been discussed.[29, 49, 75, 76]

Chapter 2

Methods and Setups

This work is mainly based on the findings of photoluminescence and X-ray diffraction, both macroscopic and microscopic. In the following sections I will discuss the different methods used, with particular emphasis on the different sensitivities of each method to certain material properties. All three methods can be classified as standard characterisation techniques for semiconductor thin films, often used simply to confirm successful perovskite formation. However, their potential, if carefully investigated, goes far beyond this.

2.1 Photoluminescence Microscopy

An inverted wide-field fluorescence microscope based on an Olympus IX-71 frame, described in detail elsewhere [77], was used for the continuous wave (CW) photoluminescence (PL) measurements presented in Paper II. A sketch of the setup is shown in Figure 2.1. The samples were excited using a 458 nm CW Argon laser. The excitation power could be varied over several orders of magnitude using a set of neutral density filters in the excitation path. At normal operating conditions the power density at the sample plane was adjusted to 0.1 $W \cdot cm^{-2}$, corresponding to the power density of the sun at AM 1.5. An EM CCD camera (Princeton, ProEM 512 B) was used as detector to record the images. The acquisition time of each image was set to 100 ms, if not otherwise stated.

A defocusing lens was used, which shifts the focal point away from the objective, such that the beam-spot at the sample-plane is enlarged. In the study presented in Paper II, the beam-spot was roughly 30 µm in diameter. In this defocused configuration a large number of crystal grains can be imaged simultaneously. To measure the PL images, an oil immersion objective (60x Olympus UPlanFLN, NA 1.25) was used to obtained a high magnification, better resolution and better light collection. For this thin microscope cover

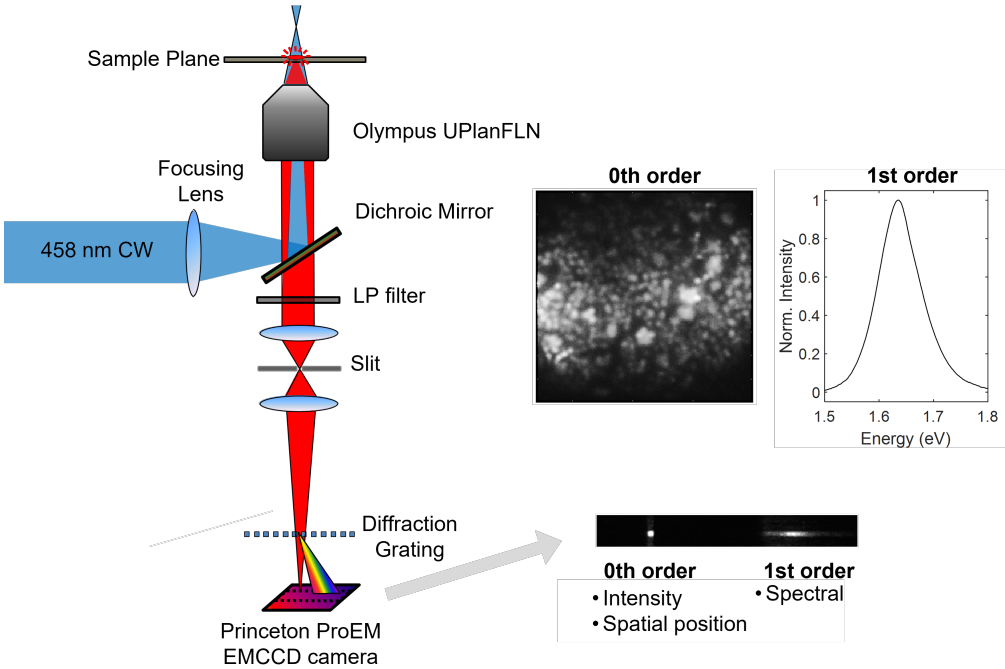

Figure 2.1: Shows the PL microscopy setup used for Paper II, together with a typical image of a perovskite sample as obtained using the 0th order without grating and a typical PL spectrum as obtained from the 1st order. Adapted from [77] and Paper II [7]

slips were used as substrates, with a thickness of 0.75 mm. The samples were placed with the substrates facing the objective and an immersion oil was inserted in between substrate and objective. The oil thus effectively eliminated the refractive index mismatch leading to better resolution of the obtained image. PL spectra were measured in this setup by inserting a narrow slit and a transmission grating in the detection path of the microscope. This causes the emitted light to diffract before reaching the detector plane. When light is diffracted from a grating, it forms a interference pattern with spatially separated fringes. The first order of the diffraction grating is used to measure the PL spectra. The grating is aligned with the slit, such that the pattern is formed horizontally. Thus on vertical detector-axis, the spatial information is contained, while on the horizontal axis, the difference between the 0th order and the 1st order represents the photon-energy. This is called a spectral image as it contains both, some spatial information as well as spectral information. The spectral resolution is determined by the width of the slit, the specifications of the grating as well as the distance between grating and detector as well as the effective pixel size of the detector. The spectral resolution has been calculated to be roughly 2.1 nm.[78]

Time-resolved PL was measured with the same PL microscope described above, using a 405 nm pulsed laser (PicoQuant) for excitation at 2 MHz repetition rate and an average

power of 0.1 W cm^{-2} (1 sun). This results in a photon flux of $2.04 \cdot 10^{17}$ photons$\cdot$ $cm^{-2} \cdot s^{-1}$ and thus $1.02 \cdot 10^{11}$ photons $\cdot cm^{-2}$ per pulse. Photons were detected by an avalanche photodiode (Mico Photonic devices) coupled to a PicoHarp300 counting system (PicoQuant). To record time-resolved kinetics for a continuously changing sample, we used the time-tagged mode, where the absolute arrival time of each detected photon was recorded with ps accuracy (so-called T3 mode). The data set allowed the calculation of PL decay kinetics with 200 ps time resolution over a chosen time interval. The 1 s time interval was chosen as a compromise between data quality and a reasonable time resolution to resolve the appearance of the transient PL peak.

2.2 Multimodal XRD and PL at Limax 60, Bessy II

In order to measure multimodal PL and XRD simultaniously at the same area of interest we designed a small scale portable PL setup, which can easily be integrated into the X-ray path at different X-ray sources, maintaining the same measurement geometry and working distances when employed at different X-ray sources. This setup is used for the multimodal CW-PL and XRD measurements in Paper III and IV presented in this thesis. A sketch of the setup is shown in Figure 2.2

2.2.1 Photoluminescence

To measure PL, the samples were excited using an LED with emission centered at 453 nm. Using an LED as excitation source allows to illuminate the entire sample area. The wavelength of 453 nm was chosen as it is below the bandgaps of both $MAPbI_3$ and $MAPbBr_3$. The absorptivity of $MAPbI_3$ and $MAPbBr_3$ is near unity for both materials as it is significantly below the bandgap. The excitation power is varied by tuning the input power for the LED. For the measurements presented in Paper III and IV, the power was set to 0.1 W$\cdot cm^{-2}$ using a power-meter. 0.1 W$\cdot cm^{-2}$ corresponds to the solar power density at AM1.5. However, it has to be noted, that the spectrum of the LED differs significantly from an actual solar spectrum and thus needs to be considered as a model system. We nonetheless chose the nearly monochromatic light of an LED, as it is equally absorbed by both $MAPbI_3$ and $MAPbBr_3$ and all solid solutions. A broad white light spectrum is absorbed differently by $MAPbI_3$ and $MAPbBr_3$ due to their different bandgaps. Different numbers of photons would be absorbed at constant flux, making the analysis more difficult, especially if chemically in-homogeneous samples are considered. The integration time for the PL spectra was set according to the sample luminescence yield.

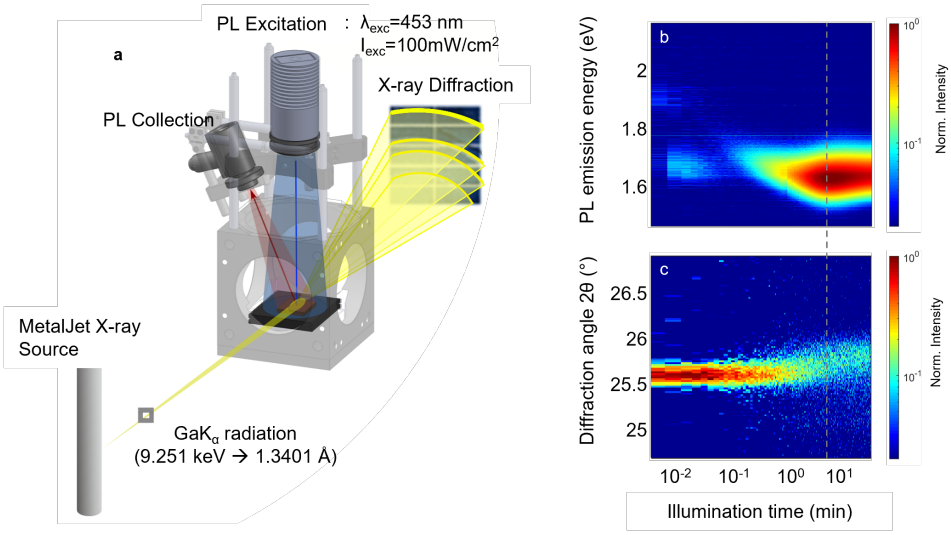

Figure 2.2: (a) shows the multimodal PL and XRD setup as placed at the MetalJet X-ray source LIMAX-70 (b) shows the typical results obtained by simultanious real-time PL and XRD measurement. Reproduced from Paper III [29]

2.2.2 X-ray Diffraction

Simultaneous *in-situ* X-ray diffraction measurements were performed at the LIMAX laboratory 1 at BESSY II (Berlin), equipped with a liquid-metal-jet X-ray source emitting high-flux GaKα radiation. A PILATUS3 R 1M area detector was used to detect the diffraction signal.[79, 80] Due to the splitting of the GaKα line into GaKα_1 and GaKα_2, the measured XRD patterns of the homogeneous samples show a double peak for each reflex. A range of 2 θ from 10°to 32°was measured at constant incidence angle of 2 $\theta \approx 25°$focusing on the pseudo-cubic /cubic 200 reflex. Due to the measurement geometry, the reflex in focus has a minimized instrumental broadening, allowing for a good resolution of the sample induced broadening, whereas any reflex at a different angle exhibits a larger instrumental broadening. The 2D diffraction image was subsequently integrated azimutally over an arc between $\eta = \pm 5°$resulting in an 1D diffraction pattern of intensity over diffraction vector length. Using a certified LaB_6 reference sample the setup was calibrated an the instrumental broadening deduced.

Atmosphere Control The PL setup is placed on top of an atmosphere and temperature controlled sample environment. To control the temperature a Peltier-element was placed beneath the sample-stage. In Paper III, this was used to keep the temperature constant at 20 °C, whereas in Paper IV the temperature was deliberately set between -20 °C and

60 °C. The temperature at the sample plane was constantly monitored using a temperature probe placed in the sample-stage. For the entire measurement the sample was placed in N_2 atmosphere with slight over pressure.

2.3 Multimodal XRD, XRF and XEOL at Balder, MAX IV

The investigation of the X-ray degradation of mixed halide perovskites has been performed at the recently developed multimodal setup at Balder beamline at MAXIV (Lund). Its unique feature is that it allows simultaneous measurements of X-ray fluorescence (XRF), X-ray excited optical luminescence (XEOL), X-ray diffraction and X-ray absorption spectroscopy (XAS). However, here we focused on XRD, XRF and XEOL measurements. A highly monochromatic X-ray beam with an energy of 12.8 keV and a spot size of 100·100 μm^2 was used. The XRD measurements were performed in the grazing incidence geometry, at an angle of 3°. The XRD patterns were detected by an Eiger 1M area detector, azimuthally integrated and calibrated using an LaB_6 reference sample. XRF was acquired using an Amptek FAST SDD detector and calibrated using PyMCA. The resulting optical luminescence (XEOL) was detected using a fibre coupled ocean optics optical spectrometer. All measurements were performed in an N_2 atmosphere.

XRF provides a quantitative measure of the elements present in a material. X-ray photons have sufficient energy to excite a core level electron, leaving a core hole. Electrons recombining with the hole from higher orbitals emit an X-ray photon with an energy characteristic of

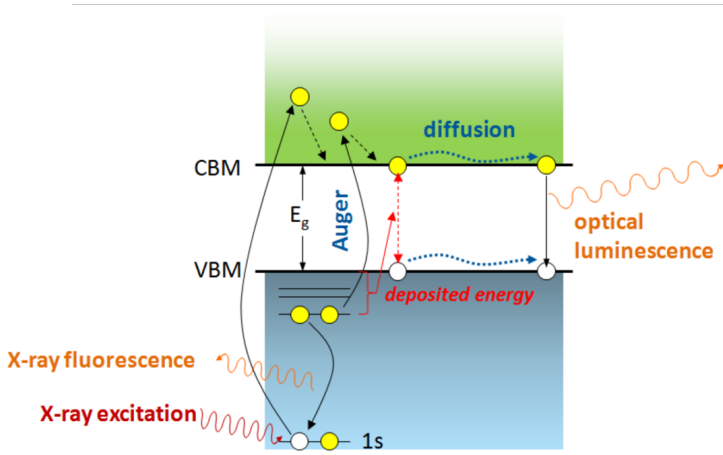

Figure 2.3: Schematic illustration of the fundamental principles of XRF and XEOL. Following X-ray excitation, the recombination of electrons with the core-hole yields X-ray fluorescence. The excited electron commonly possesses enough energy to excite thousands of charge carriers in a cascade effect. They thermalize to the conduction band minimum where they relax by emitting an optical photon, detected as XEOL spectrum.

the energy difference between the orbitals, as shown in the Figure 2.3. Since this energy difference is characteristic of the specific element, the energy and intensity of the fluorescence gives information about the amount of an element. XRF therefore gives information about the composition of the film without differentiating the compound in which the element is found. In contrast, the intensity an position of a peak in XRD can give an indication of the amount and the composition of this crystal phase, as discussed in section 2.4.2 If PbI_2 is formed as a degradation product, this is thus immediately visible by XRD, as Pb and I, but not necessary by XRF as the amount of Pb and I remain unchanged in the film.

XEOL is the optical light emitted after excitation with X-rays and was first measured in 1974.[81] We use XEOL to follow the evolution of optoelectronic properties during X-ray degradation without additional exposure to intense optical light in section 3.3. In XEOL, core-level electrons are excited by incident X-rays, while subsequent cascaded relaxation processes result in the creation of charge carriers in the valence and conduction band. The number of carriers produced is therefore roughly proportional to the X-ray energy. For an X-ray energy of 12 keV and a band gap of $\approx$ 2 eV, 500-1000 charge carriers per photon are generated. The carriers generated in this way thermalize to the conduction band energy, just like the carriers generated by optical light.

The resulting emission, assuming constant monochromatic excitation, is therefore identical to the emission of optically excited carriers. The resulting spectra can therefore be analysed in the same way as PL spectra.

2.4 Correlating Compositional Information From PL and XRD

2.4.1 Compositional Information From PL

To obtain compositional information from PL, the individual spectra need to be analysed in detail. If an electron-hole pair is generated by a photon, the charge carriers thermalize to their respective equilibrium state (VBM and CBM) before they recombine. This is the lowest energy state within the charge carrier diffusion length. Depending on the allowed states in the semiconductor, there are multiple possible recombination channels as shown in Figure 2.4

To interpret the measured photoluminescence signal correctly, the recombination channel responsible for the detected emission has to be identified. Excitonic recombination is primarily present at low temperatures, below the binding energy of the exciton. In $MAPbI_3$, the exciton binding energy has been measured to be only 18-25 meV.[83, 84] At 20 $^{\circ}C$, corresponding to 25 meV, the excitonic contribution is considered to be negligible. This agrees with the observed PL peak shape, which does not show any sharp emission lines expected

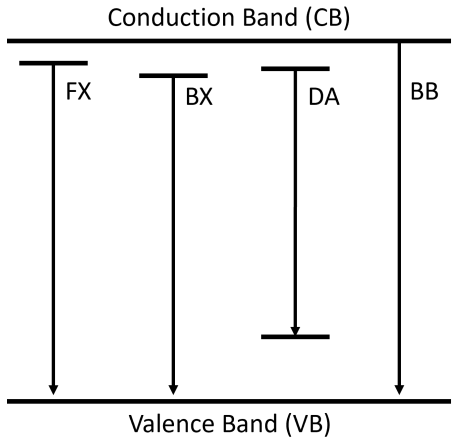

Figure 2.4: Schematic illustration of the different radiative recombination channels which can be present in semiconductors (FX: free exciton, BX: bound exciton, DA: donor to acceptor, BB: band-to-band), while additionally illustrating the temperature dependence of individual recombination channels. Adapted from [82]

for free-to-bound or bound-to-free recombination. We therefore assume, that free carrier recombination is the dominant recombination mechannism present in our samples at temperatures close to 20 °C In the case of band-to-band luminescence, the electron and hole directly recombine from the valence- and conduction band respectively. The resulting photoluminescence peak position thus roughly equals the bandgap of the semiconductor. However, at T$\neq$ 0 °K, the charge carriers reside slightly above the band edges of the valence- and conduction band, due to their thermal energy. Especially in temperature dependent measurements, the final value of the bandgap therefore needs to be temperature corrected.

As discussed in detail in section 1.1, the bandgap of $MAPbI_{(1-x)}Br_x)_3$ and with that the PL peak energy increases for higher fractions of bromide x. This increase is almost linear, being well described by modifying Vegard's law by a small additional bowing factor b, as shown in Figure 2.5.

$$E_g(x) \;=\; E_g^{Br} \cdot x + E_g^{I}(1-x) - x \cdot (1-x) \cdot b \tag{2.1}$$

As prepared samples are sufficiently homogeneous, to use this correlation between the nominal mean composition $\bar{x}$ and the PL peak energy to estimate the composition of a sample simply by measuring its PL energy.

Special Case: Inhomogeneous Samples As described above, electron-hole pairs thermalize to their respective equilibrium state before they recombine. In the case of chemically inhomogeneous $MAPbI_{(1-x)}Br_x)_3$ samples, with bromide-rich and iodide rich domains, the valence- and conductionband energy is spatially inhomogeneous. This implies, that electron-hole pairs will funnel spatially to the region with the lowest bandgap energy within

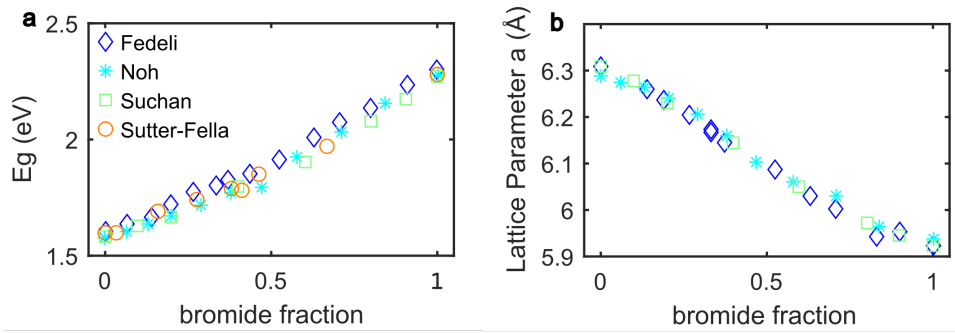

Figure 2.5: (a) The PL peak energy, shown for all compositions increases almost linearly with increasing bromide fraction as seen in our experiments (Suchan et al.) in agreement with literature reports. (b) The pseudocubic lattice parameter a, as obtained from XRD measurements decreases with incresing bromide fraction, in agreement with literature values. A slight deviation of the linear trend, described by a bowing parameter of b = 0.016 was obtained from our experimental data.[23, 29, 85, 86].

their diffusion lengths. As the bandgap scales linearly with bromide fraction, the lowest bandgap region will be the region with the least bromide fraction.

PL emission is stemming solely from phases occupied by charge carriers. The subsequent emission, thus may be severely dominated by any narrow-bandgap region present in the material. It can still be considered band-to-band recombination, but does not give information of the average bandgap and thus composition of the material, but rather of the phase exhibiting the lowest accessible bandgap.

While in inhomogeneous samples, the PL energy can thus not simply be used to obtain the average composition of the sample, it can give complementary information about which phases the charge carriers reside predominantly in. However, it is important to realise, that quantitative estimates are difficult to make with PL alone, as the detected intensity of PL emission at any wavelength needs to be considered to be a combination of the PLQY of that phase and the number of charge carriers which occupy that phase. For phases, spatially within the diffusion length of the charge carriers, they should on first approximation be Boltzmann distributed, solely depending on the energy differences between the phases.[74] In Paper III and IV, this is used to obtain the composition of the emissive phase and a rough estimate of which phase the charge carriers predominantly reside in. However, we also show that quantitative estimates of the fraction that the low energy phase makes of the entire material cannot be made. Phases which are not populated by charge carriers are completely invisible in PL such that no information on these phases can be drawn.

2.4.2 Compositional Information from XRD

Fundamentals of X-ray Diffraction - In a Nutshell In X-ray diffraction, an incident X-ray beam is reflected off of the atomic planes in a crystalline sample. The periodicity of the atomic positions in the crystal, defined by the crystal lattice, leads to an interference pattern in the reflected beam in a similar manner as an optical diffraction grating would with optical light. The reflected X-rays interfere constructively if the Bragg condition is fulfilled, which is the case if the path difference between X-rays reflected off different atomic planes is an integral multiple of the wavelength.

$$n\lambda \ = \ 2 \cdot d_{hkl} sin(\theta) \tag{2.2}$$

Where λ denotes the X-ray wavelength, d_{hkl} is the distance between a specific set of lattice planes described by the Miller indices h,k and l and θ is the incident angle of the X-ray beam with the lattice planes.[87, 88] The recorded peak position is thus determined solely by the size and the symmetry of the unit cell. Following this, the angle at which constructive interference occurs and an XRD peak is detected, is determined by the lattice distance, d_{hkl}, the distance between the atomic planes (hkl).

The X-ray diffraction intensity is determined by the electron density in the unit cell. The intensity of a specific diffraction peak, I_{hkl} is proportional to the absolute square of the structure factor F, which is determined by a sum over the fourier-transform of the electron density f_n of all atoms n, in the unit cell and a phase contribution which is determined by the atomic positions x_n, y_n and z_n in the unit cell.

$$I_{hkl} \ = \mid F_{hkl} \mid^2 = \mid \sum_n f_n e^{2\pi i(hx_n + ky_n + lz_n)} \mid^2 \tag{2.3}$$

Thus, the integrated peak intensity I_{hkl} is directly determined by the crystal symmetry and the atomic positions of the contributing elements. It is therefore sensitive to the entire crystalline material in the sample.

Additionally, the peak width gives information on how perfect the periodic lattice is. In an ideal infinitely large crystal, the perfectly periodic lattice produces sharp peaks. However, in a real crystal, the finite size of the crystal domains may introduce peak broadening. If the domains are very small, typically below a few hundred manometers, there are not enough aligned atoms per plane to produce a sharp diffraction pattern. The peaks therefore show broadening which is described by the Scherrer equation.[89] Beyond the size of the domain, also deviations from the perfect periodicity result in peak broadening. If there is in-homogeneity in the lattice plane distances, positive interference will not just occur at a single angle but at a distribution of angles, corresponding to the distribution of lattice

distances. Peak broadening due to domain size and lattice distance inhomogeneity can be distinguished due to differences in the dependence of the peak widths on the diffraction angle.[90] Inhomogeneity of lattice distances can either be caused by exerted pressure on the crystal e.g. by a lattice distance mismatch between the crystal and the substrate, leading to strained growth which typically relaxes far from the substrate, or by inhomogeneity in the chemical composition, leading to domains with different lattice distances. Both effects are nearly indistinguishable as discussed in Paper III.

Calculating Composition As discussed above, the XRD peak position gives a quantitative measure of the lattice distances. In mixed $MAPbI_{(1-x)}Br_x)_3$ samples, the smaller size of bromide compared to iodide leads to a decrease of the lattice distances with increasing bromide fraction, as discussed in section 1.1. The lattice constant of the solid solution $MAPbI_{(1-x)}Br_x)_3$ can be described by Vegard's law with an additional small bowing factor b of 0.016, as shown in Figure 2.5 b.

$$a_x \;=\; a_{Br} \cdot x + a_I \cdot (1-x) - x \cdot (1-x) \cdot b \tag{2.4}$$

Where a_x, a_{Br} and a_I are the lattice constants of the solid solution, pure bromide and pure iodide perovskites respectively. Using this relation between diffraction angle and bromide content, the position of the XRD peak can be used to obtain the materials average composition.

Special Case: Inhomogeneous Samples In case of spatial inhomogeneity of the bromide to iodide ratio in $MAPbI_{(1-x)}Br_x)_3$ samples, the lattice distances will also vary spatially as can be seen in Figure 2.6 If XRD is measured with a large beam spot, the resulting pattern has to be viewed as an ensemble average of all contributing crystallites in the beam spot. The resulting XRD peak is thus a linear combination of all peaks corresponding to the different lattice distances. To extract the weight fractions of individual phases contributing to the observed pattern, we fit the experimentally measured XRD peaks with a linear combination of 21 generated reference patterns over the compositional range. The reference patterns, $I_{XRDm}(2\,\theta)$, were constructed with composition x_m ranging from 0 to 1 in steps of 0.05 assuming that the XRD peak shapes are equal to the instrumental response function (IRF) at the diffraction angles expected for the specific composition $2\,\theta(x_m)$. With these reference patterns a linear combination analysis was performed to calculate the linear combination coefficients ϕ_m, where the coefficient ϕ_m is the volume fraction of the phase in the sample with composition x_m. This is shown for a $MAPbI_{(1-x)}Br_x)_3$ sample in Figure 2.6 This procedure assumes that the width of the diffraction peaks in the dark and under illumination is dominated by compositional inhomogeneity and neither strain nor size. This assumption is justified in Notes S3 and S6 of Paper III, where from both Williamson–Hall analysis and the analysis of the peak shape, it is shown that peak-broadening is not consistent with changes in the domain size nor strain in the samples under investigation.

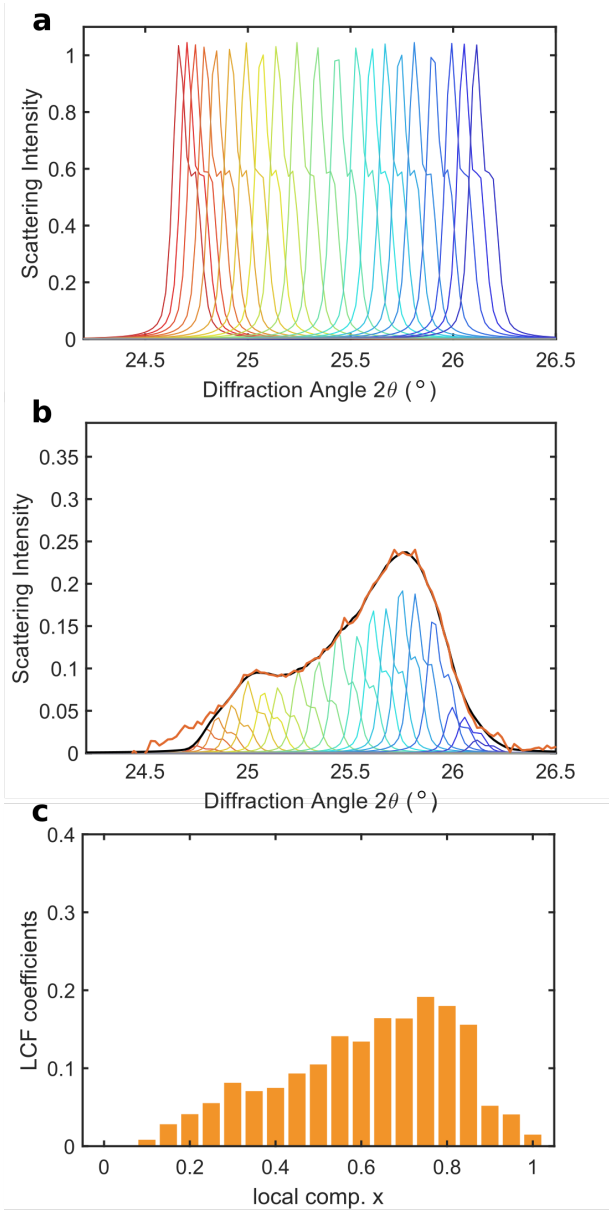

Figure 2.6: (a) The XRD patterns of the 21 compositions used to fit the patterns of inhomogeneous $MAPbI_{(1-x)}Br_x)_3$ films with their linear combinations. (b) Typical pattern of an inhomogeneous $MAPbI_{(1-x}Br_x)_3$ film, here a phase segregated film with average composition x = 0.6. (orange), the LC-fit (black) and the contributing patterns (color according to a) (c) the obtained linear combination coefficients are shown in a phase distribution histogram.

Challenges While X-ray diffraction can give information on which phases are present in a sample as well as give an estimation of their volume fraction, there are challenges in obtaining a valid result.

After hitting the sample at an angle θ, X-ray intensity is scattered in a scattering cone, resulting in a full circle with 360°when reaching the detector plane. Only grains which are aligned which are aligned to fulfill the Bragg condition for the specific angle θ contribute to the diffraction pattern. Furthermore, even with a 2D detector array, most often only a portion of the circle can be detected. In the experiments in Paper III and IV, the field of view was approximately $\pm$ 30°. Thus, typically less than 1 % of the grains contribute to the detected signal. The azimutal angle η at which a diffraction spot is formed on the diffraction circle depends on the orientation of the lattice planes with respect to the incoming X-ray beam. If certain chemical compositions would exhibit preferred orientations, e.g. align with the substrate, their corresponding diffraction spots would not be randomly distributed at the azimutal arc, but cluster at a certain degree η. If this angle is out of the field of view it might be that the volume-fraction of this compositional phase is underestimated. To verify that the orientation does not significantly alter our results we confirmed that the integrated peak intensity does not change during all our reversible experiments.

Further, as we consider mixed $MAPbI_{(1-x)}Br_x)_3$ samples, we need to consider that Br and I have different electron densities and thus different atomic form factors. This means that bromide has a smaller scattering cross-section than iodide. Equation 2.3 can be used to calculate the expected scattering intensities for the pseudo-cubic 200 reflex of $MAPbBr_3$ and $MAPbI_3$.

At 9.2 keV the ratio scales with

$$I^I_{hkl}/I^{Br}_{hkl} \;=\; 171/132 \rightarrow I^{Br}_{hkl}/I^I_{hkl} \;=\; 0.78 \tag{2.5}$$

The formfactor scales linear with the bromide fraction. The ratio of intensities can therefore be interpolated linearly in order to comparing phases with composition x = 0.6 and x = 0.8. The error made when comparing these two phases is roughly 4 % which can be neglected as it is below the accuracy of the measurement. However, when comparing phases in the composition extremes, the error might be up to 10 %. Such that if a phase is estimated to have a fraction of 1 %. This may be over- or underestimated by 10 % in the cases of pure Br and pure I phases. We deem that in the accuracy of the measurements this will not change the results and have for simplicity reasons assumed that the form-factor stays constant for all phases during the phase segregation.

2.5 The Observer-Effect in Real-Time In-Situ Measurements

In a perfect *in-situ* experiment, one aims to probe the evolution of material properties without interfering in the process itself. However, commonly an observer effect occurs where the observed system is disturbed by the act of observation. A common example is the checking of the pressure of a car-tire. If the pressure is measured by letting air out, the air-pressure has been changed by the act of measuring it. Usually the aim of careful experimentation is to reduce this effect to insignificance. However, in *in-situ* measurements this is especially difficult, as continuous observation is necessary and any observer effect will commonly build up during the process.

When measuring PL, light is used to measure material properties. However, in the case of light induced phase segregation the light will usually induce the phase segregation. This is an extreme case of the observer effect, where the probe is inducing the effect to be studied. This poses several problems. first of all, it is not possible to measure the PL and the tr-PL of the pristine material. If a short integration time is chosen to be able to get a glimpse on the state prior to phase segregation, the spectra will be noisy while still being a superposition of the pristine state and some degree of phase segregation. Thus the optical properties, such as the charge carrier lifetime of the pristine material are still relatively unknown. This circumvents to analyse how the phase-segregation process may be dependent on these properties. Even at later stages of the phase segregation the duality of the excitation to be both a probe and inducing the phenomena, means that there is a constant competition between temporal resolution and signal-to noise. Longer integration times lead to a lack in time resolution. Going to higher excitation densities accelerates the phase-segregation process, such that this is not a viable scheme to increase the temporal resolution.

A different scenario occurs when measuring X-ray diffraction. While the incident X-ray photons do not directly induce phase-segregation, the X-ray beam is still far from a pure probe beam. Incident X-ray photons induce additional charge carrier densities in the material, such that the measured emission will consist of a juxtaposition of X-ray excited optical luminescence (XEOL) and PL. At high X-ray dosages we observed ionizing effects, which lead to continuous destruction of the sample. We discuss the loss of halide ions in section 3.3 which strains the crystal lattice and by this alters the peak position of the diffraction reflexes. Even at lower X-ray dosages, it has been reported, that exposure to X-rays induces defects which degrade the opto-electronic properties of MHPs.[91] We have observed that the introduction of X-ray induced defects alters the phase segregation process and slows down its kinetic. This is an especially dangerous example of the observer effect, as the X-ray induced defects are not detectable with XRD itself. Thus even though no effect was observed while testing for X-ray damage by long exposures, X-ray damage at the defect level occurred which in turn alters the process under investigation.

Chapter 3

Summary of Results

3.1 Evaluating Performance Losses in Mixed Bromide-Iodide Perovskite Solar Cells

The ability to modify the bandgap of a semiconductor is a necessary but not sufficient condition to enable a wide range of applications. The key requirements for efficient device performance is the ability of a material system to maintain high material quality, compositional homogeneity, and stability as well as good electrical contacting across the entire bandgap range. In Paper I, we therefore do a correlation between the tunable bandgap of metal halide perovskite solar cell devices and their performance metrics. For this we analyze the trends from over 45 000 experimental data sets of metal halide perovskite solar cell devices. This unique dataset is openly available in 'The Perovskite Database'. beyond individual reports, the gained insights allow to generalize the progress and current limits of the device performance of metal halide perovskites. While we focus on solar cell metrics, due to their abundant availability, we deem that the results have more general importance as qualities such as low radiative loss, stability and reliability are universal across a range of different applications.

The analysis of the experimental data sets reaffirms the astonishing performance of metal halide perovskites solar cells with an absorber bandgap around 1.6 eV. However, at bandgaps below 1.55 eV, as well as above 1.7 eV, the performance is less optimal. To evaluate the influence of the halide mixture on the solar cell performance of wide bandgap solar cells, we analyze the power conversion efficiency η, the short circuit current density J_{sc} and the open circuit voltage V_{oc}, with respect to the theoretical limit, given by the Schockley-Quaisser limit, shown in Figure 3.1

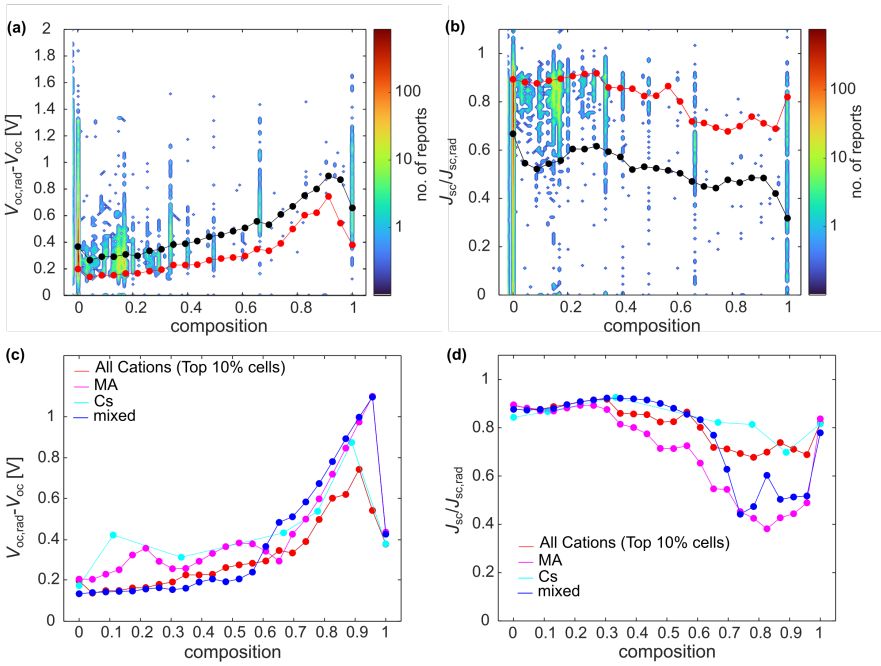

Figure 3.1: Comparison of the device performance depending on the Br/(Br+I) composition. a) The dependence of $V_{oc,rad} - V_{oc}$ on the composition Br/(Br+I), shows the previously reported increase in voltage loss for higher bromide contents and a sharp decrease of the loss for pure bromide samples. The black line shows the mean of all devices, while the red line shows the mean of the top 10 % of the devices. b) Similarly the J_{sc}/J_{SQ} shows an a decrease in current for bromide contents above 0.3 and a sudden increase in current for the pure bromide devices. c) The same general behaviour of $V_{oc,rad} - V_{oc}$ can be seen independent of the cation. d) The cation dependence of J_{sc}/J_{SQ} shows that the general tendency of a decreased current at high bromide contents is independent of the cation. However, mixed cation devices show an initial increase in the current up to bromide contents of 0.4-0.5 and only a decline at even higher bromide contents.

While the voltage loss ($V_{oc,rad} - V_{oc}$) only slightly increases for samples with a bromide fraction up to 50 %, it increases steeply for higher bromide contents. A similar decline is visible in the current, $J_{sc}/J_{sc,rad}$ for high bromide fractions. Interestingly, pure bromide perovskites show only a slightly increased voltage loss and almost the same J_{sc} than their pure iodide counterparts.

Mainly three dominant effects have been discussed in literature to be responsible for the suboptimal performance of mixed halide perovskites with large bromide fractions:

1. Quenching at extraction layers
2. Non-radiative Shockley-Read-Hall recombination
3. Phase segregation

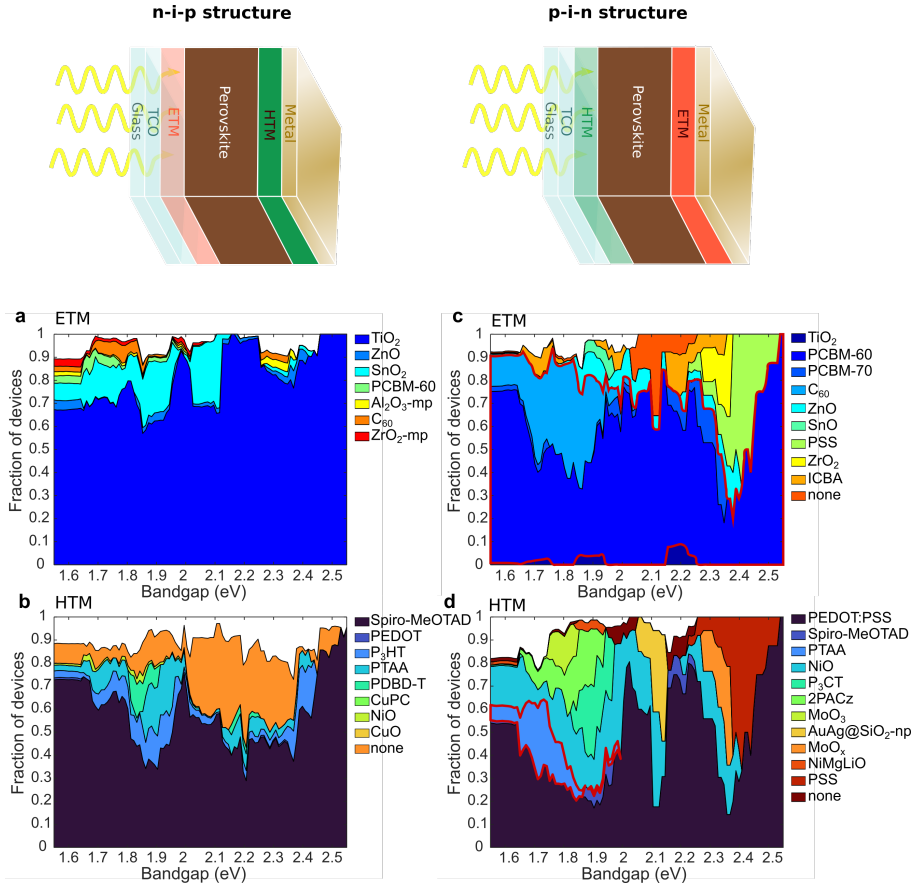

Figure 3.2: The fraction of devices using the most commonly used transport materials are shown in dependence of the device's bandgap. a) shows the fraction of devices using one of the 7 most commonly used ETMs in p-i-n structures. Likewise b) shows the fraction of devices using the most commonly used HTMs in p-i-n structures. Accordingly b) and d) shows the use of ETMs and HTMs in n-i-p structures. 'none' signifies if no HTL was used in the device stack. C_60 derived ETMs and PTAA as HTM, is highlighted by a red border.

In paper I, we set out to discuss these three effects and their role in the observed losses in V_{oc} and J_sc in wider bandgap perovskites, between 1.6 en 2.2 eV. We find that the utilized extraction layers are only seldom optimized separately for each bandgap. Instead, for metal halide perovskites with an n-i-p layerstack, TiO_2 and $Spiro - MeOTAD$ are still the most used extraction layers, originally used for the archetypal $MAPbI_3$ solar cells. In p-i-n devices a larger variety of extraction materials can be found. However, PCBM-60 and PEDOT:PSS are clearly dominating. SCAPS simulations done by Christian Wolff, show that the reliance on unoptimized extraction layers results in an increasing V_{oc} pinning for higher bandgap materials. We therefore conclude that a part of the V_{oc} loss, specifically the part which continuously increases for higher bromide fractions, yielding a larger V_{oc} loss even for the pure bromide devices.

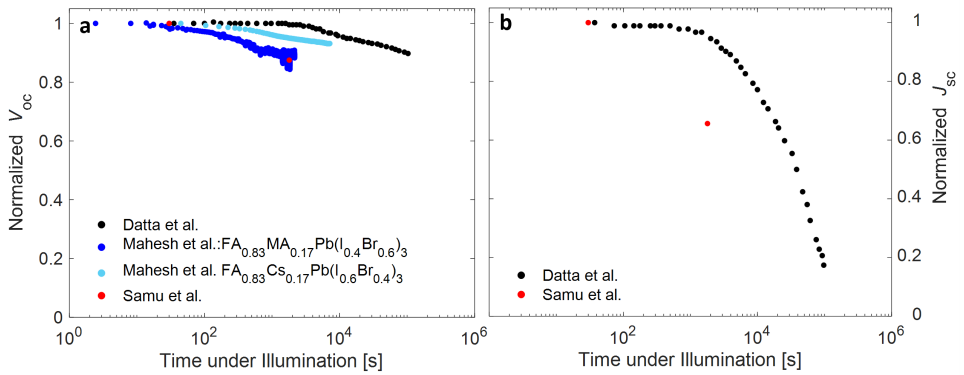

Figure 3.3: The evolution of V_{oc} (a) and J_{sc} (b) measured during phase segregation of mixed perovskite films, clearly shows that J_{sc} is significantly more effected by phase segregation than V_{oc}. Data from [39, 40, 42], digitized with WebPlotDigitizer.

The characteristic recovery of the solar cell metrics for pure bromide devices however indicates, that a large portion of the losses are distinctly connected to the mixing of the halides rather than the bandgap alone. Strikingly the intrinsic opto-electronic quality, approximately following the PLQY, follows the same qualitative evolution with the bromide fraction as the solar cell device metrics, which indicates that the majority of the losses are connected to the optoelectronic quality of the absorber.

In a chemically unstable material, reported J-V curves result from a mixture of pristine effects, such as the layer stack and the intrinsic material properties as well as dynamic effects such as phase-segregation, light soaking, degradation and hysteresis. Apart from the discussed losses in pristine devices, light induced compositional instability is thus a necessary factor to consider when evaluating the solar-cell performance of mixed (I, Br) metal halide perovskites. During the light-induced phase segregation of mixed halide perovskites, iodide rich domains form. These newly formed iodide rich domains have a smaller bandgap, compared to the surrounding mixed material. Thus, it has been observed that nearly all charge carriers funnel into the newly emerging iodide-rich domains. However, only a few studies did a detailed analysis of the effect of the photo-segregation into iodide rich and bromide rich domains on solar cell efficiencies.[39–43]

A summary of the *in-situ* reports, tracking the evolution of V_{oc} and J_sc during phase segregation is shown in Figure 3.3 a. In all reports a decrease in the V_{oc} within the first 15-30 min, of around 10 to 20 % of its initial value can be seen, which is on the order of 70-130 mV.[39, 42] Thus light induced phase segregation may contribute to the observed increase in V_{oc} loss for devices with higher bromide content. Mahesh et al. conclude that this rather small V_{oc} loss related to phase segregation is due to two effects counteracting each other. While the formation of lower bandgap domains reduces the Fermi-level splitting and thus pins

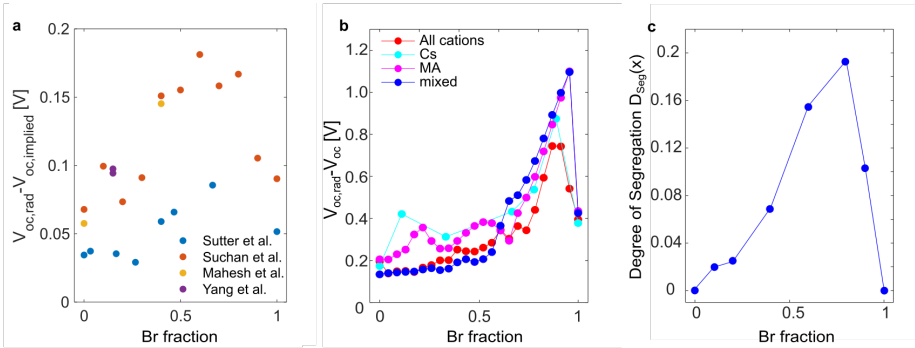

Figure 3.4: The $V_{oc,rad} - V_{oc,implied}$, calculated from PLQY ($Q_e^{lum}$), the open circuit loss $V_{oc,rad} - V_{oc}$, and the photo-instability quantified by the degree of segregation D_seg, follow the same dependence on the bromide fraction in the perovskite absorber.

the V_{oc} this effect may be reduced if the radiative efficiency of the lower bandgap material is significantly higher than that of the pristine mixed material.

In contrast, the J_{sc} is severely affected by the phase segregation with a decrease of over 80 % of the initial value, as shown in Figure 3.3b. This has been rationalized by the isolated nature of the newly formed I-rich domains. As they are isolated, they are assumed to act as trap states, preventing charge transport to the electrodes, thus causing a severe loss in J_{sc}.[40] The experimental evidence thus clearly shows that phase-segregation is detrimental for the solar cell performance. Furthermore, it highlights, that while the V_{oc} is only marginally affected, J_{sc} decays severely

It is noteworthy that both, the dependence of the PLQY and the in Paper III discussed dependence of the photo-instability on the bromide content qualitatively agree with the observed dependence of V_{oc} and J_{sc} on the bromide content. The instability of mixed halide perovskites with compositions of x > 0.2 has been shown to due gradually increase with bromide content and exhibits a maximal instability at x = 0.9 when only a small fraction of iodide is added to pure bromide perovskites.[29] The agreement of all three traces, shown in Figure 3.4 hints to the interconnectiveness of the defect density, the photo-chemical stability and the device performance, as we discuss in detail in Paper III. Peña-Carmargo et al. pointed out, that initial phase-segregation at a very low level may appear as increased defect density.[92] Such that the apparently increased defect density visible in the PLQY of bromide rich samples could also be a disguised intial phase-segregation. This agrees with the observed higher FWHM in X-ray diffraction reflexes of bromide rich samples.[13, 51, 85, 93] Vice versa, the importance of defects and especially halide vacancies for the kinetics of phase-segregation has recently been highlighted. Such that increased instability may as well be connected to the high defect density of mixed halide perovskites.[29, 49, 75, 76] This highlights that defect density and chemical instability cannot be viewed as two disconnected topics, but are instead highly correlated.

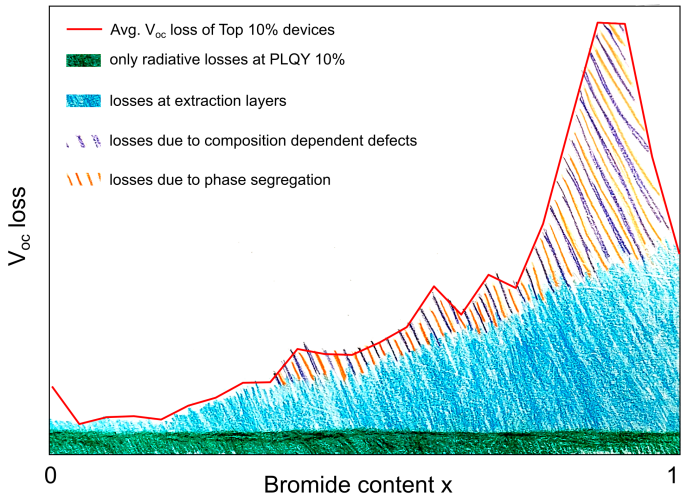

Figure 3.5: Cartoon indicating the contribution of different loss mechanisms to the total observed loss in V_{oc} as a function of the bromide content in the MHP absorber layer.

From the analysis of the vast amount of reported solar cell device data collected in 'The Perovskite Database' we were able to highlight the contribution of unoptimized extraction layers as well as the interconnected effect of poor opto-electronic absorber quality and chemical photo-instability of mixed halide perovskites with high bromide contents, as shown in Figure 3.5.

3.2 Towards a Better Understanding of Phase Segregation

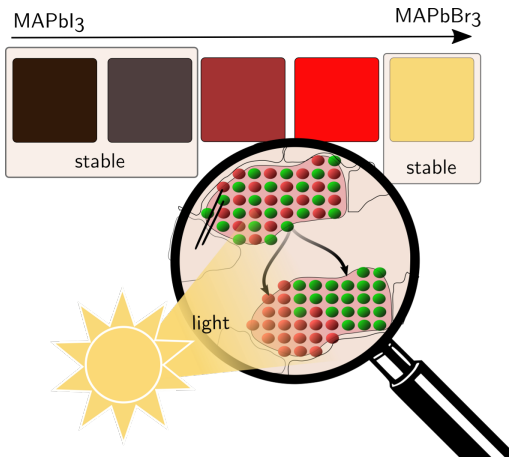

Figure 3.6: Under illumination the mixed halide bromide-iodide perovskites undergo a phase segregation in which iodide and bromide segregates. The mechanism of phase segregation is yet to be understood. In this thesis I aim to shine light on the photo-induced phase segregation mechanism in metal halide perovskites. Adapted from Paper II[7]

Metal-Halide Perovskites (MHPs) have attracted tremendous attention due to their steep rise in power conversion efficiency to now over 25.2 % [17] The ease of bandgap tunability by varying the halide ratio of bromide, iodide and chloride in e.g. $MAPb(I_{1-x}Br_x)_3$ perovskites [23] makes these materials interesting for tandem solar cells [17] or LEDs over the whole visible range [94, 95]. Detrimental for device performance is the light-induced phase segregation as discussed in Paper I. However, the details determining the segregation are not well-understood. We used PL-microscopy as well as multimodal PL and XRD experiments to monitor and analyze the phase segregation process in detail.

The measurements presented in Papers II, III and IV were conducted on $MAPb(I_{1-x}Br_x)_3$ perovskites, spin coated on top of microscope glass cover slides by Carolin Rehermann (HZB) as described in the methods sections of the respective papers.[7, 29]

3.2.1 Halide Segregation: A Multistage Process

By employing spatially resolved real-time *in-situ* PL measurements (Paper II), we revealed an even more complex evolution of the phase segregation pathway than previously reported. This complex evolution of PL for a $MAPb(I_{0.4}Br_{0.6})_3$ sample at $-20\ ^{\circ}C$ is shown in Figure 3.7a, on a logarithmic time scale. Within the first few seconds of illumination, we found a very rapid formation of a short-lived intense photoluminescence band. The photoluminescence shifts from 1.72 eV to 1.65 eV over the course of 1 minute, resembling the emission of almost pure $MAPbI_3$. The appearance of such a transient photoluminescence

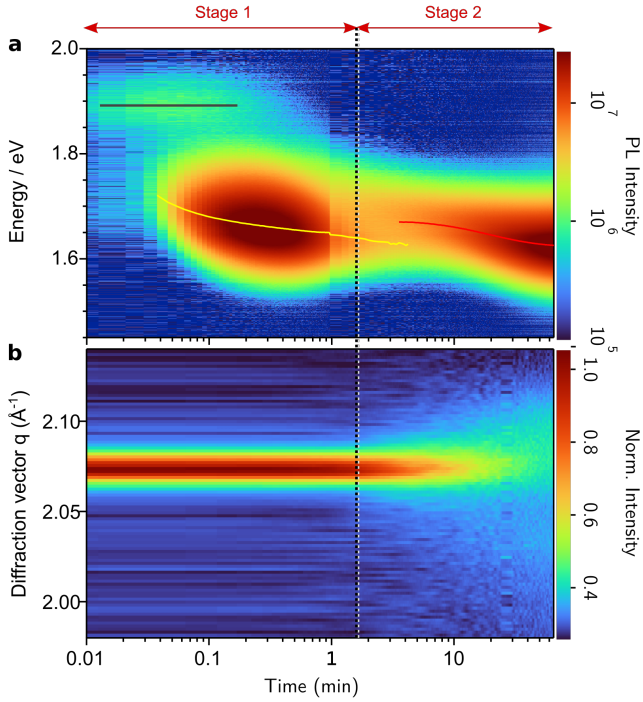

Figure 3.7: The evolution of the photoluminescence (a) and (200) X-ray diffraction peak (b) of a $MAPb(I_{1-x}Br_x)_3$ sample at -20 $^\circ C$ during light-induced phase segregation are shown in a color plot, where the color indicates the peak intensities. The PL energy shifts rapidly from the initial peak to a temporary PL peak at lower energies in the first stage of the process. The fitted peak energies are shown as black and yellow traces, respectively. Changes in the (200) diffraction peak are observed only in the second stage. Here the (200) diffraction peak broadens while the final low energy PL peak evolves (red trace). The segregation process is slowed down at -20 $^\circ C$, allowing stages 1 and 2 to be resolved in both PL and XRD. Note that the time axis is plotted on a logarithmic scale.

peak during phase segregation was later confirmed by other studies.[72, 96] Our results allowed us to distinguish two stages of phase segregation. Stage 1 marks the transition from high to low emission energy within the first few seconds. Whereas in stage 2, the initial low energy peak disappears as a new low energy peak grows in.

Using multimodal PL and XRD in Paper III, we showed that during the first stage of phase segregation, the 200 XRD peak remains unchanged as shown in Figure 3.7 b. This means that the structural material properties remain intact in stage 1, despite the apparent changes in PL. We therefore proposed that small nanoscopic iodide-rich clusters form initially. Being very small and relatively few, they do not constitute a large volume fraction of the sampled material, which explains the unchanged XRD patterns. While this initial phase segregation is invisible in XRD, it is clearly visible in PL. This underscores the unique sensitivity of PL to the tiniest traces of narrow-bandgap domains arising from charge relaxation to the lowest accessible energy state immediately after excitation. Interestingly in stage 1, a rise time is visible in the time resolved photoluminescence (TRPL) traces, which is a direct

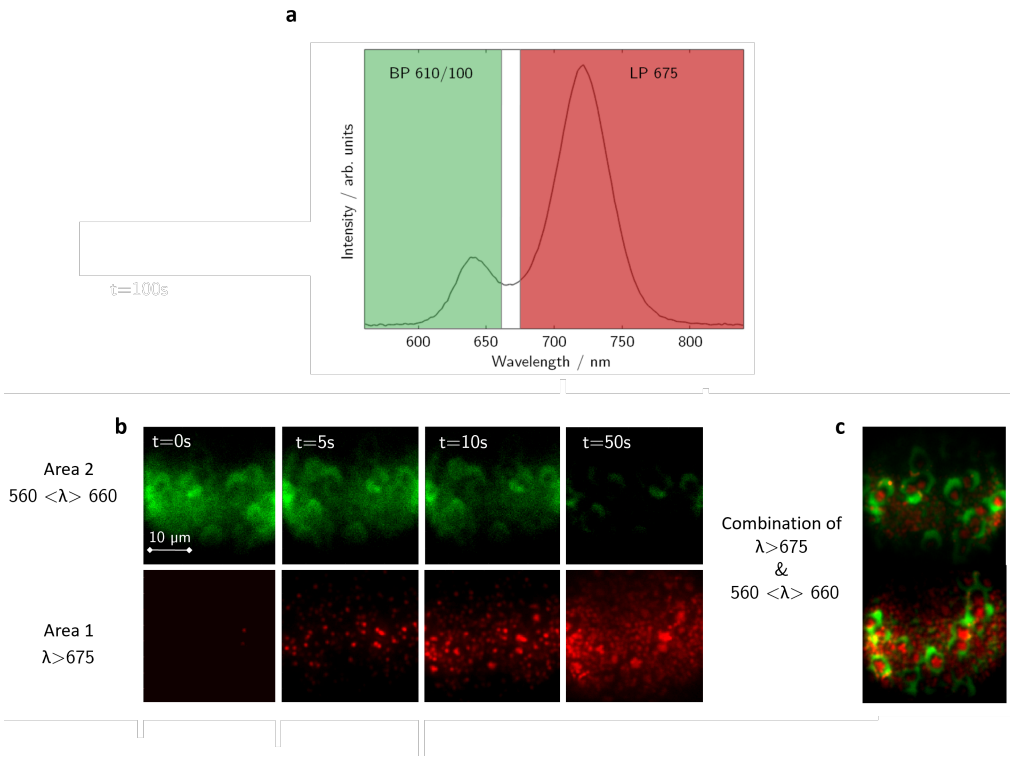

Figure 3.8: Spatial evolution of the photoluminescence intensity of a $MAPb(I_{0.5}Br_{0.5})_3$ sample at 20 $^{\circ}C$. a) To distinguish between the emission of the mixed phase and the newly formed iodide-rich phase, bandpass (BP) and longpass (LP) filters are inserted into the detection path. b) shows the evolution of the high-energy emission (green) and the dual-energy emission (red) at two different regions of the same sample. (c) After 50 s, the filters were switched and the images taken at 50 s and 55 s were superimposed. Adapted from Paper II[7]

observation of the charge carrier funneling, as seen in Figure 3.9

To study the spatial evolution of PL, we used PL microscopy imaging. Images were acquired with specific bandpass filters inserted into the detection path, allowing us to choose between imaging the evolution of the initial high-energy emission or the growing low-energy emission, as shown in Figure 3.8 a. The high and low energy emission is followed separately in area 2 and area 1 for 50 s, as shown in figure 3.8 b. After 50 s, the filters were switched and a final image was taken with the opposite filter. This allows the creation of an overlay image as shown in Figure 3.8 c.

We found that the low emission is initially due to small diffraction-limited regions that subsequently grow into larger islands during phase segregation, confirming our hypothesis. Interestingly, the low energy emission starts in spots that originally have a low relative PL yield, pointing to the interesting role of defects in the phase segregation process, see Figure 3.8 b.

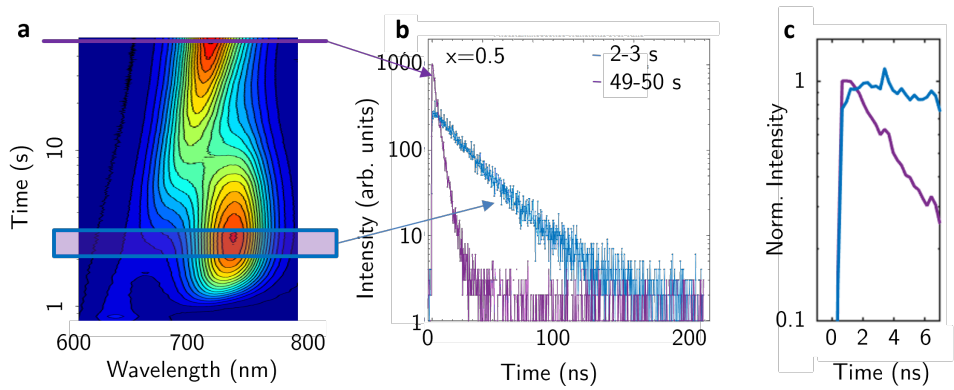

Figure 3.9: TRPL is measured with an integration time of 1 s during phase segregation of a MAPb($I_{0.5}Br_{0.5}$)$_3$ sample. The TRPL trace collected from 2 to 3 s of illumination time corresponds to the transient peak growing in stage 1, marked in blue in a) The TRPL trace collected from 49 to 50 s of illumination time originates from the final PL peak, marked in purple. b) The relative PL yield is similar at both times. The comparison of the PL decay kinetics integrated over all wavelengths in stage 1 and in the final time interval shows a reduction of the PL lifetime during phase segregation accompanied by an increase of the initial PL amplitude. c) A closer look into the first 6 ns of the PL decay reveals a rise time of the PL trace of 2-3 seconds, which we propose to be caused by charge carriers from the still mixed majority phase into the highly emissive nanoscopic iodide-rich domains. Adapted from Paper II [7]

Based on our results, we propose a multi-stage phase segregation mechanism. In stage 1, isolated iodide-rich domains of nanoscopic size are formed. All carriers in the vicinity are funneled into these iodide-rich domains as they have a smaller bandgap. In stage 2, the iodide rich domains grow into larger islands and the majority phase is depleted of iodide.

3.2.2 Comparison to Current Models and Their Limitations

Several models have been formulated to explain the light induced phase-segregation. A consensus has been reached, that the phenomenon is charge carrier driven. Thermodynamic models, such as the 'Gap-model' or the 'Polaron-model' introduced in section 1.3.2 rely on the charge carrier contribution to the free energy to make the segregates state energetically favourable. The free energy of mixing, F is the energy difference between the mixed state and the segregated state. If it is positive, this signifies that energy can be gained by segregation. In Paper III, we used the experimental data to quantitatively probe the hypothesis, that the charge carrier contribution to the free energy can rationalize the phase segregation. We therefore calculated the energy difference of the experimentally measured mixed and phase segregated state according to the proposed models and evaluated the obtained energy difference. For this at first a quantitative description of the phase segregated state is needed to subsequently calculate the energy difference between the mixed and the segregated state, relying on published values for the composition dependent free energies.

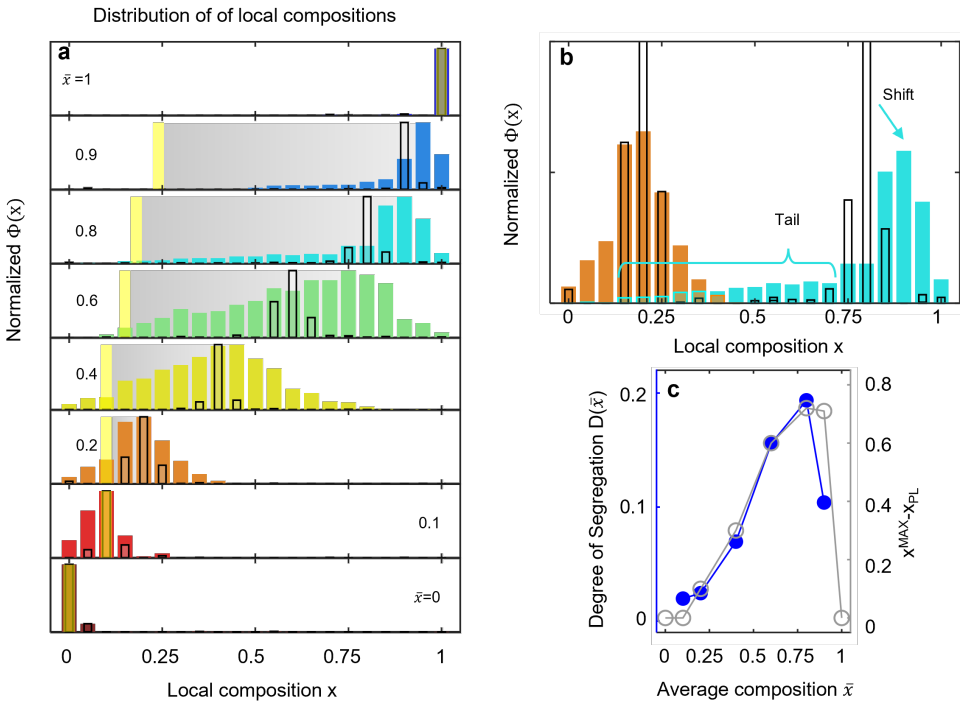

Figure 3.10: (a) shows the compositional phase distribution for samples with bromide fractions between x = 1 and 0. The initial phase distribution is shown as empty bars and the equilibrated phase distribution after segregation is shown in colours. The yellow bars represent the composition of the emissive phase as obtained from PL. (b) shows a zoom of the 'mirror' compositions x = 0.2 and x = 0.8. In this representation the asymmetry becomes apparent. While the sample with x = 0.2 shows a symmetrically broadend phase distribution, the sample with x = 0.8 shows the formation of and iodide rich tail and a bromide enrichment of the majority phase. (c) shows the degree of segregation, $D_{seg}(x)$ a quantitative metric to compare the segregated state despite qualitatively different phase distributions. Samples with high bromide fractions are shown to be more probe to segregate. The agreement between the final $D_{seg}(x)$ and the difference between the composition of the majority phase and the emissive phase in which the charge carriers reside point to the 'gap-model' to be key in the underlying segregation mechanics. Reproduced from Paper III[29]

Quantification of Phase Segregation In a first step we therefore developed a quantitative approach to describe the final phase segregated state. Previous reports have in part be conflicting in quantifying the amount of material that undergoes phase segregation. Different results between different measurements are likely due to different different ways to quantify phase-segregation. The amount of a new 'low energy phase formed', the decrease in the original peak-height or even the intensity of the low-energy PL band have been used to estimate the progress of segregation. Furthermore the dependence of the final segregated state on environmental and processing conditions has hindered a meaningful comparison.

In this work, we therefore use a linear-combination analysis of reference patterns with different bromide to iodide compositions to obtain the volume fraction of each compositional phase present in the film, as explained in section 2.4.2. We hence know which composi-

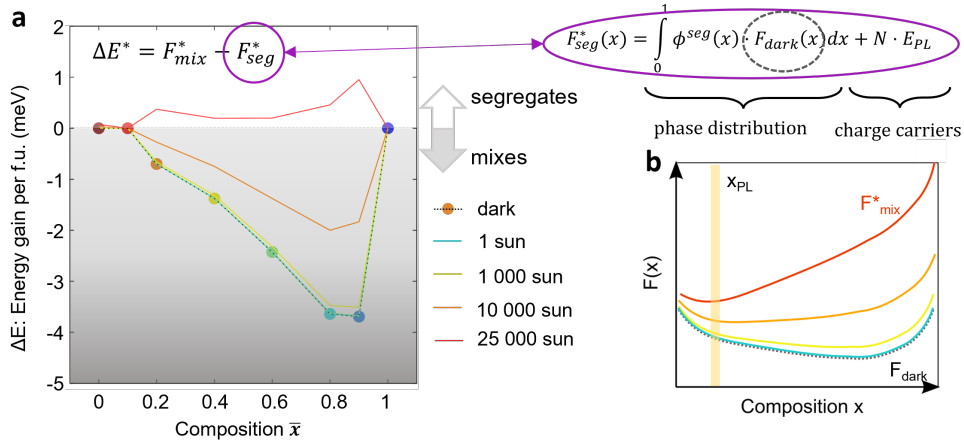

Figure 3.11: Calculation of the energy gained by segregation for different excitation densities. (a) shows the calculated energy gain as a function of sample composition at various excitation densities. At excitation densities corresponding to 1 sun, the charge carrier contribution is not sufficient to rationalize the experimentally obtained segregated phase distribution. The segregated state only becomes energetically favourable at high charge carrier densities corresponding to 25 000 suns. The free energy of mixing in the segregated state can be calculated by using the reported free energy of mixing in the dark, F(x), weighed by the experimentally obtained phase distribution in the segregated state $\phi_{seg}(x)$, together with the energy of the charge carriers. b) shows a sketch of the free energy of mixing in the *gap-model* as a function of the sample composition for different excitation densities. The sketch illustrates, that the free energy at 1 sun excitation is almost identical to that in the dark. Only at higher excitation energies does the charge carrier term $N \cdot Eg(x)$, contribute significantly to the free energy of mixing. Adapted from Paper III[29]

tional phases form and in what quantity. With this approach we are able to quantitatively describe the distribution of compositional phases during phase segregation. Through this we were able to show that up to 70 % of the material changes it's composition during phase segregation for a sample with x = 0.8.

To further quantify how much a sample segregated independent on the shape of the distribution of compositional phases, we propose to use the degree of segregation D(x,t), which we introduced in Paper III. It is a measure of how much the compositional phase distribution differs from its original state. This quantitative figure of merit makes it possible to compare the phase segregation of different samples such as different bromide fractions but potentially also different cation systems in a quantitative manner.

Quantitative Comparison of Experimental Data with Theoretical Models As the next step the previously reported models are quantitatively assessed in Paper III. To calculate the difference in free energy between the mixed state and the phase segregated state, we use the experimentally obtained compositional phase distribution and the reported free energy for each composition. The charge carrier contribution to the free energy is calculated according to the 'Gap-model'.[50, 68, 74] From the energy difference we obtained, that the final

phase segregated state cannot be explained alone by consideration of the free energies. The mixed phase is thermodynamically preferred in the absence of charge carriers. It is however proposed, that the energy reduction of the charge carriers which is possible due to bandgap variations in the mixed state is enough to make the segregated state thermodynamically favourable. However, the experimentally observed changes in the compositional distribution are too severe to be induced solely by the energy of the relatively low number of charge carriers excited at moderate light intensities (1 sun). We therefore conclude that only the first stage of phase segregation, at which the majority phase has not yet changed significantly but small iodide rich domains form, can be explained by the proposed models. Here the charge carriers funnel to the nanoscopic iodide-enriched domains, which leads to local charge carrier densities high enough to rationalize local charge carrier densities, see Figure 3.11. However, to explain the second stage of phase segregation, at which reorganisation of ions in the majority of the material occurs, a kinetic model is needed.

3.2.3 Rationalizing the Consequences of Photo-Induced Ion-Mobility

In Papers III and IV, we propose to consider photoinduced changes in the material to explain the entirety of the phase segregation process. The unique softness of metal halide perovskites implies that material properties such as ion-mobility cannot be assumed to stay constant in the course of irradiation.

Especially halide vacancy densities have been singled out as a key ingredient determining the photo-segregation process. The role of halide-vacancies as an accelerating factor for photo-segregation has recently been reviewed by Tian et al..[97] It is generally agreed upon, that ion-migration, which is the key prerequisite for both segregation and recovery, predominantly occurs via vacancy-mediated diffusion of halide ions.[28, 35, 40, 49, 76, 98] During the initial stage of phase segregation, it has been indicated by Tiede et al. and Suchan et al. that the pre-existing vacancy density determines the location where the segregation initializes as well as the segregation kinetics.[7, 76] This highlights the importance of the defect density in the phase segregation process, especially when looking at the initial stage of segregation.

While the importance of the pre-existing halide vacancy density has been widely discussed, photo-induced vacancies via the weakening of Pb-I bonds need to be considered as well to understand the continuous segregation process.[31, 34, 35, 98] Photo-induced vacancies have been proposed repeatedly and are thought to be the major reason behind the reported dependence of the ion mobility on the excitation density.[31, 35, 98–102] Recently photo-induced vacancies have been suggested to be an underlying factor determining phase segregation.[75]

In the case of mixed halide perovskites, bandgap inhomogeneities and charge carrier fun-

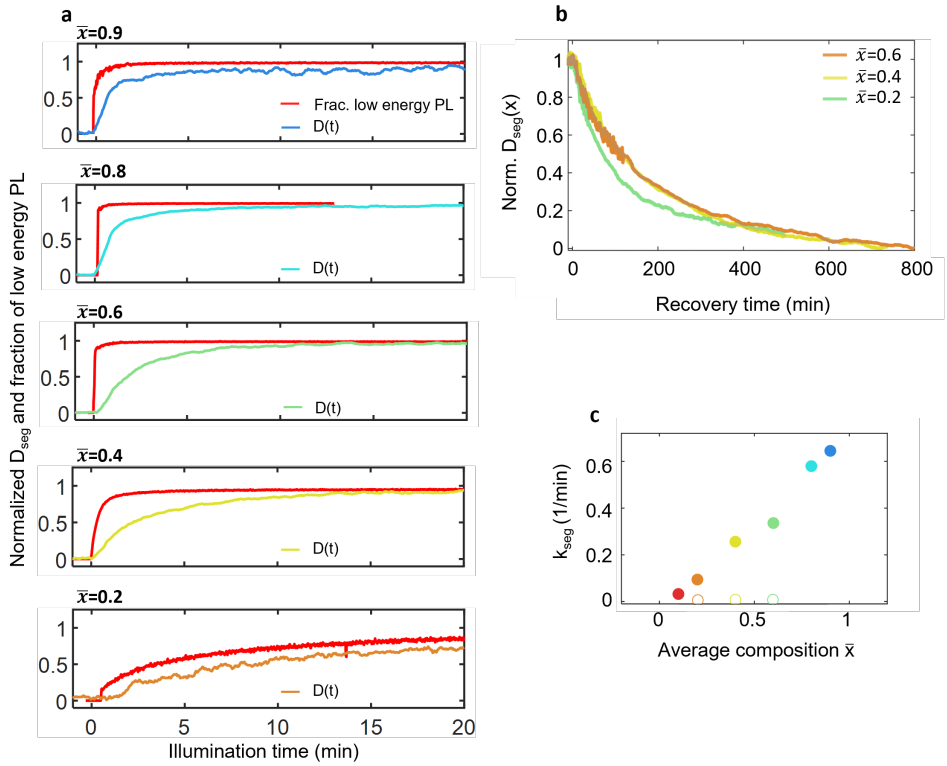

Figure 3.12: a) shows the fraction of low energy PL in the total PL emission, indicating the shift from high energy to low energy emission (red traces). In comparison, the degree of segregation $D_{seg}(x)$ is shown (colored lines). The shift in PL is quite fast, almost independent of the sample composition. The evolution of the degree of segregation, a quantitative measure of the progress of phase segregation, is much slower. This implies that carrier funneling into nanoscopic iodide-rich domains precedes large-scale phase segregation. Comparing the traces for high bromide content (x = 0.8 and 0.9) with those for low bromide content (x = 0.2 and 0.4), it can be seen that the phase segregation process is significantly accelerated for samples with higher bromide content. In contrast, the recovery kinetics shown in (b) are more independent of the composition. Rate constants for both segregation and recovery for selected compositions are obtained and shown in (c) as empty and full circles, respectively. Adapted from Paper III [29]

neling leads to inhomogeneous charge carrier densities. Such an inhomogeneous charge carrier density implies that photoinduced effects primarily occur in the iodide-rich domains. Further, the concentration of charge-carriers in such "hot-spots", leads to a higher probability of the creation of halide vacancies there, than expected for irradiation with 1 sun. In Paper III, we observed experimentally, that the phase segregation rate for samples with a high bromide fraction is much higher than for samples with a low bromide fraction, as shown in Figure 3.12 a and c. In contrast, we see that the recovery rates if the samples are left in the dark after phase segregation, are independent of the bromide ratio, shown in Figure 3.12 The recovery process is believed to be purely driven by diffusion. Its composition independence thus indicates, that the pristine ion-mobility is independent of the bromide fraction, in agreement with theoretical predictions. This raises the question, why

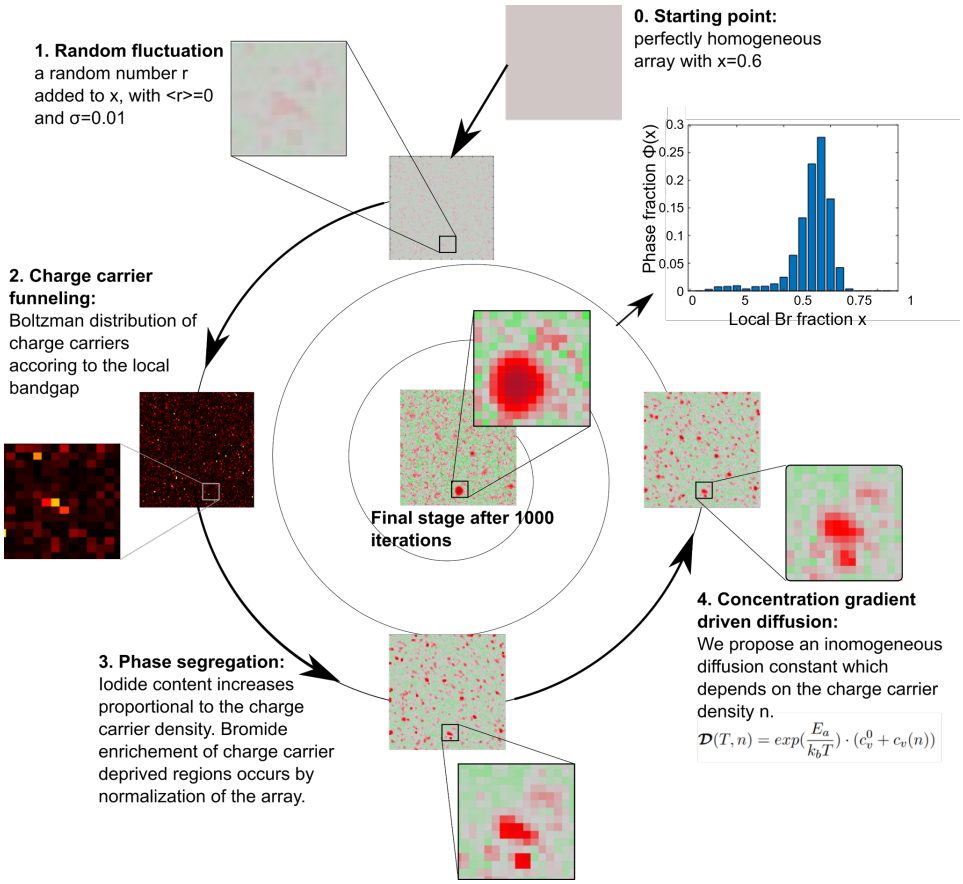

Figure 3.13: Sketch of the simulation steps. Reproduced from Paper IV [29]

the phase-segregation kinetics are accelerated in samples with high bromide fractions. We propose that this observed acceleration of segregation in Br-rich samples is a light-induced effect, rather than due to generally higher ion mobility in Br-rich samples. The stronger local charge-carrier concentration in Br-rich samples leads to higher local vacancy and interstitial densities. From the phase-distribution of the final segregated state, we estimate as a lower limit a 10-fold higher local charge carrier concentration in Br-rich samples compared to I-rich samples. However, we anticipate, that this difference is even larger in the initial stage of phase-segregation, when the I-rich domains are below the detection limit of XRD. Higher spatial inhomogeneity in the vacancy density in Br-rich samples can thus well rationalize the faster segregation in the Br-rich samples.

To further investigate how this mechanism leads to the gradual phase-segregation, we looked into the temperature dependence of the phase-segregation process by *in-situ* XRD and PL in paper IV. We utilized the same experimental setup and methodology developed for the

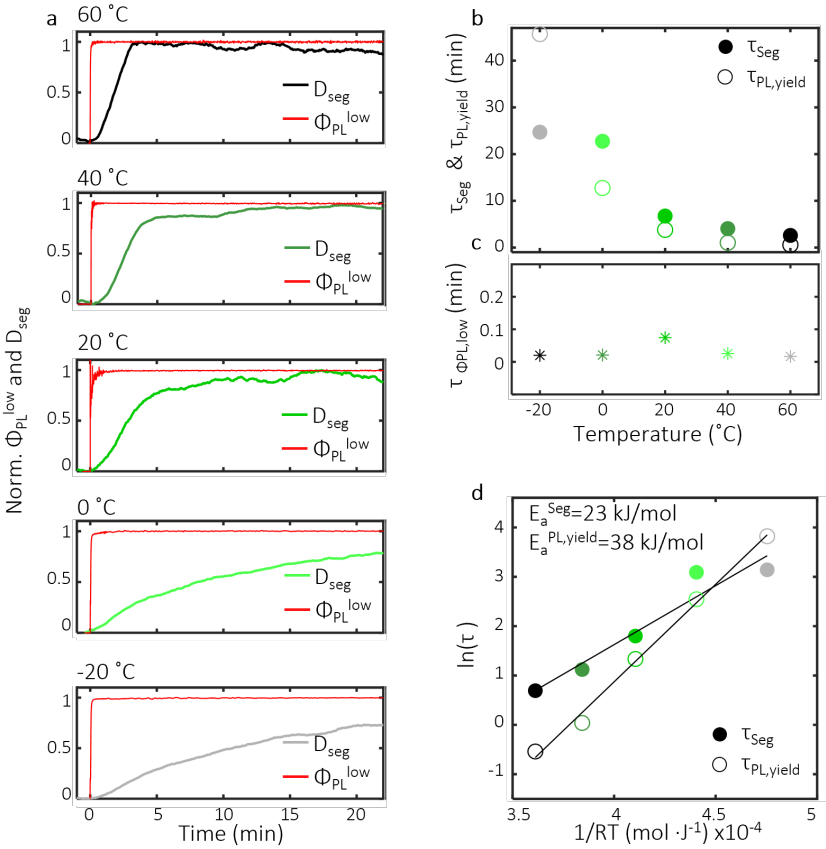

Figure 3.14: a) shows the kinetic evolution of the fraction of low energy PL, which signifies the emergence of nanoscopic iodide rich domains and the charge carrier funnelling therein (red traces). The evolution of the degree of segregation, giving a quantitative estimate of the progress of phase segregation is shown in colour. It becomes apparent, that the kinetic of the fraction of low energy PL (red traces) is very fast and independent of the temperature. This is further shown in the temperature independence of the respective segregation time constants $\tau_{\phi PL,low}$. The kinetic of the phase segregation temperature activated. The segregation constant τ^{Seg} decreases with higher temperature, respectively. An activation energy of $E_A = 23kJ/mol$ can be calculated from the kinetics of phase segregation. The increase in PL yield, a common denominator for phase segregation is shown alongside. A similar but different activation energy can be calculated. Reproduced from Paper IV.

composition dependent phase segregation discussed in paper III. We further developed a simple 2D numerical model of the phase segregation, including our insights from paper III. In the model we assume a temperature independent segregation mechanism interconnected to a temperature dependent chemical gradient driven diffusion. The most unique feature of the model is that we included both a pre-existing vacancy density, which is homogeneously distributed, c_v^0 and a photo-induced vacancy density which depends on the local charge-carrier density $c_v(n)$ and is thus laterally inhomogeneous. The diffusion constant,

$\boldsymbol{\mathcal{D}}$ therefore becomes dependent on the local charge carrier density n.

$$\boldsymbol{\mathcal{D}}(T) \;=\; exp(\frac{E_a}{k_b T}) \cdot c_v \rightarrow \boldsymbol{\mathcal{D}}(T,n) \;=\; exp(\frac{E_a}{k_b T}) \cdot (c_v^0 + c_v(n)) \qquad (3.1)$$

The temperature dependence of the equilibrium phase distribution and the PL energy as well as their evolution was analyzed to distinguish between thermally and photo-activated aspects of the phase segregation process. Experimentally we observed that the first stage, at which nanoscopic iodide rich domains form is mostly photo-activated and not temperature dependent. The quick appearance of small iodide rich clusters has previously been seen in PL-microscopy in Paper II and is apparent in the simulation presented herein.

The appearance of these domains is simulated to occur independent of the set temperature in agreement with the experimental results.

In contrast, the substantial ion reorganization, which occurs in the second stage shows strong temperature dependence. As a result the segregation kinetics of the second state, $D_{seg}(x,t)$ and $I_{PL}(x,t)$ as well as the final phase segregated compositional phase distribution $\phi(x)$ show clear temperature dependent behavior. By simulating the extended phase segregation in dependence of temperature we were able to rationalize this by temperature activated ion diffusion. A lack of diffusion at low temperatures slows down the extended phase segregation.

The results presented herein provide important insights into the mechanism of the phase segregation process. They corroborate that the temperature independent 'gap-model' can explain the initial formation of nanoscopic iodide rich domains. However, the extended phase segregation of the majority of the material is determined by continuous illumination and an equilibrium of photo-activated segregation and thermally activated gradient-driven diffusion. These results pinpoint to the high ion diffusivity, related to the low activation energy for the formation of halide vacancies to be the key challenge in metal halide perovskites.

3.2.4 Conclusions on the Phase-Segregation Process

With Papers II to IV presented in this thesis we were able to contribute significantly to the understanding of the mechanism underlying the phase segregation process. We found that the phase segregation process is a more complex process than previously assumed. In a first stage, small nanoscopic iodide-rich domains form, which only in a second stage grow to larger iodide-rich islands, leading simultaneously to a bromide enriched majority phase. While the first stage is well described by previously proposed mechanism, such as the 'gap-model', an explanation why how the material continuous to segregate was lacking.

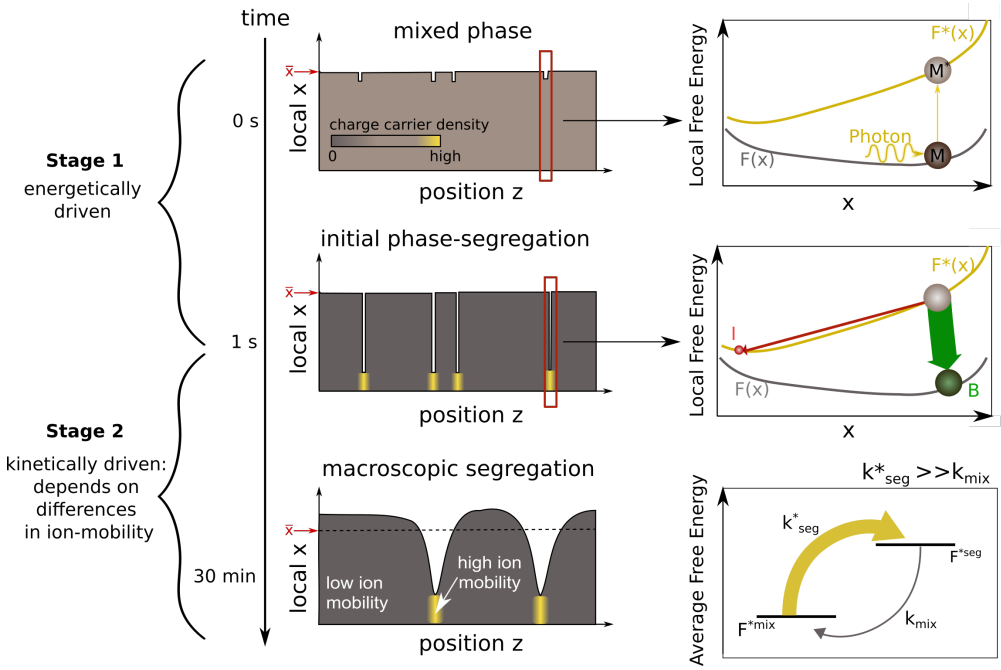

Figure 3.15: The phase segregation process is a multistage process. At the first stage, nano-scopic iodide rich domains grow. Their formation is locally energetically favorable as indicated in the energy schematics (right side). The presence of I-rich domains (red ball) in close vicinity to charge-carrier generation allows for the reduction of charge-carrier energy via funneling to such low bandgap, I-rich domains. The bromide rich phase (green ball) is thus depleted of charge-carriers and is effectively in the dark. In the second stage, the phase segregation continuous. Larger iodide rich domains form which leads to bromide enrichment of the majority phase. This stage cannot be rationalized by previously reported thermodynamic models. Inclusion of chemical gradient driven diffusion and photo-induced inhomogeneous vacancy densities are needed to explain the extended phase segregation. Adapted from Paper III [29]

In this work we proposed a kinetic model based on the interplay of a temperature independent, photo-activated segregation mechanism and gradient driven diffusion. We were able to implement the model in a 2D numerical simulation and where thus able to show that such a kinetic model can reproduce both stages of photo-segregation. Initial formation of small iodide-rich domains, independent of temperature, and a subsequent temperature dependent continued phase segregation. With this we extend understanding of the phase segregation beyond merely its initial phase. Beyond this we are certain that our gained knowledge on the interdependence of charge-carrier density and ion mobility will be applicable to various photo- and charge-carrier induced instabilities observed in metal halide perovskites.

3.3 Sensitivity of Mixed Metal Halide Perovskites to Hard X-ray Irradiation

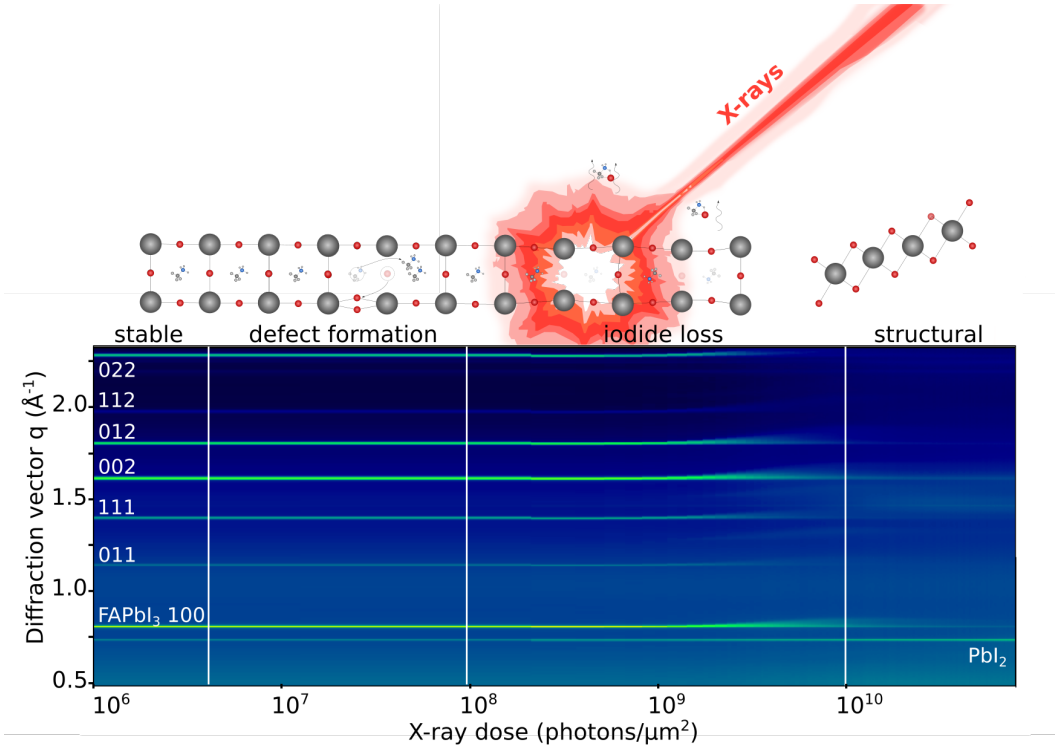

Figure 3.16: Metal halide perovskites are X-ray sensitive. Exemplary, this is shown on the evolution of the XRD patterns of $FAPbI_3$, shown as a colour map as a function of the X-ray dose. Upon exposure to X-rays, different degradation mechanisms can be observed depending on the X-ray dosage. We here differentiate into 4 regimes: At very low X-ray dosages, the material's properties stay stable. However, already at X-ray dosages above $\approx 10^6\ photons \cdot \mu m^{-2}$, degradation of the optoelectronic properties occurs (not visible in XRD). At even higher X-ray dosages the material strains, likely an effect related to the organic cation. Beyond this, iodide starts to become volatile and finally, the perovskite lattice collapses giving rise to the formation of PbI_2.

A multitude of different characterization techniques such as X-ray diffraction (XRD), X-ray beam induced current (XBIC), X-ray fluorescence (XRF) and X-ray absorption spectroscopy (XAS) rely on X-rays as a probe. However, the X-ray sensitivity of the studied material limits their applicability, as the studied material properties may be altered by the X-ray exposure.

To assess the validity of the obtained results a profound understanding of the interaction mechanism between X-rays and MHPs is therefore necessary.

Beyond X-rays involved in materials characterization, a range of possible applications of MHPs require X-ray radiation hardness. Due to MHPs' low weight in combination with

reported high proton and electron hardness, the potential of MHPs for space photovoltaics has been discussed.[103] However, besides proton radiation also X-ray radiation is common in space. Especially solar flares contain significant X-ray photons, such that the X-ray flux may momentarily increase by several orders of magnitudes. Further MHPs are considered promising candidates for X-ray detectors.[2] Here it would be a large benefit if the detector would withstand large X-ray dosages.

Several studies have investigated the hardness of MHPs concerning protons, electrons as well as intense laser light.[32, 103–108]

In the case of electron irradiation, it has been shown, that, the organic cation is affected, if present, and even prone to evaporation.[104–106] This leads to a lattice contraction. At a later stage, PbI_2 is formed. In the case of inorganic perovskites, such as $CsPb(I_{0.4}Br_{0.6})_3$, Pb^0 is shown to form as a degradation product.[107, 108] Intense optical illumination has been proposed to induce Frenkel-defects, at which a bound halide-vacancy and interstitial is formed.[32] The formation of such photo-induced Frenkel pairs is proposed to induce a deformation of the organic sublattice, which ultimately leads to a contraction of the entire perovskite lattice.[32, 109]

The effect of X-rays on MHPs is much less studied, despite XRD being among the most employed characterization techniques.[91, 110–112] In 2020, Stuckelberger et al. showed, that the optoelectronic properties of the material are already affected prior to the evaporation of iodide at an assumed dosage of 10^{11} photons·µm^{-2}.[91] Structural properties are reported to be more resilient towards X-ray exposure.[110, 111] Still, a congruent account of the interaction between X-rays and MHPs over a large range of dosages, taking into account the degradation of both optical and structural material properties is missing.

3.3.1 Exploring the X-ray Dose-Dependence of X-ray Degradation

To analyze the effect of X-rays on the optoelectronic and structural material properties over a wide range of X-ray dosages, we conducted a multimodal study in which a $MAPb(I_{0.4}Br_{0.6})_3$ sample was exposed to a total of $6.6{\cdot}10^8$ photons·µm^{-2}with an energy of 12.8 keV over the course of 32 minutes. This corresponds to a total dose of $1.36 \cdot 10^{-6}$ J ·µm^{-2}. The exerted X-ray dose on the sample is calculated from the continuously measured beam intensity I_0 and the beam profile and the measurement geometry.

From X-ray diffraction, we obtain the effect of X-rays on the crystal lattice. Furthermore, as the scattering intensity of a peak is determined by the amount of material in that phase, as discussed in section 2.4.2, we can follow the disappearance and appearance of crystalline phases.

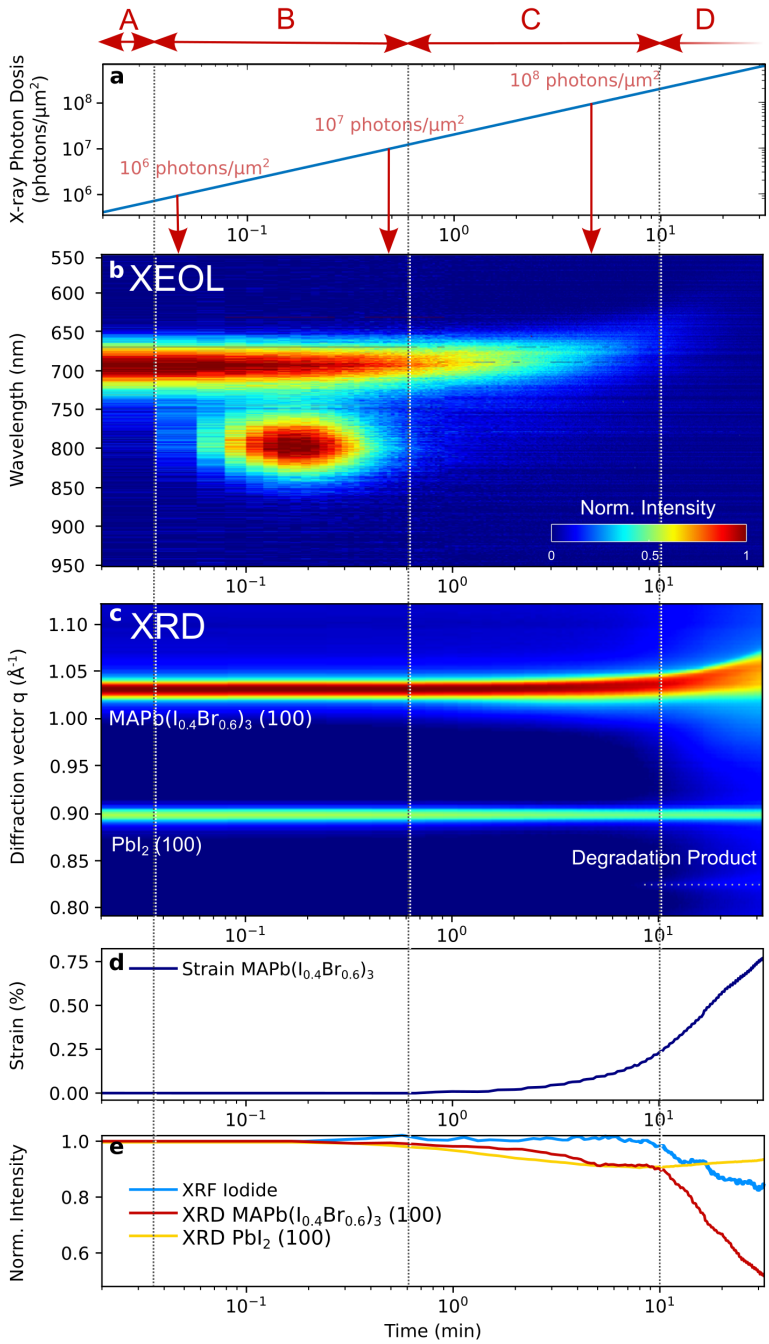

Figure 3.17: Different stages of interaction between X-rays and $MAPb(I_{0.4}Br_{0.6})_3$, from A: 'no-effect' to significant structural degradation in D, as followed with XEOL, XRD, and XRF. a) X-ray excited optical emission shows the decay of the optoelectronic properties alongside the emergence of a temporary low energy emission peak in stage B. b) shows the X-ray diffraction peaks of $MAPb(I_{0.4}Br_{0.6})_3$ and PbI_2. While little changes in PbI_2 are visible, the $MAPb(I_{0.4}Br_{0.6})_3$ (100) reflex broadens and shifts to higher q. d) shows the strain associated with the shift of the $MAPb(I_{0.4}Br_{0.6})_3$ (100) reflex. d) Compares the integrated peak intensity of the $MAPb(I_{0.4}Br_{0.6})_3$ and the PbI_2 (100) reflexes and the iodide content in the film, extracted from the iodide L-lines in XRF.

The X-ray fluorescence signal (XRF), gives a quantitative measure of the elements present in the film, irrespective of the compound they are in. Unfortunately, the experimental setup did not allow to measure both iodine and bromine simultaneously with sufficient statistics. We therefore, concentrated on accurately measuring the iodide loss from the I-L lines and the amount of lead from the Pb-L lines.

Utilizing the optical emission due to X-ray photo-excitation, we analyse the effect of X-rays on the optoelectronic properties, without adding any additional bias through illumination of the sample with optical light, as described in section 2.3 A single X-ray photon can excite approx. 500-1000 charge carriers, due to multi-step cascade processes. Despite the difference in excitation, the emitted light can be analyzed analogously to PL and very similar conclusions can be drawn from XEOL and PL.

In Figure 3.17 the accumulated X-ray photon-dosage is shown in comparison to the evolution of XEOL (b), XRD (c), calculated strain (d) as well as the integrated peak-areas of the $MAPb(I_{0.4}Br_{0.6})_3$ (100) reflex, the PbI_2 (100) reflex and the iodide L-lines from XRF (e) over time in a logarithmic scale. The logarithmic time scale allows us to visualise processes on different time scales. It becomes apparent, that the 'no-effect' regime, stage A, lasts only for $\approx$ 1 s at an X-ray flux of $3.4{\cdot}10^5$ photons$\cdot\mu m^{-2}\cdot s^{-1}$ with 12.8 keV.

The XEOL color map shows the luminescence intensity (color scale), over the emission wavelength (y-axis) and the time (x-axis). The luminescence intensity is proportional to the ratio between radiative recombination to non-radiative recombination. The implied V_{oc} of a solar cell scales directly with this ratio.[113] Thus the luminescence intensity is a good figure of merit to judge the optoelectronic quality of a material. As can be seen in Figure 3.17, the luminescence intensity decays quickly within the first minute of X-ray exposure (stage B). Furthermore, already in the first few seconds, a new low energy peak appears. This is likely due to either emissive defects or nanoscale I-rich domains, similar to those observed during optical illumination during phase segregation, as discussed in section 2.3. The similarity of the emission signal in the initial phase upon optical illumination and X-ray exposure is striking. However, a further investigation of the evolution of XEOL for different halide compositions would be needed to differentiate defect emission and nanoscale I-rich domain formation.

Comparing the emission signal to the evolution of the X-ray diffraction peaks shows that at such low X-ray dosages as present in stage B, no structural changes can be observed. Neither the formation of strain nor any changes in the phase distribution can be seen. The lattice compresses only upon further X-ray exposure (stage C). Compression of the lattice has previously been proposed, both for the formation of Frenkel-pair defects as well as for the evaporation of the organic cation.[104–106, 109] As the amount of iodide in the film (light blue trace in Figure 3.17d), stays constant throughout stage C, we deem it unlikely that changes in the halide composition cause this strain.

Even further X-ray exposure for over 10 minutes, however, starts to lead to the evaporation of iodide. The lattice is further strained and a severe reduction of the $MAPb(I_{0.4}Br_{0.6})_3$ phase is observed. Simultaneously the PbI_2 phase slowly starts growing. The severe reduction of the $MAPb(I_{0.4}Br_{0.6})_3$ 100 reflex intensity cannot be explained by the loss of iodide from the perovskite phase alone. After 30 min of X-ray irradiation, only 20 % iodide has evaporated making up only 7 % of the scattering intensity, while the $MAPb(I_{0.4}Br_{0.6})_3$ scattering intensity has decreased by 50 %. Interestingly, as visible in the color map of the X-ray diffraction, the diffuse background increases at this stage and shifts from dark blue to a lighter blue. This indicates, that a significant fraction of the $MAPb(I_{0.4}Br_{0.6})_3$ phase is transformed into an unknown amorphous phase. Furthermore, a new, unidentified, crystalline phase forms, which has distinct diffraction peaks at q = 0.828 Å, 1.678 Å, and 2.1806 Å, neither expected for PbI_2, $PbBr_2$, MAI nor MABr.

3.3.2 Impact of X-ray Sensitivity on In-Situ Measurements

3.3.2.1 Degradation of Radiative Efficiency Increases Photo-Stability

As discussed in section 3.3.1, the radiative efficiency of MHPs decays quickly upon exposure to X-rays, in agreement with recent literature.[91] While this decay of the radiative efficiency is visible in XEOL, no measurable structural changes accompany it. Thus we rationalized, that the decay is most likely connected to the creation of defects or the creation of a few nanoscopic I-rich domains. In both cases, their volume fraction needs to be sufficiently small to not influence the ensemble average structural properties.

The induced changes in the radiative efficiency can be shown to be a long-lasting effect. We exposed distinct regions (# 1-6) of two nominally identical $MAPb(I_{0.5}Br_{0.5})_3$ samples to different X-ray dosages covering 3 orders of magnitudes from $2{\cdot}10^6$ photons·µm^{-2} to $4{\cdot}10^9$ photons·µm^{-2}, as shown in the procedure scheme in Figure 3.18 Several hours after the exposure, a clear dependence of the photoluminescence yield on the X-ray dosage is visible, as measured by ex-situ photoluminescence microscopy, shown in Figure 3.19 a.

After the X-ray treatment, the entire first sample is exposed to optical light at 453 nm, with ≈100 mW·cm^{-2} to induce the photo-induced phase segregation process. The phase segregation is followed by *in-situ* XRD, similar to the experiments presented in papers III and IV. To follow the evolution of the XRD pattern without inducing further degradation effects with the X-ray beam, the X-ray beam was severely attenuated to a flux of $1.2{\cdot}10^4$ photons·µm^{-2}·s^{-1}.

All treated areas as well as two untreated areas are measured in sequence over the time of 50 min, to ensure the same conditions for all areas. This results in an additional X-ray photo dose on the sample due to the XRD measurements of $3.8{\cdot}10^5$ photons·µm^{-2}. As this is one

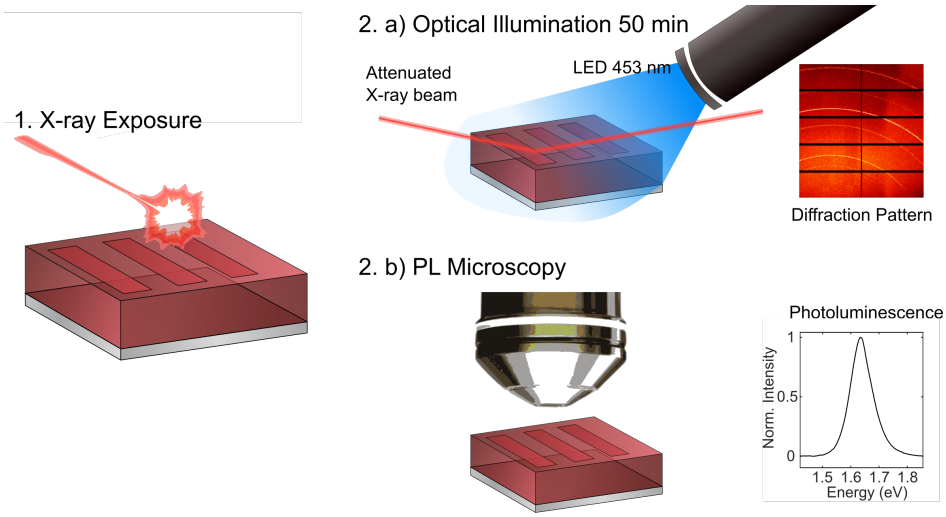

Figure 3.18: Sketch of the X-ray treatment setup and procedure. In the first step, 6 areas of the sample are exposed to X-rays with dosages from $2{\cdot}10^6$ photons·µm^{-2} to $4{\cdot}10^9$ photons·µm^{-2} on two identical samples. Subsequently, in step 2a, one sample is exposed to optical illumination by an LED with center wavelength of 453 nm, to induce phase segregation. The phase segregation is followed by measuring X-ray diffraction with an attenuated beam on each treated area and two untreated areas, sequentially. Several hours after the X-ray treatment, the second sample is analyzed with PL microscopy in step 2b. By using PL microscopy, the treatment areas can be resolved and analyzed separately.

order of magnitude less than the onset of X-ray induced optoelectronic changes (stage B), shown in Figure 3.17, we are confident that the measurements were done in the 'no-effect' region, A, when following the phase segregation.

Non-treated areas of the sample show the expected phase segregation. The original peak broadens upon illumination and a broad distribution of phases is established quickly, as expected from previous studies, described in detail in Papers III and IV. Treated areas however, show significantly improved photo-stability. Samples that prior to the optical illumination were exposed to an X-ray dosage of approx. $4{\cdot}10^8$ photons·µm^{-2} show only a slight broadening upon illumination with optical light. XRD patterns of area 4 and 5, exposed to more than $2{\cdot}10^9$ photons·µm^{-2}, show peak broadening already prior to the optical illumination. We, therefore, conclude that around 10^8 photons·µm^{-2} lies an optimum, at which the phase segregation is nearly omitted and on the other hand the X-ray exposure has not yet led to detectable structural degradation.

We rationalize the decreased PL intensity with the creation of X-ray induced defects, increasing the non-radiative recombination rate. A decrease in photoluminescence yield in a solar cell absorber material, leads to a decrease in Quasi-Fermi-Level splitting and thus causes a loss in the open circuit voltage, V_{oc}.[113] The V_{oc} loss through the radiation damage

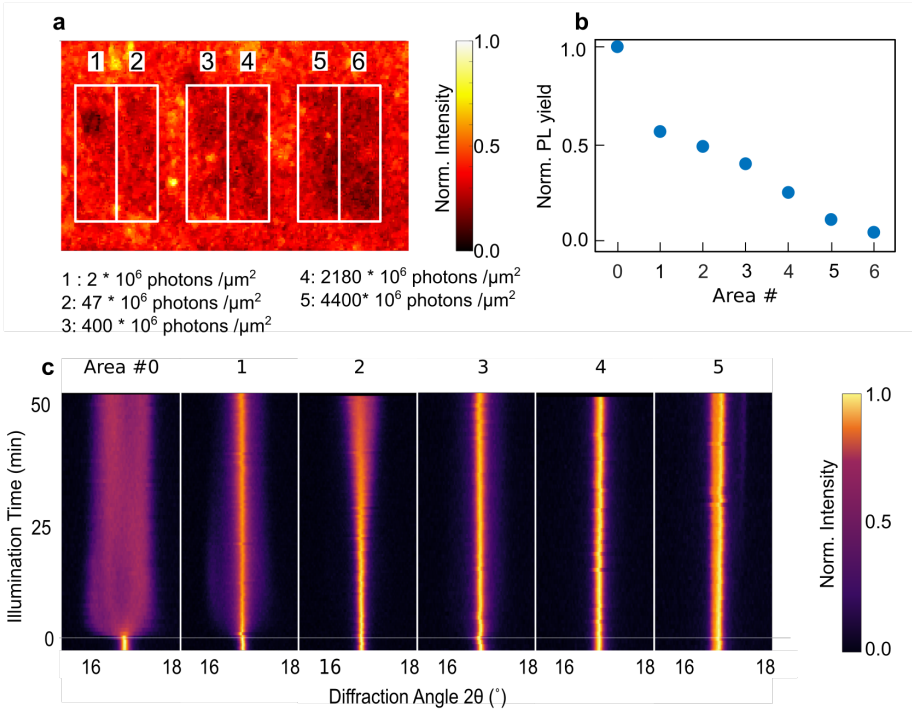

Figure 3.19: a) shows the decrease of the normalized photoluminescence intensity of a MAPb($I_{0.5}Br_{0.5}$)$_3$ sample for regions exposed to increasing X-ray doses ranging from $2{\cdot}10^6$ photons·µm^{-2} to $4{\cdot}10^9$ photons·µm^{-2}. The photoluminescence intensity was measured ex-situ several hours after X-ray exposure. b) shows a photoluminescence microscopy map of the general treatment region with the 6 treatment areas. The X-ray dosage for the treatment is increasing with increasing area number. Already in this representation, it becomes evident, that the relative PL yield decreases with increasing X-ray exposure dosage. c) Shows the evolution of the 200 diffraction reflex of such treated areas when exposed to optical light at 453 nm. The spots treated with higher X-ray dosages show improved photo-stability. However, area 5 shows peak broadening already prior to illumination with optical light, likely due to further X-ray damage.

is therefore given by:

$$V_{oc}^{ini} - V_{oc}^{fin} = -kT/qln(Q_e^{lum,ini}) + kT/qln(Q_e^{lum,fin}) \tag{3.2}$$

The absolute external quantum efficiency Q_e^{lum} is not known, as the setup is not calibrated for this. However, Q_e^{lum} and the relative PL yield are connected by a setup dependent factor. This factor will cancel out if only looking at a difference in V_{oc} .

$$\rightarrow V_{oc}^{ini} - V_{oc}^{fin} = -kT/q(ln(PL^{int,ini}) - ln(PL^{int,fin})) \tag{3.3}$$

A decrease in the relative PL yield of one order of magnitude therefore corresponds to a decrease in the open circuit voltage of 60 mV.

The creation of X-ray-induced defects is irreversible within hours. This stands in contrast to the reversibility of phase segregation, despite the resemblance of initial stage of X-ray-

degradation to the initial stage of phase segregation. From the observed photo-stabilization of $MAPb(I_{0.5}Br_{0.5})_3$ samples after exposure to X-rays, we conclude that defects play a deciding role in the phase-segregation process. Deliberate creation of the right kind of defects could thus be a viable path to omit phase segregation by sacrificing only a small portion of the solar cell's efficiency

3.3.2.2 Validity of Reported Data

The herein presented results highlight that X-ray degradation is a key issue to consider when employing X-ray-based characterization techniques at any X-ray dose. Defects are shown to be created already at low X-ray doses of 10^6 photons·μm^{-2}, much earlier to the apparent degradation of the structural properties above 10^7 and 10^8·μm^{-2}.

This discovery has severe implications for the interpretation of a range of *in-situ* measurements on MHPs. Despite the widely accepted notion, that MHPs are X-ray sensitive, X-ray stability is often not sufficiently considered when reporting X-ray based *in-situ* measurements. Looking more closely at reports that use X-ray diffraction to characterise light-induced phenomena, it is clear that several reports do not comment on X-ray degradation at all.[13, 47, 62] Other reports focus only on negligible decrease of the intensity of the perovskite reflex [53] or negligible increase in PbI_2 as a measure of stability.[32, 51, 63] Interestingly, even though as stated, the reported diffraction patterns show no increase in PbI_2 peak-area, a decrease in the PbI_2 peak-area can be seen if a closer look at the patterns is taken.[51, 63] A similar decrease in the PbI_2 peak-area is observed in our result in stage C of X-ray degradation. Our results clearly show, that X-ray degradation occurs at X-ray photon dosages several orders of magnitude lower than those at which an increase in PbI_2 peak area is observed. Therefore, it cannot be excluded that the observed behaviour in those studies has been influenced by the X-ray exposure. The evolution of the light-induced phase segregation, which is strongly determined by the defect density, may be especially sensitive to the effects of X-ray exposure. However, other changes in the structural properties of MHPs have also been shown to be dependent on defect density, such as the phase transition temperature between the tetragonal and orthorhombic phases.[114] Against this background, our results show that more careful considerations are needed even when only structural properties are measured, as structural properties and defects in MHPs have to be viewed as interdependent.

The X-ray diffraction measurements following the evolution of phase segregation, presented in Papers III and IV of this thesis, were performed with a photon flux estimated to be roughly 10^3 photons·s^{-1}·μm^{-2}. Over the course of 30 minutes, the samples were exposed to a total photon dose of $1.8 \cdot 10^6$ photons·μm^{-2} at an energy of 9.28 keV. The dosage to which the samples are exposed in the course of the measurement thus corresponds to that just at the transition between the 'no-effect' region A and the onset of the degradation of

the optoelectronic properties, region B, as measured in the X-ray degradation experiments described here. It should be noted, however, that the lower energy of 9.28 keV used in the phase segregation experiments may result in a different energy dose compared to the degradation experiment. Further research is needed to accurately distinguish whether the X-ray degradation of metal halide perovskites depends predominantly on the total photon dose, the energy dose, or the photon or energy flux. Further, the X-ray degradation here is shown exemplary for a single sample. The exact numbers may be dependent on the processing condition and environmental factors. A more systematic study on a large number of samples spanning the entire compositional range is needed to accurately describe the sensitivity of mixed metal halide perovskites to hard X-ray in a more general manner. An accurate description of the x-ray degradation can then point the way to measurement schemes that minimize the effect of x-ray exposure without sacrificing data quality.

Conclusions

In this thesis, the light-induced phase segregation of mixed metal halide perovskites has been thoroughly investigated. The central experimental part of the work was the investigation of its mechanism. In addition, we analysed its effect on the efficiency of solar cell devices and also considered the challenges associated with the observation of such phenomena by X-ray based techniques.

While perovskite devices with varying bandgaps between 1.2 eV and 3 eV have been developed, material quality is not optimal across the entire bandgap range. $MAPbI_3$ solar cells with bandgaps between 1.55 eV and 1.6 eV are still yield the best efficiency. We have investigated the effect of bromide-iodide mixtures on device efficiency and found that suboptimal band alignment, higher defect density and light-induced phase segregation all contribute to the efficiency drop. In particular, the qualitative similarity of the dependence of photoluminescence quantum yield, stability and device efficiency on bromide content suggests a link between defect density and material stability.

The mechanism of light-induced phase segregation was investigated using multimodal *in-situ* Photoluminescence and X-ray Diffraction techniques and Photiluminescence microscopy. We revealed a multi-stage segregation process involving the initial formation of iodide-rich nanoscopic domains followed by extended phase segregation. Detailed analysis of the compositional phase distributions formed during segregation indicates that the first stage is photo-activated and can be explained by models based on energy gain of charge carriers due to differences in the bandgaps of phases with different halide composition. In contrast, in order to rationalise the second stage of phase segregation, we have developed a kinetic model which is based on light induced changes in the material properties during the segregation process. We propose that light induced vacancies locally change the diffusivity and thus effectively increase the mobility of the iodide. Our results highlight the importance of both intrinsic and light-induced defects in determining the photo-stability of mixed metal halide perovskites.

X-ray diffraction was one of the core techniques used throughout this work. We have therefore taken a step back to consider the effect of X-ray sensitivity on the phenomena

under investigation. We find that prior to any structural degradation, the optoelectronic properties decay, presumably through X-ray induced defect formation. Surprisingly, these x-ray induced defects strongly modify the phase segregation process and, at certain x-ray dose levels, almost eliminate the photoinduced phase segregation.

These results once again emphasise the mutual dependence of (photon induced) defects and the photo-stability of metal halide perovskites as a recurring theme throughout the thesis.

References

[1] M. A. Green, E. D. Dunlop, J. Hohl-Ebinger, M. Yoshita, N. Kopidakis, K. Bothe, D. Hinken, M. Rauer and X. Hao: "Solar cell efficiency tables (Version 60)". In: *Progress in Photovoltaics: Research and Applications* 30.7 (2022), pp. 687–701.

[2] H. Dierks, Z. Zhang, N. Lamers and J. Wallentin: "3D X-ray microscopy with a CsPbBr3 nanowire scintillator". In: *Nano Research* (2022).

[3] E. L. Unger, E. T. Hoke, C. D. Bailie, W. H. Nguyen, A. R. Bowring, T. Heumüller, M. G. Christoforo and M. D. McGehee: "Hysteresis and transient behavior in current–voltage measurements of hybrid-perovskite absorber solar cells". In: *Energy & Environmental Science* 7.11 (2014), pp. 3690–3698.

[4] J. M. Cave et al.: "Deducing transport properties of mobile vacancies from perovskite solar cell characteristics". In: *Journal of Applied Physics* 128.18 (2020), p. 184501.

[5] K. Domanski et al.: "Migration of cations induces reversible performance losses over day/night cycling in perovskite solar cells". In: *Energy & Environmental Science* 10.2 (2017), pp. 604–613.

[6] N. Wu, D. Walter, A. Fell, Y. Wu and K. Weber: "The Impact of Mobile Ions on the Steady-State Performance of Perovskite Solar Cells". In: *The Journal of Physical Chemistry C* 124.1 (2020), pp. 219–229.

[7] K. Suchan, A. Merdasa, C. Rehermann, E. L. Unger and I. G. Scheblykin: "Complex evolution of photoluminescence during phase segregation of MAPb(I1-xBrx)3 mixed halide perovskite". In: *Journal of Luminescence* 221 (2020), p. 117073.

[8] IEA: *Outlook for electricity – World Energy Outlook 2022 – Analysis.* IEA. 2022. URL: `https://www.iea.org/reports/world-energy-outlook-2022/outlook-for-electricity` (visited on 27/02/2023).

[9] IEA: *Net Zero by 2050 – Analysis.* IEA. 2021. URL: `https://www.iea.org/reports/net-zero-by-2050` (visited on 27/02/2023).

[10] D. Feldman, V. Ramasamy, R. Fu, A. Ramdas, J. Desai and R. Margolis: *U.S. Solar Photovoltaic System and Energy Storage Cost Benchmark (Q1 2020).* NREL/TP–6A20-77324, 1764908, MainId:26270. 2021.

[11] D. S. Philipps, F. Ise, W. Warmuth and P. P. GmbH: “Photovoltaics Report”. In: (2022).

[12] IRENA: “The True Cost of Fossil Fuels: Saving on the Externalities of Air Pollution and Climate Change (REmap brief) - IRENA_REmap_externality_brief_-2016.pdf”. In: (2016).

[13] E. T. Hoke, D. J. Slotcavage, E. R. Dohner, A. R. Bowring, H. I. Karunadasa and M. D. McGehee: “Reversible photo-induced trap formation in mixed-halide hybrid perovskites for photovoltaics”. In: *Chemical Science* 6.1 (2014), pp. 613–617.

[14] T. J. Jacobsson et al.: “An open-access database and analysis tool for perovskite solar cells based on the FAIR data principles”. In: *Nature Energy* 7.1 (2022), pp. 107–115.

[15] Z. Wang, Z. Song, Y. Yan, S. (Liu and D. Yang: “Perovskite—a Perfect Top Cell for Tandem Devices to Break the S–Q Limit”. In: *Advanced Science* 6.7 (2019), p. 1801704.

[16] T. Markvart: “Shockley: Queisser detailed balance limit after 60 years”. In: *WIREs Energy and Environment* 11.4 (2022), e430.

[17] NREL: *NREL Efficiency Chart.* Best Research-Cell Efficiencies. 2022. URL: `https://www.nrel.gov/pv/cell-efficiency.html` (visited on 26/09/2022).

[18] W. Shockley and H. J. Queisser: “Detailed Balance Limit of Efficiency of p□n Junction Solar Cells”. In: *Journal of Applied Physics* 32.3 (1961), pp. 510–519.

[19] A. Rajagopal, Z. Yang, S. B. Jo, I. L. Braly, P.-W. Liang, H. W. Hillhouse and A. K.-Y. Jen: “Highly Efficient Perovskite–Perovskite Tandem Solar Cells Reaching 80% of the Theoretical Limit in Photovoltage”. In: *Advanced Materials* 29.34 (2017), p. 1702140.

[20] G. E. Eperon, S. D. Stranks, C. Menelaou, M. B. Johnston, L. M. Herz and H. J. Snaith: “Formamidinium lead trihalide: a broadly tunable perovskite for efficient planar heterojunction solar cells”. In: *Energy & Environmental Science* 7.3 (2014), pp. 982–988.

[21] G. E. Eperon, M. T. Hörantner and H. J. Snaith: “Metal halide perovskite tandem and multiple-junction photovoltaics”. In: *Nature Reviews Chemistry* 1.12 (2017), pp. 1–18.

[22] S. Tao, I. Schmidt, G. Brocks, J. Jiang, I. Tranca, K. Meerholz and S. Olthof: “Absolute energy level positions in tin- and lead-based halide perovskites”. In: *Nature Communications* 10.1 (2019).

[23] J. H. Noh, S. H. Im, J. H. Heo, T. N. Mandal and S. I. Seok: “Chemical management for colorful, efficient, and stable inorganic-organic hybrid nanostructured solar cells”. In: *Nano Letters* 13.4 (2013), pp. 1764–1769.

[24] L. Vegard: “Die Konstitution der Mischkristalle und die Raumfüllung der Atome”. In: *Zeitschrift für Physik* 5.1 (1921), pp. 17–26.

[25] K. Miyata, T. L. Atallah and X.-Y. Zhu: “Lead halide perovskites: Crystal-liquid duality, phonon glass electron crystals, and large polaron formation”. In: *Science Advances* 3.10 (2017), e1701469.

[26] Y. Rakita, S. R. Cohen, N. K. Kedem, G. Hodes and D. Cahen: “Mechanical properties of APbX3 (A = Cs or CH_3NH_3; X = I or Br) perovskite single crystals”. In: *MRS Communications* 5.4 (2015), pp. 623–629.

[27] N. K. Tailor and S. Satapathi: “Crystalline-liquid duality of specific heat in halide perovskite semiconductor”. In: *Scripta Materialia* 223 (2023), p. 115061.

[28] C. Eames, J. M. Frost, P. R. F. Barnes, B. C. O’Regan, A. Walsh and M. S. Islam: “Ionic transport in hybrid lead iodide perovskite solar cells”. In: *Nature Communications* 6.1 (2015), p. 7497.

[29] K. Suchan, J. Just, P. Beblo, C. Rehermann, A. Merdasa, R. Mainz, I. G. Scheblykin and E. Unger: “Multi-Stage Phase-Segregation of Mixed Halide Perovskites under Illumination: A Quantitative Comparison of Experimental Observations and Thermodynamic Models”. In: *Advanced Functional Materials* 33.3 (2023), p. 2206047.

[30] Y. W. Woo, Y.-K. Jung, G. Y. Kim, S. Kim and A. Walsh: “Factors influencing halide vacancy transport in perovskite solar cells”. In: *Discover Materials* 2.1 (2022), p. 8.

[31] G. Y. Kim, A. Senocrate, T.-Y. Yang, G. Gregori, M. Grätzel and J. Maier: “Large tunable photoeffect on ion conduction in halide perovskites and implications for photodecomposition”. In: *Nature Materials* 17.5 (2018), pp. 445–449.

[32] N. Phung et al.: “Photoprotection in metal halide perovskites by ionic defect formation”. In: *Joule* 6.9 (2022), pp. 2152–2174.

[33] Y. Lin et al.: “Excess charge-carrier induced instability of hybrid perovskites”. In: *Nature Communications* 9.1 (2018), p. 4981.

[34] L. A. Frolova et al.: “Reversible Pb2+/Pb0 and I–/I3– Redox Chemistry Drives the Light-Induced Phase Segregation in All-Inorganic Mixed Halide Perovskites”. In: *Advanced Energy Materials* 11.12 (2021), p. 2002934.

[35] G. Y. Kim, A. Senocrate, Y.-R. Wang, D. Moia and J. Maier: “Photo-Effect on Ion Transport in Mixed Cation and Halide Perovskites and Implications for Photo-Demixing**”. In: *Angewandte Chemie International Edition* 60.2 (2021), pp. 820–826.

[36] T.-Y. Yang, G. Gregori, N. Pellet, M. Grätzel and J. Maier: “The Significance of Ion Conduction in a Hybrid Organic–Inorganic Lead-Iodide-Based Perovskite Photosensitizer”. In: *Angewandte Chemie International Edition* 54.27 (2015), pp. 7905–7910.

[37] M. Gerhard, B. Louis, R. Camacho, A. Merdasa, J. Li, A. Kiligaridis, A. Dobrovolsky, J. Hofkens and I. G. Scheblykin: "Microscopic insight into non-radiative decay in perovskite semiconductors from temperature-dependent luminescence blinking". In: *Nature Communications* 10.1 (2019), p. 1698.

[38] H. J. Snaith et al.: "Anomalous Hysteresis in Perovskite Solar Cells". In: *The Journal of Physical Chemistry Letters* 5.9 (2014), pp. 1511–1515.

[39] S. Mahesh, J. M. Ball, R. D. J. Oliver, D. P. McMeekin, P. K. Nayak, M. B. Johnston and H. J. Snaith: "Revealing the origin of voltage loss in mixed-halide perovskite solar cells". In: *Energy & Environmental Science* 13.1 (2020), pp. 258–267.

[40] K. Datta et al.: "Effect of Light-Induced Halide Segregation on the Performance of Mixed-Halide Perovskite Solar Cells". In: *ACS Applied Energy Materials* 4.7 (2021), pp. 6650–6658.

[41] A. Singareddy, U. K. R. Sadula and P. R. Nair: "Phase segregation induced efficiency degradation and variability in mixed halide perovskite solar cells". In: *Journal of Applied Physics* 130.22 (2021), p. 225501.

[42] G. F. Samu, C. Janáky and P. V. Kamat: "A Victim of Halide Ion Segregation. How Light Soaking Affects Solar Cell Performance of Mixed Halide Lead Perovskites". In: *ACS Energy Letters* 2.8 (2017), pp. 1860–1861.

[43] B. Das, I. Aguilera, U. Rau and T. Kirchartz: "Effect of doping, photodoping and bandgap variation on the performance of perovskite solar cells". In: (), p. 37.

[44] W. Rehman, D. P. McMeekin, J. B. Patel, R. L. Milot, M. B. Johnston, H. J. Snaith and L. M. Herz: "Photovoltaic mixed-cation lead mixed-halide perovskites: links between crystallinity, photo-stability and electronic properties". In: *Energy & Environmental Science* 10.1 (2017), pp. 361–369.

[45] D. J. Slotcavage, H. I. Karunadasa and M. D. McGehee: "Light-Induced Phase Segregation in Halide-Perovskite Absorbers". In: *ACS Energy Letters* 1.6 (2016), pp. 1199–1205.

[46] S. J. Yoon, S. Draguta, J. S. Manser, O. Sharia, W. F. Schneider, M. Kuno and P. V. Kamat: "Tracking Iodide and Bromide Ion Segregation in Mixed Halide Lead Perovskites during Photoirradiation". In: *ACS Energy Letters* 1.1 (2016), pp. 290–296.

[47] A. J. Barker et al.: "Defect-Assisted Photoinduced Halide Segregation in Mixed-Halide Perovskite Thin Films". In: *ACS Energy Letters* 2.6 (2017), pp. 1416–1424.

[48] M. C. Brennan, S. Draguta, P. V. Kamat and M. Kuno: "Light-Induced Anion Phase Segregation in Mixed Halide Perovskites". In: *ACS Energy Letters* 3.1 (2018), pp. 204–213.

[49] A. Ruth, M. C. Brennan, S. Draguta, Y. V. Morozov, M. Zhukovskyi, B. Janko, P. Zapol and M. Kuno: "Vacancy-Mediated Anion Photosegregation Kinetics in Mixed Halide Hybrid Perovskites: Coupled Kinetic Monte Carlo and Optical Measurements". In: *ACS Energy Letters* (2018), p. 8.

[50] S. Draguta, J. A. Christians, Y. V. Morozov, A. Mucunzi, J. S. Manser, P. V. Kamat, J. M. Luther and M. Kuno: "A quantitative and spatially resolved analysis of the performance-bottleneck in high efficiency, planar hybrid perovskite solar cells". In: *Energy & Environmental Science* 11.4 (2018), pp. 960–969.

[51] C. M. Sutter-Fella et al.: "Cation-Dependent Light-Induced Halide Demixing in Hybrid Organic–Inorganic Perovskites". In: *Nano Letters* 18.6 (2018), pp. 3473–3480.

[52] A. J. Knight, A. D. Wright, J. B. Patel, D. P. McMeekin, H. J. Snaith, M. B. Johnston and L. M. Herz: "Electronic Traps and Phase Segregation in Lead Mixed-Halide Perovskite". In: *ACS Energy Letters* (2018), pp. 75–84.

[53] A. J. Knight, J. Borchert, R. D. J. Oliver, J. B. Patel, P. G. Radaelli, H. J. Snaith, M. B. Johnston and L. M. Herz: "Halide Segregation in Mixed-Halide Perovskites: Influence of A-Site Cations". In: *ACS Energy Letters* 6.2 (2021), pp. 799–808.

[54] W. Rehman, R. L. Milot, G. E. Eperon, C. Wehrenfennig, J. L. Boland, H. J. Snaith, M. B. Johnston and L. M. Herz: "Charge-Carrier Dynamics and Mobilities in Formamidinium Lead Mixed-Halide Perovskites". In: *Advanced Materials* 27.48 (2015), pp. 7938–7944.

[55] D. Guo, Z. Andaji Garmaroudi, M. Abdi-Jalebi, S. D. Stranks and T. J. Savenije: "Reversible Removal of Intermixed Shallow States by Light Soaking in Multication Mixed Halide Perovskite Films". In: *ACS Energy Letters* 4.10 (2019), pp. 2360–2367.

[56] M. C. Brennan, A. Ruth, P. V. Kamat and M. Kuno: "Photoinduced Anion Segregation in Mixed Halide Perovskites". In: *Trends in Chemistry.* Special Issue - Laying Groundwork for the Future 2.4 (2020), pp. 282–301.

[57] C. G. Bischak, A. B. Wong, E. Lin, D. T. Limmer, P. Yang and N. S. Ginsberg: "Tunable Polaron Distortions Control the Extent of Halide Demixing in Lead Halide Perovskites". In: *The Journal of Physical Chemistry Letters* (2018).

[58] F. Brivio, C. Caetano and A. Walsh: "Thermodynamic Origin of Photoinstability in the $CH_3NH_3Pb(I_{1-x}Br_x)_3$ Hybrid Halide Perovskite Alloy". In: *The Journal of Physical Chemistry Letters* 7.6 (2016), p. 1083.

[59] X. Wang et al.: "Suppressed phase separation of mixed-halide perovskites confined in endotaxial matrices". In: *Nature Communications* 10.1 (2019), p. 695.

[60] I. M. Pavlovetc, A. Ruth, I. Gushchina, L. Ngo, S. Zhang, Z. Zhang and M. Kuno: "Distinguishing Models for Mixed Halide Lead Perovskite Photosegregation via Terminal Halide Stoichiometry". In: *ACS Energy Letters* (2021), pp. 2064–2071.

[61] C. G. Bischak, C. L. Hetherington, H. Wu, S. Aloni, D. F. Ogletree, D. T. Limmer and N. S. Ginsberg: "Origin of Reversible Photoinduced Phase Separation in Hybrid Perovskites". In: *Nano Letters* 17.2 (2017), pp. 1028–1033.

[62] R. E. Beal et al.: "Structural Origins of Light-Induced Phase Segregation in Organic-Inorganic Halide Perovskite Photovoltaic Materials". In: *Matter* 2.1 (2020), pp. 207–219.

[63] G. C. Halford, Q. Deng, A. Gomez, T. Green, J. M. Mankoff and R. A. Belisle: "Structural Dynamics of Metal Halide Perovskites during Photoinduced Halide Segregation". In: *ACS Applied Materials & Interfaces* 14.3 (2022), pp. 4335–4343.

[64] M. Hu, C. Bi, Y. Yuan, Y. Bai and J. Huang: "Stabilized Wide Bandgap MAPbBrxI3–x Perovskite by Enhanced Grain Size and Improved Crystallinity". In: *Advanced Science* 3.6 (2016), n/a–n/a.

[65] X. Yang, X. Yan, W. Wang, X. Zhu, H. Li, W. Ma and C. Sheng: "Light induced metastable modification of optical properties in $CH_3NH_3PbI_{3-x}Br_x$ perovskite films: Two-step mechanism". In: *Organic Electronics* 34 (2016), pp. 79–83.

[66] T. Duong et al.: "Light and Electrically Induced Phase Segregation and Its Impact on the Stability of Quadruple Cation High Bandgap Perovskite Solar Cells". In: *ACS Applied Materials & Interfaces* 9.32 (2017), pp. 26859–26866.

[67] T. C.-J. Yang, P. Fiala, Q. Jeangros and C. Ballif: "High-Bandgap Perovskite Materials for Multijunction Solar Cells". In: *Joule* 2.8 (2018), pp. 1421–1436.

[68] S. Draguta, O. Sharia, S. J. Yoon, M. C. Brennan, Y. V. Morozov, J. S. Manser, P. V. Kamat, W. F. Schneider and M. Kuno: "Rationalizing the light-induced phase separation of mixed halide organic–inorganic perovskites". In: *Nature Communications* 8.1 (2017), p. 200.

[69] H. Funk, O. Shargaieva, A. Eljarrat, E. L. Unger, C. T. Koch and D. Abou-Ras: "In Situ TEM Monitoring of Phase-Segregation in Inorganic Mixed Halide Perovskite". In: *The Journal of Physical Chemistry Letters* 11.13 (2020), pp. 4945–4950.

[70] J.-W. Lee, S.-H. Bae, N. De Marco, Y.-T. Hsieh, Z. Dai and Y. Yang: "The role of grain boundaries in perovskite solar cells". In: *Materials Today Energy* 7 (2018), pp. 149–160.

[71] W. Mao, C. R. Hall, S. Bernardi, Y.-B. Cheng, A. Widmer-Cooper, T. A. Smith and U. Bach: "Light-induced reversal of ion segregation in mixed-halide perovskites". In: *Nature Materials* 20.1 (2021), pp. 55–61.

[72] W. Mao, C. R. Hall, A. S. R. Chesman, C. Forsyth, Y.-B. Cheng, N. W. Duffy, T. A. Smith and U. Bach: "Visualizing Phase Segregation in Mixed-Halide Perovskite Single Crystals". In: *Angewandte Chemie International Edition* 58.9 (2019), pp. 2893–2898.

[73] T. Elmelund, B. Seger, M. Kuno and P. V. Kamat: "How Interplay between Photo and Thermal Activation Dictates Halide Ion Segregation in Mixed Halide Perovskites". In: *ACS Energy Letters* 5.1 (2020), pp. 56–63.

[74] Z. Chen, G. Brocks, S. Tao and P. A. Bobbert: "Unified theory for light-induced halide segregation in mixed halide perovskites". In: *Nature Communications* 12.1 (2021), p. 2687.

[75] R. A. Kerner, Z. Xu, B. W. Larson and B. P. Rand: "The role of halide oxidation in perovskite halide phase separation". In: *Joule* 5.9 (2021), pp. 2273–2295.

[76] D. O. Tiede, M. E. Calvo, J. F. Galisteo-López and H. Míguez: "Local Rearrangement of the Iodide Defect Structure Determines the Phase Segregation Effect in Mixed-Halide Perovskites". In: *The Journal of Physical Chemistry Letters* 11.12 (2020), pp. 4911–4916.

[77] A. Merdasa et al.: "Impact of Excess Lead Iodide on the Recombination Kinetics in Metal Halide Perovskites". In: *ACS Energy Letters* 4.6 (2019), pp. 1370–1378.

[78] A. Merdasa: "Super-resolution Luminescence Micro-Spectroscopy: A nano-scale view of solar cell material photophysics". Doctoral Thesis (compilation). Lund: Lund University, Faculty of Science, Department of Chemistry, Division of Chemical Physics, 2017.

[79] M. Wansleben, C. Zech, C. Streeck, J. Weser, C. Genzel, B. Beckhoff and R. Mainz: "Photon flux determination of a liquid-metal jet X-ray source by means of photon scattering". In: *Journal of Analytical Atomic Spectrometry* 34.7 (2019), pp. 1497–1502.

[80] H. Näsström, P. Becker, J. A. Márquez, O. Shargaieva, R. Mainz, E. Unger and T. Unold: "Dependence of phase transitions on halide ratio in inorganic CsPb(BrxI1–x)3 perovskite thin films obtained from high-throughput experimentation". In: *Journal of Materials Chemistry A* 8.43 (2020), pp. 22626–22631.

[81] A. Bianconi, D. Jackson and K. Monahan: "Intrinsic luminescence excitation spectrum and extended x-ray absorption fine structure above the K edge in CaF2". In: *Physical Review B* 17.4 (1978), pp. 2021–2024.

[82] T. Unold and L. Gütay: "Photoluminescence Analysis of Thin-Film Solar Cells". In: *Advanced Characterization Techniques for Thin Film Solar Cells.* Ed. by D. Abou-Ras, T. Kirchartz and U. Rau. Weinheim, Germany: Wiley-VCH Verlag GmbH & Co. KGaA, 2011, pp. 151–175.

[83] J. Even, L. Pedesseau and C. Katan: "Analysis of Multivalley and Multibandgap Absorption and Enhancement of Free Carriers Related to Exciton Screening in Hybrid Perovskites". In: *The Journal of Physical Chemistry C* 118.22 (2014), pp. 11566–11572.

[84] M. Saba et al.: "Correlated electron–hole plasma in organometal perovskites". In: *Nature Communications* 5 (2014), p. 5049.

[85] P. Fedeli et al.: "Influence of the Synthetic Procedures on the Structural and Optical Properties of Mixed-Halide (Br, I) Perovskite Films". In: *The Journal of Physical Chemistry C* 119.37 (2015), pp. 21304–21313.

[86] C. M. Sutter-Fella, Y. Li, M. Amani, J. W. Ager, F. M. Toma, E. Yablonovitch, I. D. Sharp and A. Javey: "High Photoluminescence Quantum Yield in Band Gap Tunable Bromide Containing Mixed Halide Perovskites". In: *Nano Letters* 16.1 (2016), pp. 800–806.

[87] W. H. Miller: *A Treatise on Crystallography.* For J. & J. J. Deighton, 1839. 190 pp.

[88] C. S. Weiss: *Ueber eine verbesserte Methode fuer die Bezeichnung der verschiedenen Flächen eines Kristallisationssystemes.* In collab. with L. Natural History Museum Library. Königlich Preussische Akademie der Wissenschaften zu Berlin, 1816. 584 pp.

[89] P.Scherer: "Bestimmung der Größe und der inneren Struktur von Kolloidteilchen". In: *Nachrichten von der Gesellschaft der Wissenschaften zu Göttingen, Mathematisch-Physikalische Klasse* 1918 (Mathematica 1918).

[90] G. K. Williamson and W. H. Hall: "X-ray line broadening from filed aluminium and wolfram". In: *Acta Metallurgica* 1.1 (1953), pp. 22–31.

[91] M. E. Stuckelberger et al.: "Effects of X-rays on Perovskite Solar Cells". In: *The Journal of Physical Chemistry C* 124.33 (2020), pp. 17949–17956.

[92] F. Peña-Camargo et al.: "Halide Segregation versus Interfacial Recombination in Bromide-Rich Wide-Gap Perovskite Solar Cells". In: *ACS Energy Letters* 5.8 (2020), pp. 2728–2736.

[93] K. Suchan, J. Just, P. Becker, C. Rehermann, A. Merdasa, R. Mainz, I. G. Scheblykin and E. L. Unger: "Broad Distribution of Local I/Br Ratio in Illuminated Mixed Halide Perovskite Films Revealed by Correlative X-ray Diffraction and Photoluminescence". In: *arXiv:2101.00645 [cond-mat, physics:physics]* (2021). arXiv: 2101.00645.

[94] G. Xing, N. Mathews, S. S. Lim, N. Yantara, X. Liu, D. Sabba, M. Grätzel, S. Mhaisalkar and T. C. Sum: "Low-temperature solution-processed wavelength-tunable perovskites for lasing". In: *Nature Materials* 13.5 (2014), pp. 476–480.

[95] A. Sadhanala et al.: "Blue-Green Color Tunable Solution Processable Organolead Chloride–Bromide Mixed Halide Perovskites for Optoelectronic Applications". In: *Nano Letters* 15.9 (2015), pp. 6095–6101.

[96] F. Babbe, E. Masquelier, Z. Zheng and C. M. Sutter-Fella: "Flash Formation of I-Rich Clusters during Multistage Halide Segregation Studied in MAPbI1.5Br1.5". In: *The Journal of Physical Chemistry C* 124.45 (2020), pp. 24608–24615.

[97] L. Tian, J. Xue and R. Wang: "Halide Segregation in Mixed Halide Perovskites: Visualization and Mechanisms". In: *Electronics* 11.5 (2022), p. 700.

[98] A. Senocrate, I. Moudrakovski, G. Y. Kim, T.-Y. Yang, G. Gregori, M. Grätzel and J. Maier: "The Nature of Ion Conduction in Methylammonium Lead Iodide: A Multimethod Approach". In: *Angewandte Chemie (International Ed. in English)* 56.27 (2017), pp. 7755–7759.

[99] Y.-C. Zhao, W.-K. Zhou, X. Zhou, K.-H. Liu, D.-P. Yu and Q. Zhao: "Quantification of light-enhanced ionic transport in lead iodide perovskite thin films and its solar cell applications". In: *Light: Science & Applications* 6.5 (2017), e16243–e16243.

[100] Y.-T. Li et al.: "Light-Enhanced Ion Migration in Two-Dimensional Perovskite Single Crystals Revealed in Carbon Nanotubes/Two-Dimensional Perovskite Heterostructure and Its Photomemory Application". In: *ACS Central Science* 5.11 (2019), pp. 1857–1865.

[101] Y. Yuan, J. Chae, Y. Shao, Q. Wang, Z. Xiao, A. Centrone and J. Huang: "Photovoltaic Switching Mechanism in Lateral Structure Hybrid Perovskite Solar Cells". In: *Advanced Energy Materials* 5.15 (2015), p. 1500615.

[102] A. Walsh and S. D. Stranks: "Taking Control of Ion Transport in Halide Perovskite Solar Cells". In: *ACS Energy Letters* 3.8 (2018), pp. 1983–1990.

[103] F. Lang et al.: "Radiation Hardness and Self-Healing of Perovskite Solar Cells". In: *Advanced Materials (Deerfield Beach, Fla.)* 28.39 (2016), pp. 8726–8731.

[104] S. Chen and P. Gao: "Challenges, myths, and opportunities of electron microscopy on halide perovskites". In: *Journal of Applied Physics* 128.1 (2020), p. 010901.

[105] S. Chen et al.: "Atomic-scale imaging of $CH_3NH_3PbI_3$ structure and its decomposition pathway". In: *Nature Communications* 12.1 (2021), p. 5516.

[106] N. Klein-Kedem, D. Cahen and G. Hodes: "Effects of Light and Electron Beam Irradiation on Halide Perovskites and Their Solar Cells". In: *Accounts of Chemical Research* 49.2 (2016), pp. 347–354.

[107] Z. Dang et al.: "In Situ Transmission Electron Microscopy Study of Electron Beam-Induced Transformations in Colloidal Cesium Lead Halide Perovskite Nanocrystals". In: *ACS Nano* 11.2 (2017), pp. 2124–2132.

[108] X.-G. Zhou et al.: "Probing the Electron Beam-Induced Structural Evolution of Halide Perovskite Thin Films by Scanning Transmission Electron Microscopy". In: *The Journal of Physical Chemistry C* 125.19 (2021), pp. 10786–10794.

[109] S. Meloni, G. Palermo, N. Ashari-Astani, M. Grätzel and U. Rothlisberger: "Valence and conduction band tuning in halide perovskites for solar cell applications". In: *Journal of Materials Chemistry A* 4.41 (2016), pp. 15997–16002.

[110] S. Svanström, A. G. Fernández, T. Sloboda, T. J. Jacobsson, H. Rensmo and U. B. Cappel: "X-ray stability and degradation mechanism of lead halide perovskites and lead halides". In: *Physical Chemistry Chemical Physics* 23.21 (2021), pp. 12479–12489.

[111] J. Ferrer Orri, T. A. Doherty, D. Johnstone, S. M. Collins, H. Simons, P. A. Midgley, C. Ducati and S. D. Stranks: "Unveiling the Interaction Mechanisms of Electron and X-ray Radiation with Halide Perovskite Semiconductors using Scanning Nanoprobe Diffraction". In: *Advanced Materials* 34.18 (2022), p. 2200383.

[112] R. L. Z. Hoye et al.: "Perovskite-Inspired Photovoltaic Materials: Toward Best Practices in Materials Characterization and Calculations". In: *Chemistry of Materials* 29.5 (2017), pp. 1964–1988.

[113] R. T. Ross: "Some Thermodynamics of Photochemical Systems". In: *The Journal of Chemical Physics* 46.12 (1967), pp. 4590–4593.

[114] A. Dobrovolsky, A. Merdasa, E. L. Unger, A. Yartsev and I. G. Scheblykin: "Defect-induced local variation of crystal phase transition temperature in metal-halide perovskites". In: *Nature Communications* 8.1 (2017), p. 34.

[115] X. Zou: "Dynamics of Photogenerated Charge Carriers in III-V Bulk and Nanowire Semiconductors". PhD thesis. Lund University, 2020.

Scientific publications

Author contributions

Paper I : Rationalizing Performance Losses of Wide-Bandgap Perovskite Solar Cells Evident in Data from the Perovskite Database

I did the majority of the data analysis and wrote the manuscript for the majority of the content.

Paper II: Complex evolution of photoluminescence during phase segregation of $MAPb(I_{1-x}Br_x)_3$ mixed halide perovskites

I designed and performed the experiments together with Aboma Merdasa. I analyzed the data and wrote the manuscript with support of the co-authors.

Paper III: Multi-Stage Phase-Segregation of Mixed Halide Perovskites under Illumination: A Quantitative Comparison of Experimental Observations and Thermodynamic Models

I constructed the experimental setup together with Justus Just. I planned and carried out the experiments. I analyzed the data and wrote the manuscript with support of the co-authors.

Paper IV: Light-Induced Halide Vacancies as Key Players in the Temperature-Dependent Phase Segregation of Mixed Metal Halide Perovskites

I planned and carried out the experiments. I analyzed the data, performed the numerical simulations and wrote the manuscript with support of the co-authors.